



저작자표시-비영리-변경금지 2.0 대한민국

이용자는 아래의 조건을 따르는 경우에 한하여 자유롭게

- 이 저작물을 복제, 배포, 전송, 전시, 공연 및 방송할 수 있습니다.

다음과 같은 조건을 따라야 합니다:



저작자표시. 귀하는 원저작자를 표시하여야 합니다.



비영리. 귀하는 이 저작물을 영리 목적으로 이용할 수 없습니다.



변경금지. 귀하는 이 저작물을 개작, 변형 또는 가공할 수 없습니다.

- 귀하는, 이 저작물의 재이용이나 배포의 경우, 이 저작물에 적용된 이용허락조건을 명확하게 나타내어야 합니다.
- 저작권자로부터 별도의 허가를 받으면 이러한 조건들은 적용되지 않습니다.

저작권법에 따른 이용자의 권리는 위의 내용에 의하여 영향을 받지 않습니다.

이것은 [이용허락규약\(Legal Code\)](#)을 이해하기 쉽게 요약한 것입니다.

[Disclaimer](#)

공학박사 학위논문

**Characteristic pinning properties of  
REBa<sub>2</sub>Cu<sub>3</sub>O<sub>7-δ</sub> (RE= Eu and Gd) films  
by the PLD and RCE-DR process**

PLD 및 RCE-DR 공정으로 제조된  
REBa<sub>2</sub>Cu<sub>3</sub>O<sub>7-δ</sub> (RE= Eu and Gd) film의  
피닝 특성 분석

2020년 2월

서울대학교 대학원

재료공학부

오 원 재

# Characteristic pinning properties of $\text{REBa}_2\text{Cu}_3\text{O}_{7-\delta}$ (RE = Eu and Gd) films by the PLD and RCE-DR process

PLD 및 RCE-DR 공정으로 제조된  
 $\text{REBa}_2\text{Cu}_3\text{O}_{7-\delta}$  (RE = Eu and Gd) film 의 피닝 특성 분석

지도교수 유 상 임

이 논문을 공학박사학위논문으로 제출함  
2020년 2월

서울대학교 대학원  
재료공학부  
오 원 재

오원재의 박사학위논문을 인준함  
2020년 02월

위 원 장 \_\_\_\_\_ 박 찬

(인) 

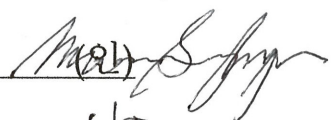
부 위 원 장 \_\_\_\_\_ 유 상 임

(인) 

위 원 \_\_\_\_\_ 김 미 영

(인) 

위 원 \_\_\_\_\_ 문 승 현

(인) 

위 원 \_\_\_\_\_ 정 국 채

(인) 

## **Abstract**

# **Characteristic pinning properties of REBa<sub>2</sub>Cu<sub>3</sub>O<sub>7- $\delta$</sub> (RE= Eu and Gd) films by the PLD and RCE-DR process**

Won-Jae Oh

Department of Materials Science and Engineering

The Graduate School

Seoul National University

The reactive co-evaporation deposition and reaction (RCE-DR) process has the advantages of a high throughput and high critical current density ( $J_c$ ) values at 77 K in self-field. However, the pinning properties of GdBa<sub>2</sub>Cu<sub>3</sub>O<sub>7- $\delta$</sub>  (GdBCO) coated conductors (CCs) by RCE-DR are inferior to that of REBa<sub>2</sub>Cu<sub>3</sub>O<sub>7- $\delta$</sub>  (REBCO, RE = rare earth elements) CCs by other processes such as pulsed laser deposition (PLD), metal-organic deposition (MOD), and metal-organic chemical vapor deposition (MOCVD). To improve the pinning properties of

REBCO films by RCE-DR, two different approaches have been tried in this study. One is to refine the  $\text{RE}_2\text{O}_3$  particles trapped in the REBCO films to the level of the artificial pinning centers (APCs) by other processes such as PLD and MOD, and the other is to control the defects like stacking fault (SF) in the GdBCO matrix via the post-annealing process in a reduced atmosphere for GdBCO CCs by RCE-DR.

Since the average size of the  $\text{Gd}_2\text{O}_3$  particles trapped in the GdBCO films by RCE-DR is too large to effectively pin the flux lines,  $\text{Gd}_2\text{O}_3$  particles should be refined to improve in-field  $J_c$  values. As such an effort, in this study, the REBCO (RE = Eu and Gd) films with  $\text{RE}_2\text{O}_3$  nanoparticles (RE= Eu and Gd) were fabricated on  $\text{CeO}_2$ -buffered MgO (100) single crystal substrate by the PLD process, and their characteristic pinning properties were analyzed in order to investigate how much the pinning properties can be improved by the refinement of  $\text{RE}_2\text{O}_3$  particles in the REBCO matrix. Also, we investigated the origin of  $J_c$  peak along the  $c$ -axis direction for the GdBCO films fabricated by the PLD process. On the other hand, the GdBCO CCs by RCE-DR were post-annealed at various high temperatures in low  $P_{\text{O}_2}$  region in order to improve the pinning properties of GdBCO CCs fabricated by RCE-DR in SuNAM Co. in Korea. We carefully selected the post-annealing conditions on the basis of the stability diagram of GdBCO. The major results are as the following.

First, we tried to optimize the pinning properties of REBCO (RE= Eu and Gd) films with the  $\text{RE}_2\text{O}_3$  nanoparticles. The GdBCO films with the  $\text{Gd}_2\text{O}_3$  contents of 0, 2, 5, 7 and 10 mol% and EuBCO films with the  $\text{Eu}_2\text{O}_3$  contents of 0, 2, 4, 5, 6 and 8 mol% were fabricated on  $\text{CeO}_2$ -buffered MgO (100) substrate by the PLD process using the surface modified target. Among these

samples, the 5 mol % Gd<sub>2</sub>O<sub>3</sub>-doped GdBCO film and 4 mol% Eu<sub>2</sub>O<sub>3</sub>-doped EuBCO film exhibited the highest in-field  $J_c$  values compared with other samples at temperatures of 20 and 40 K for  $B//c$ , and they also showed the maximum pinning force density ( $F_{p,max}$ ) value at 20 and 40 K, indicating that 5 mol% Gd<sub>2</sub>O<sub>3</sub> and 4 mol% Eu<sub>2</sub>O<sub>3</sub> were the optimum doping contents below 40 K, respectively. However, the RE<sub>2</sub>O<sub>3</sub> nanoparticles were ineffective for improving the pinning properties at higher temperatures (> 65 K). Analysis by transmission electron microscopy (TEM) for these samples revealed that the RE<sub>2</sub>O<sub>3</sub> nanoparticles with an average diameter of ~18 nm were randomly dispersed in the REBCO matrix. Unlike GdBCO CCs by RCE-DR, these peculiar pinning characteristics are attributable to more severe degradation in the superconducting transition temperature ( $T_{c,zero}$ ) due to the formation of solid solution in addition to a residual strain effect around RE<sub>2</sub>O<sub>3</sub> nanoparticles. The average sizes of RE<sub>2</sub>O<sub>3</sub> were ~18 nm, which is much smaller than that of Y<sub>2</sub>O<sub>3</sub> nanoparticles (~ 8 nm).

Second, we investigated the origin of  $J_c$  peak along the  $c$ -axis direction for the GdBCO films fabricated by the PLD process. By modifying the position of a laser focal point on the PLD target, we could fabricate the GdBCO films with (sample A) or without (sample B) the  $J_c$  peak along the  $c$ -axis direction at 77 K in 1 T. The outgrowths on the film surface were observable in sample A while the sample B exhibited smooth film surface. From the angular dependence of  $J_c$ , the sample A showed the  $J_c$  peak for  $B//c$  while the degradation of  $J_c$  peak for  $B//ab$  was observable at 77 K in 1 T. However, the  $J_c$  peak for  $B//c$  of sample A disappeared with increasing magnetic fields at 77 K. In contrast, the  $J_c$  peak for  $B//c$  was unobservable in the sample B at 77 K in 1 T. Analyses by scanning

transmission electron microscopy (STEM) revealed that the threading dislocations and twin boundaries existed for both sample A and B. A significant difference in microstructures between sample A and B was the density and length of SF. The SF density of sample A was much higher than that of sample B. Also, the SF length of sample A was much smaller than that of sample B. Consequently, the edge dislocation at the boundaries of SFs is believed to act as the pinning centers, leading to the  $J_c$  peak for  $B//c$  in sample A.

Third, we identified the post-annealing effect on the pinning properties of GdBCO CCs fabricated by the RCE-DR process. The GdBCO CCs annealed at 750°C in the  $PO_2$  of 300 mTorr for 15 min show the most enhanced  $J_c$  for  $B//c$  due to the SFs piled up along the  $c$ -axis. The minimum critical current density ( $J_{c,min}$ ) values of post-annealed samples in relatively higher fields like 5 T at 77 K and 7 T at 65 K were larger than those of pristine sample although their  $J_{c,min}$  values were lower in relatively lower fields like 1 T at 77 K and 3 T at 65 K. In-field  $J_c$  values for  $B//ab$  were closely related to the density of SFs within samples. Analysis results by TEM revealed that the SF density was remarkably reduced after the post-annealing process, which is responsible for enhanced  $J_{c,min}$  values and significantly degraded  $J_c$  values for  $B//ab$  in relatively higher fields. Also, we extended the post-annealing temperatures to relatively lower temperatures. Unlike as-grown GdBCO CCs, samples post-annealed at the temperature region of 450-600°C for 1 h included the higher SF density and GdBa<sub>2</sub>Cu<sub>4</sub>O<sub>8</sub> (Gd124) phase while samples annealed at 650 and 750°C showed relatively lower SF density. The HAADF-STEM analyses on the GdBCO CCs annealed at 500°C revealed that the Gd124 phase was mainly observed at the region near the CuO phase. At the temperature of 50-77 K, while the  $J_{c,min}$

values of as-grown GdBCO CC were enhanced in relatively higher fields after post-annealing at 750°C due to reduced SF density, both  $J_c^{ab}$  and  $J_{c,min}$  values were increased after post-annealing at 500°C in relatively lower fields due to both increased SF density and the formation of Gd124.

**Keywords:** REBa<sub>2</sub>Cu<sub>3</sub>O<sub>7-δ</sub> (REBCO, RE= Eu and Gd) films, Eu<sub>2</sub>O<sub>3</sub>-doped EuBCO films, Gd<sub>2</sub>O<sub>3</sub>-doped GdBCO films, pulsed laser deposition (PLD), reactive co-evaporation deposition and reaction (RCE-DR), post-annealing process, Flux pinning, critical current density ( $J_c$ ), pinning force density ( $F_p$ )

***Student Number: 2014-21430***

# Contents

List of Tables .....	viii
List of Figures .....	ix

## **Chapter 1 General introduction..... 1**

1.1 High temperature superconductor (HTS) .....	1
1.2 Flux pinning of REBCO superconductor .....	3
1.2.1 Flux pinning mechanism .....	3
1.2.2 Artificial pinning centers (APCs) in HTS .....	5
1.3 REBCO films by various abrication technologies.....	6
1.3.1 Pulsed laser deposition (PLD).....	7
1.3.2 Metal-organic chemical vapor deposition (MOCVD) .....	8
1.3.3 Metal-organic deposition (MOD) .....	9
1.3.4 Reactive co-evaporation deposition & reaction (RCE-DR)..	9

## **Chapter 2 Improvement of pinning properties for RE<sub>2</sub>O<sub>3</sub>-doped REBCO (RE = Eu, Gd) films by the PLD process ..... 35**

2.1 Introduction .....	35
2.2 Experimental.....	36
2.3 Results and discussion.....	38
2.3.1 GdBCO films with Gd <sub>2</sub> O <sub>3</sub> nanoparticles.....	38
2.3.2 EuBCO films with Eu <sub>2</sub> O <sub>3</sub> nanoparticles .....	42
2.4 Summary.....	47

<b>Chapter 3 Origin of <math>J_c</math> peak along the <math>c</math>-axis direction for the GdBCO films by the PLD process.....</b>	<b>75</b>
3.1 Introduction .....	75
3.2 Experimental .....	76
3.3 Results and discussion.....	77
3.4 Summary.....	80
<b>Chapter 4 Effect of post-annealing on the pinning properties of GdBCO CCs by the RCE-DR process .....</b>	<b>94</b>
4.1 Introduction .....	94
4.2 Experimental .....	95
4.3 Results and discussion.....	97
4.3.1 High temperature annealing in low $PO_2$ region .....	97
4.3.2 Low temperature annealing in low $PO_2$ region.....	101
4.4 Summary.....	110
<b>Chapter 5 Conclusion.....</b>	<b>133</b>
Publications.....	136
Abstract in Korean.....	139
Acknowledgement.....	143

## List of Tables

Table 3.1. The $T_{c,zero}$ , $\phi$ scan of (103) reflection, and $\omega$ scan of (005) reflection.. .....	86
Table 4.1. $T_{c,zero}$ , $\Delta T_c$ , Average linear SF density, FWHM values of (003) reflections, and magnetic $J_c$ values for samples.....	118
Table 4.2. $T_{c,zero}$ , $\Delta T_c$ , Average linear SF density, and the FWHM values of (003) reflections for samples .....	119

## List of Figures

Fig. 1.1. Electric applications of LTS, 1G HTS, and 2G HTS as a function of magnetic field [4]. .....	22
Fig. 1.2. Crystallographic structure of YBCO and REBCO.....	23
Fig. 1.3. $T_c$ values of YBCO compound versus the oxygen content $x$ ( $\text{YBa}_2\text{Cu}_3\text{O}_{7-x}$ ) [5].....	24
Fig. 1.4. (a) Orthorhombic and (b) tetragonal structures of YBCO compound [7] .....	25
Fig. 1.5. A schematic of the architecture for REBCO CCs [10].....	26
Fig. 1.6. Field dependence of magnetization for (a) type-I superconductor and (b) type-II superconductor.....	27
Fig. 1.7. Schematics of quantized flux lines and flux pinning [12].....	28
Fig. 1.8. Naturally generated defects in the REBCO films [29].....	29
Fig. 1.9. Schematic of the dimensionality of artificial pinning centers (APCs): (a) 0D-APC, (b) 1D-APC, (c) 2D-APC, and (d) 3D-APC [30] .....	30
Fig. 1.10. Comparison of the configuration of a pinned vortex by 1D-APCs or 3D-APCs: (a) the zigzag state of the vortex line when the magnetic field is applied tilted from the direction of 1D-APCs, (b) the vortex line which is pinned	

by the randomly distributed 3D-APCs in the tilted magnetic field [41] .....	31
Fig. 1.11. Summarization of the $J_{c,min}$ and $J_c$ for $B//c$ values as function of fabrication technologies .....	32
Fig. 1.12. A schematic of PLD system .....	33
Fig. 1.13. A schematic of the RCE-DR process and the program of the automated deposition control [79].....	34
Fig. 2.1. XRD patterns of all GdBCO films deposited on CeO <sub>2</sub> -buffered MgO (100) substrates .....	57
Fig. 2.2. The in-plane ( $\Delta\phi$ ) and out-of-plane textures ( $\Delta\omega$ ) of all GdBCO films as a function of the Gd <sub>2</sub> O <sub>3</sub> doping content. ....	58
Fig. 2.3. (a) Electrical resistivity versus temperature curves, (b) the variation of the $T_{c,zero}$ and $\Delta T$ values with increasing Gd <sub>2</sub> O <sub>3</sub> doping contents for all GdBCO samples.....	59
Fig. 2.4. Magnetic $J_c$ versus applied field for all GdBCO films at (a) 20, (b) 40, (c) 65, and (d) 77 K.....	60
Fig. 2.5. The pinning force density ( $F_p = J_c \times B$ ) values at (a) 20, (b) 40, (c) 65, and (d) 77 K for $B//c$ as a function of the magnetic field for all samples. ....	61
Fig. 2.6. Field-orientation dependence of the transport $J_c$ values for undoped, 2 mol% and 5 mol% Gd <sub>2</sub> O <sub>3</sub> -doped GdBCO samples measured at 77 K, 1 T ....	62

Fig. 2.7. Cross-section HR-TEM images of 5 mol% Gd <sub>2</sub> O <sub>3</sub> -doped GdBCO film .....	63
Fig. 2.8. (a) Cross-section HR-TEM images and (b) FFT indexing diffraction data of 5 mol% Gd <sub>2</sub> O <sub>3</sub> -doped GdBCO film .....	64
Fig. 2.9. XRD patterns of all EuBCO films deposited on CeO <sub>2</sub> -buffered MgO (100) substrates [48].....	65
Fig. 2.10. The in-plane ( $\Delta\phi$ ) and out-of-plane textures ( $\Delta\omega$ ) of EuBCO films as a function of the Eu <sub>2</sub> O <sub>3</sub> doping content [48] .....	66
Fig. 2.11. (a) Electrical resistivity versus temperature curves, (b) the variation of the $T_{c,zero}$ and $\Delta T$ values with increasing Eu <sub>2</sub> O <sub>3</sub> doping contents for all EuBCO samples [48].....	67
Fig. 2.12. Magnetic $J_c$ versus magnetic field applied parallel to the $c$ -axis for pristine and 2-8 mol% Eu <sub>2</sub> O <sub>3</sub> -doped EuBCO films at (a) 20, (b) 40, (c) 65 and (d) 77 K [48].....	68
Fig. 2.13. The pinning force density ( $F_p = J_c \times B$ ) values at (a) 20, (b) 40, (c) 65 and (d) 77 K for $B//c$ as a function of the magnetic field for pristine and 2-8 mol% Eu <sub>2</sub> O <sub>3</sub> -doped EuBCO films [48].....	69
Fig. 2.14. Field-orientation dependence of the transport $J_c$ values for pristine, and 4 mol% Eu <sub>2</sub> O <sub>3</sub> -doped EuBCO samples measured at 77 K, 1 T.....	70
Fig. 2.15. Cross-sectional HR-TEM image (a) and FFT pattern (b) of 4 mol%	

Eu <sub>2</sub> O <sub>3</sub> -doped EuBCO films by PLD. ....	71
Fig. 2.16. The comparison of the $T_{c,zero}$ and $\Delta T$ values with increasing doping contents for Y <sub>2</sub> O <sub>3</sub> -doped YBCO by PLD [27], RE <sub>2</sub> O <sub>3</sub> -doped REBCO by PLD (RE = Eu, Gd [26]), BZO-doped YBCO by MOD [49], and GdBCO CCs by RCE-DR [50], REBCO samples .....	72
Fig. 2.17. (a) Eu/Ba elements ratio and (b) $c$ -axis lattice parameter as function of RE <sub>2</sub> O <sub>3</sub> doping contents.....	73
Fig. 2.18. (a) HAADF-STEM image of 4 mol% Eu <sub>2</sub> O <sub>3</sub> -doped EuBCO films, nanostrain maps of (b) $\epsilon_{xx}$ , (c) $\epsilon_{xz}$ , and (d) $\epsilon_{zz}$ .....	74
Fig. 3.1. XRD patterns of the GdBCO films (sample A (red) and sample B(black)) .....	87
Fig. 3.2. FE-SEM micrographs of (a) sample A and sample B. (c) Z-contrast images of the outgrowth for the top surface of sample A, and the Gd, Ba, Cu, and O spectral images .....	88
Fig. 3.3. Angular dependence of $J_c$ at 77 K in (a) 1 T, (b) 3 T, and (c) 5 T, and at 65 K in (d) 1 T, (e) 3 T, and (f) 5 T for both the sample A and B .....	89
Fig. 3.4. Cross-sectional STEM micrographs of both the sample A and sample B .....	90
Fig. 3.5. Cross-sectional BF STEM micrographs of both the sample A (a) and B (b) .....	91

Fig. 3.6. HAADF STEM images of the sample A (a) and sample B (c), and reconstructed masked inverse FFT images for the sample A (b) and sample B (d) analyzed for the square area related by red dashed line in (a) and (c).....	92
Fig. 3.7. Schematic of the pinning model for the SFs acting as the <i>c</i> -axis related pinning center.....	93
Fig. 4.1. Angular dependence of $J_c$ values ( $B, \theta, T$ ) (a) at 77 K in 1 T, (b) at 77 K in 3 T, (c) at 65 K in 3 T, and (d) at 65 K in 7 T for pristine and GdBCO CCs annealed at 750°C in the $PO_2$ of 300 mTorr for 5, 15 and 30 min .....	120
Fig. 4.2. Cross-sectional TEM images of pristine and post-annealed GdBCO CCs for 15 min. (Red arrows indicate the SFs).....	121
Fig. 4.3. XRD patterns of pristine and GdBCO CCs post-annealed (a) at 750°C in the $PO_2$ of 300 mTorr for 5, 15, 30 and 60 min and (b) at 750°C in the $PO_2$ of 10, 30, 300 and 1000 mTorr for 15 min .....	122
Fig. 4.4. STEM images of the pristine and post-annealed GdBCO CCs for 15 min. HAADF-STEM images show that the SFs were piled up along the <i>c</i> -axis of the GdBCO CCs (red arrows).....	123
Fig. 4.5. Angular dependence of $J_c$ value ( $B, \theta, T$ ) at 77 K in (a) 1 T, and (b) 5 T compared with 10, 30, and 300 mTorr. ....	124
Fig. 4.6. Theta-2theta ( $\theta$ - $2\theta$ ) scans of samples. As-grown pristine GdBCO CCs samples were post-annealed at 450, 500, 550, 600, 650, and 750°C in the $PO_2$ of 300 mTorr from 20° to 70° (a) and from 17° to 40° (b).....	125

Fig. 4.7. Cross-sectional TEM micrographs of pristine sample and GdBCO CCs annealed at 500°C (1 h) and 750°C (5 min) in the  $PO_2$  of 300 mTorr. The SFs are indicated by red arrows .....126

Fig. 4.8. Cross-sectional STEM micrographs of pristine sample and GdBCO CCs annealed at 500°C in the  $PO_2$  of 300 mTorr for 1 h (a) and EDS elemental mapping (b). The CuO phases are indicated by red arrows .....127

Fig. 4.9. Magnified HAADF images are indicated by red rectangular (a) and white rectangular (c) in Fig. 3 for GdBCO CCs annealed at 500°C in the  $PO_2$  of 300 mTorr for 1 h. High resolution HAADF images are noted by red rectangular (b) and (d).....128

Fig. 4.10. High resolution HAADF images showing the distribution of SFs near the CuO phase in the GdBCO matrix for GdBCO CCs annealed at 500°C in the  $PO_2$  of 300 mTorr for 1 h. The red arrows indicate the double CuO planes .....129

Fig. 4.11. Atomic scale resolution HAADF images showing the double CuO planes (a) and single CuO planes (b) .....130

Fig. 4.12. The field angle dependency  $J_c$  of both the pristine sample and post-annealed GdBCO CCs (a) at 77 K in 1 T, (b) at 77 K in 5 T, (c) at 65 K in 3 T, (d) at 65 K in 7 T, (e) at 50 K in 11 T, and (f) at 50 K in 13 T .....131

Fig. 4.13. The  $J_{c,min}$  values of pristine sample and post-annealed GdBCO CCs versus the applied fields at 77, 65, and 50 K.....132

# Chapter 1. General Introduction

## 1.1. High temperature superconductor

Since the high temperature superconductor (HTS) was discovered in 1986 [1], the promising HTS materials which possessed higher critical temperatures ( $T_c$ ) and critical current density ( $J_c$ ) have attracted attentions of many researchers. Especially, there have been significant efforts to applying the HTS materials in electrical power system [2]. The first generation (1G) HTS wire, which is the Bi-Sr-Ca-Cu-O (BSCCO) with  $T_c$  of 110 K, was utilized in the practical applications. The BSCCO wires using the powder-in-tube (PIT) process have several limitation such as low  $J_c$  due to high angle boundaries, low irreversibility field ( $H_{irr}$ ) and high processing cost for utilizing the practical applications [2, 3]. However, the second generation (2G) materials like the  $\text{YBa}_2\text{Cu}_3\text{O}_{7-\delta}$  (YBCO) and  $\text{REBa}_2\text{Cu}_3\text{O}_{7-\delta}$  (REBCO, RE: light rare earths) have considerable advantages in the superconducting properties compared with 1<sup>st</sup> HTS wires [2]. Up to now, YBCO and REBCO wires have successfully utilized and reached practical applications such as magnet, motors, transformers, generators, transmission cables, and etc. in Fig. 1.1 [4].

As shown in Fig. 1.2, the crystal structure of the YBCO and REBCO system is a layered perovskite with orthorhombic symmetry, resulting in the strong anisotropy. In REBCO system, the structure is formed by sequential copper oxide chains, which contain conducting and charge reservoir layers. In particular, the crystallographic unit cell contains varying number of  $\text{CuO}_2$

planes as well as CuO chain depending on stoichiometry, indicating that the  $T_c$  values of these system are varied by the oxygen contents in Fig. 1.3 [5]. The  $\delta$  values of the oxygen contents can vary from 0 to 1 [6]. Depending on the oxygen contents, the REBCO system show two crystalline structure consisting of the tetragonal with  $\delta > 0.5$  and orthorhombic structure with  $\delta < 0.5$  as shown in Fig. 1.4 [7]. Depending on the oxygen annealing temperatures, the structure becomes tetragonal at high temperature, and transition from tetragonal phase to orthorhombic phase at relatively low temperature. Especially, the REBCO system have specific structural properties compared with YBCO system. It is well known that REBCO compounds tend to form  $RE_{1+x}Ba_{2-x}Cu_3O_{7-\delta}$ -type solid solutions due to the similarity in the ionic radius of  $RE^{3+}$  and  $Ba^{2+}$  [8].

One of critical issues for the practical application of REBCO is the improvement of pinning properties. To improve the in-field performance of REBCO CCs, it is very important to incorporate the artificial pinning centers (APCs) into the superconducting matrix. When the size of pinning center is comparable to coherence length, the vortex would be effectively pinned by pinning center. As such an effort, many research groups tried to improve pinning properties of REBCO CCs by refining the second phases. Further details of defects and APCs will be explained below in 1.2.

In order to applying the YBCO and REBCO compound to the practical applications, these materials should be fabricated by the coated conductors (CCs). So far, there were numerous attempts in worldwide R&D activities to develop high quality CCs and electric power systems [9]. These materials can be successfully fabricated by various deposition methods such as pulsed laser deposition (PLD), metal organic deposition (MOD), metal organic chemical

deposition (MOCVD), and reactive co-evaporation deposition & reaction (RCE-DR) on flexible metal substrate. As shown in Fig. 1. 5, the typical structure of 2G HTS CCs is the following: protecting layer/superconducting layer/buffer layer/IBAD-MgO layer/seed layer/diffusion barrier layer/metal substrates [10]. Further details of processing methods will be explained in chapter 1.3.

## **1.2. Flux pinning of REBCO superconductor**

In order to improve the performance of REBCO CCs in magnetic field, it is important to introduce the APCs into the superconducting matrix. Basically, the superconducting state will disappear above critical field ( $H_c$ ). Unlike the type I superconductor, the magnetic fields penetrate through the matrix when the magnitude of magnetic fields is between lower critical fields ( $H_{c1}$ ) and upper critical field ( $H_{c2}$ ), called mixed state or vortex state, in the type II superconductor. In the vortex state, the quantized flux lines try to move by a Lorentz force ( $F_L = J \times B$ ). The flux lines can be effectively pinned by pinning centers.

### **1.2.1. Flux pinning mechanism**

The important feature of superconductor is the perfect diamagnetism, implying that the applied field is completely expelled below  $H_c$ . Superconductors are categorized into type I and type II whether or the superconductors have the vortex state. According to the Ginzberg-Landau

equation, type I superconductor shows the case with  $\kappa < 1/\sqrt{2}$  ( $\kappa = \lambda/\xi$ ) while type II superconductor exhibits the case with  $\kappa > 1/\sqrt{2}$  [11]. As shown in Fig. 1. 6(b), type II superconductors have two critical fields ( $H_{c1}$  and  $H_{c2}$ ). In the magnetic fields ranging from  $H_{c1}$  to  $H_{c2}$ , the magnetic fields exist in the form of quantized flux lines. Each flux line is characterized by a vortex of which diameter is the superconducting current  $\sim 2\lambda$ , surrounding a normal core of a diameter  $\sim 2\xi$ . Fig. 1.7 shows that the quantized flux lines are moved by the Lorentz force which is generated by the applied field and the current [12]. With increasing applied fields or current, the intensity of Lorentz force is increased, resulting in the significant degradation of critical current ( $I_c$ ). In order to hinder the movement of the vortex, the pinning force should be higher than the Lorentz force.

In order to increase the in-field  $J_c$ , we have to pin the flux lines by introducing appropriate defects, where flux lines stay stably. Therefore, the vortex pinning technology holds the key for improving the in-field  $J_c$  values. REBCO films have various defects, which is naturally generated in the superconducting matrix, such as oxygen vacancies [13, 14], cation disorder [15], dislocation [16-20], small angle boundaries [20, 21], twin boundaries [22, 23], anti-phase boundaries [24], stacking faults (SFs) [25-28], and etc. as shown in Fig. 1. 8 [29]. These defects can act as pinning centers. However, the improvement of pinning properties by these natural defects is significantly limited due to the difficulty in engineering defect landscape. Therefore, it is necessary to introduce nano-sized second phase such as APCs into the superconducting matrix to obtain further improved pinning properties.

### 1.2.2. Artificial pinning centers (APCs) in HTS

As we mentioned, the APCs should be introduced into superconducting matrix to obtain the high  $J_c$  values of REBCO films in high magnetic fields. According to the dimension of pinning centers, the pinning centers can be classified by 0 dimension (0D) APCs, 1 dimension (1D) APCs, 2 dimension (2D) APCs, and 3 dimension (3D) APCs as shown in Fig. 1. 9 [30]. The details of defects are as followings; 0D-APCs such as oxygen vacancies and point defects [13-15]; 1D-APCs such as columnar defects and dislocations [16-20, 31-34]; 2D-APC such as low angle grain boundaries, twin boundaries, and SFs [20-28]; 3D-APC such as nanoparticles [35-37]. Also, the combination of 1D-APCs + 3D-APCs was reported [38].

The point defects like 0D-APCs which are smaller than  $\xi^3$  can act as effective pinning centers at low temperature in high field region [39]. These defects are atomic-scale structure and can be formed by the substitution between the RE and Ba elements due to the similarity to the ion sizes [29]. So far, the strongest defect to improve  $J_c$  values for  $B//c$  is a columnar defect so called 1D-APCs. Especially, the nanorods which are aligned to  $c$ -axis in the matrix cause the significant improvement of in-field  $J_c$  values in high magnetic fields. The interface region between the matrix and nanorods contains the misfit dislocations and strain-induced oxygen vacancies, resulting in the improvement of  $J_c$  values [40]. However, the 1D-APCs have the critical drawback in terms of the magnetic field direction due to the anisotropic  $J_c$  behaviour. The orientation of the APCs in the superconducting matrix affects the angular dependence of  $J_c$  values. In contrast to the 1D-APCs, the 3D-APCs are round-

shape nanoparticles, indicating that the nanoparticles can pin the flux lines in the whole magnetic fields.

The schematics of a pinned flux lines by 1D-APCs or 3D-APCs are represented in Fig. 1.10 [41]. In the case of 1D-APCs, the pinned vortex line comes out from nanorods when the magnetic field is tilted from the direction of nanorods, representing in the zigzag state. The portion of the vortex line pinned by the nanorods is reduced. With increasing the current density or the magnetic fields, the Lorentz force increases, leading to the depinning of flux lines. In terms of 3D-APCs, however, flux lines are easily pinned by nanoparticles due to the random orientation of pinning centers. Therefore, 3D-APCs shows more isotropic  $J_c$  behavior compared with 1D-APCs.

### **1.3. REBCO films by various fabrication technologies**

There are various technologies such as PLD, MOCVD, MOD, and RCE-DR for the fabrication of REBCO films. The details of these fabrication technologies will be briefly introduced below in 1.3.1, 1.3.2, 1.3.3, and 1.3.4. The pinning behaviors of REBCO films by these fabrication technologies are quite different. Above all, the dimension of the APCs is varied by fabrication methods due to the different growth mechanism. For example, the BaZrO<sub>3</sub> (BZO) compound can be formed as nanorods in the PLD process but as nanoparticles in the MOD process [32, 42]. In the case of an *in-situ* annealing process such as PLD and MOCVD, the nucleation and growth of the REBCO superconducting matrix and the APCs occur simultaneously. Therefore, the formation of APCs can be directly affected by the growth condition of REBCO

matrix. However, the MOD and RCE-DR process are an *ex-situ* annealing process. In these processes, the APCs were pre-formed in a precursor film before the growth of the REBCO matrix. Therefore, the APCs trapped in the superconducting matrix show the randomly oriented structure.

As shown in Fig. 1. 11, we summarize the minimum critical current density ( $J_{c,min}$ ) and  $J_c$  values for  $B//c$  of REBCO films at 77 K 1 T as a function of fabrication technologies among the recently reported studies [33-36, 43-66]. The maximum  $J_c$  value for  $B//c$  is observable in the PLD process. However, the highest  $J_{c,min}$  value is observable in the MOD process. As we mentioned in chapter 1.2.2, the 1D-APCs have limitation to improve  $J_c$  values in the whole magnetic field except for  $c$ -axis direction.

In order to overcome the disadvantage of 1D-APC, we have tried to fabricate the REBCO films with  $RE_2O_3$  nanoparticles using the modified surface target in the PLD process. The details will be described in chapter 2. Additionally, we identified the origin of  $J_c$  peak along the  $c$ -axis direction for the GdBCO films by PLD (chapter 3). Also, we have tried to improve pinning properties the GdBCO CCs via RCE-DR by controlling the density of SFs since the GdBCO CCs by RCE-DR have relatively week pinning properties compared to other processes (Fig. 1. 11). The details for the improved pinning properties of GdBCO CCs by RCE-DR will be introduced in chapter 4.

### **1.3.1. Pulsed laser deposition (PLD)**

The PLD process is a kind of the physical vapor deposition (PVD), which carried out in a vacuum system. As shown in Fig. 1. 12, PLD system consists

of a laser source, an optical system, and vacuum system. The laser sources can be categorized by the ArF ( $\lambda = 193$  nm), KrF ( $\lambda = 248$  nm), and XeF ( $\lambda = 260$  nm) excimer laser or the Nd:YAG ( $\lambda = 355$  nm). It also includes a mold or halogen heater, a heating stage, and a rotating target holder. Pulsed lasers pass through the aligned mirrors and are focused on the target. One of the crucial features is that the composition of deposited film is similar to the target composition. Due to this advantage, the PLD process is widely employed in the fabrication of the REBCO films possessing the high pinning properties. So far, several companies such as Bruker, Fujikura, SuperOx, and Sumitomo have fabricated REBCO CCs by PLD and scaled up to production long length [67-71].

### **1.3.2. Metal-organic chemical vapor deposition (MOCVD)**

MOCVD is a chemical vapor deposition (CVD) technique using metal organic sources as precursor materials. MOCVD contains the process that the vaporized gas phases from liquid precursor phase are transferred by a carrier gas to the substrate. The transferred gas phases are decomposed on the substrates and then, the deposition occurs via a chemical reaction at the surface of the substrate. One of the most important features is that it is possible to precisely control the composition of the REBCO films for the large area deposition. Additionally, it is possible to easily insert the pinning materials and continuously modify film composition during growth [72]. However, the slow growth rate and high price of precursor materials cause the higher cost for the fabrication of long-lengths CCs. Among the manufacturers of CCs, Superpower

Inc. produces REBCO CCs by the MOCVD process [73].

### **1.3.3. Metal-organic deposition (MOD)**

MOD is the process using a solution as a precursor. It also called as chemical solution deposition (CSD). The MOD process is based on the *ex-situ* growth technique unlike the PLD and MOCVD process (*in-situ* growth). The coating solution is pyrolyzed and fired at a high temperature to grow on the substrate. Compared with the PLD and MOCVD process, the MOD process is known to be cost-effective since the high vacuum system is unnecessary to fabricate REBCO films. The trifluoroacetic acid (TFA)-MOD process of YBCO films was firstly reported in 1988 [74]. The TFA-MOD process has been up to achieve high quality REBCO films. However, it has been a challenging problem to produce thick films with high  $I_c$  due to a macroscopic crack formation and a long decomposition time of organic components. Alternatively, the fluorine-free MOD process has been developed and reported [75-77]. From now on, AMSC Co., Ltd produces commercial REBCO HTS CCs [78].

### **1.3.4. Reactive co-evaporation deposition & reaction (RCE-DR)**

The RCE-DR process has been developed by SuNAM Co. in Korea. Basically, the RCE-DR process is a two-step *ex-situ* process as shown in Fig. 1.13. Firstly, an amorphous precursor film which consists of Gd, Ba, and Cu elements is deposited on LaMnO<sub>3</sub> (LMO)-buffered IBAD MgO templates using high energy e-beam evaporation. Each metal element is controlled by the QCM

and automatic control program. The nominal composition of the amorphous film is Gd : Ba : Cu  $\approx$  1 : 1 : 2.5. As-deposited amorphous films are transferred from lower  $PO_2$  zone of  $\sim 10^{-5}$  Torr to higher  $PO_2$  zone of  $\sim 150$  mTorr and pass this zone for 2 min to grow thick GdBCO layer in a reel-to-reel furnace at  $860^\circ\text{C}$  [79]. According to growth mechanism of GdBCO by RCE-DR, the amorphous film is converted into  $\text{Gd}_2\text{O}_3$  + liquid phase and finally grown to the GdBCO film by the peritectic recombination reaction [79]. Due to the growth mechanism of GdBCO superconducting layers, the RCE-DR process has the advantages of a high throughput and high  $J_c$  at 77 K in self-field compared with the CCs of other manufacturers [80]. However, in-field  $J_c$  values are lower than those of REBCO CCs from other companies, indicating that the pinning properties of the GdBCO CCs by the RCE-DR process should be improved.

## References

- [1] J. G. Bednorz and K. A. Müller, "Possible high $T_c$  superconductivity in the Ba–La–Cu–O system," *Zeitschrift für Physik B Condensed Matter*, vol. 64, no. 2, pp. 189-193, 1986.
- [2] D. Larbalestier, A. Gurevich, D. M. Feldmann, and A. Polyanskii, "High- $T_c$  superconducting materials for electric power applications," *Nature*, pp. 311-320, 2001.
- [3] Y. Yan, W. Lo, J. Evetts, A. Campbell, and W. Stobbs, "Lower  $T_c$  barriers at high angle boundaries in the  $(\text{BiPb})_2\text{Sr}_2\text{Ca}_2\text{Cu}_3\text{O}_x$  system," *Applied physics letters*, vol. 67, no. 17, pp. 2554-2556, 1995.
- [4] Fujikura website,  
"<http://www.fujikura.com/solutions/superconductingwire>."
- [5] V. Breit, P. Schweiss, R. Hauff, H. Wühl, H. Claus, H. Rietschel, A. Erb, and G. Müller-Vogt, "Evidence for chain superconductivity in near-stoichiometric  $\text{YBa}_2\text{Cu}_3\text{O}_x$  single crystals," *Physical Review B*, vol. 52, no. 22, p. R15727, 1995.
- [6] J. Jorgensen, M. A. Beno, D. G. Hinks, L. Soderholm, K. Volin, R. Hitterman, J. Grace, I. K. Schuller, C. Segre, and K. Zhang, "Oxygen ordering and the orthorhombic-to-tetragonal phase transition in  $\text{YBa}_2\text{Cu}_3\text{O}_{7-x}$ ," *Physical Review B*, vol. 36, no. 7, p. 3608, 1987.
- [7] J. Jorgensen, B. Veal, A. P. Paulikas, L. Nowicki, G. Crabtree, H. Claus, and W. Kwok, "Structural properties of oxygen-deficient  $\text{YBa}_2\text{Cu}_3\text{O}_{7-\delta}$ ," *Physical Review B*, vol. 41, no. 4, p. 1863, 1990.
- [8] K. Zhang, B. Dabrowski, C. Segre, D. Hinks, I. K. Schuller, J. Jorgensen, and M. Slaski, "Solubility and superconductivity in  $\text{RE}(\text{Ba}_{2-x}\text{RE}_x)\text{Cu}_3\text{O}_{7+\delta}$  systems (RE= Nd, Sm, Eu, Gd, Dy)," *Journal of Physics C: Solid State Physics*, vol. 20, no. 34, p. L935, 1987.
- [9] Y. Shiohara, T. Taneda, and M. Yoshizumi, "Overview of materials and

- power applications of coated conductors project," *Japanese Journal of Applied Physics*, vol. 51, no. 1R, p. 010007, 2011.
- [10] O. Kwon, K. Kim, Y. Choi, H. Shin, S. Hahn, Y. Iwasa, and H. Lee, "Effects of turn-to-turn compactness in the straight sections of HTS racetrack coils on thermal and electrical characteristics," *Superconductor Science and Technology*, vol. 26, no. 8, p. 085025, 2013.
- [11] M. Tinkham, *Introduction to superconductivity*. Courier Corporation, 2004.
- [12] H. Yamasaki, K. Ohki, I. Yamaguchi, M. Sohma, W. Kondo, H. Matsui, T. Manabe, and T. Kumagai, "Strong flux pinning due to dislocations associated with stacking faults in  $\text{YBa}_2\text{Cu}_3\text{O}_{7-\delta}$  thin films prepared by fluorine-free metal organic deposition," *Superconductor Science and Technology*, vol. 23, no. 10, p. 105004, 2010.
- [13] M. Daeumling, J. Seuntjens, and D. Larbalestier, "Oxygen-defect flux pinning, anomalous magnetization and intra-grain granularity in  $\text{YBa}_2\text{Cu}_3\text{O}_{7-\delta}$ ," *Nature*, vol. 346, no. 6282, p. 332, 1990.
- [14] T. Hylton and M. Beasley, "Flux-pinning mechanisms in thin films of  $\text{YBa}_2\text{Cu}_3\text{O}_x$ ," *Physical Review B*, vol. 41, no. 16, p. 11669, 1990.
- [15] V. Maroni, Y. Li, D. Feldmann, and Q. Jia, "Correlation between cation disorder and flux pinning in the  $\text{YBa}_2\text{Cu}_3\text{O}_7$  coated conductor," *Journal of Applied Physics*, vol. 102, no. 11, p. 113909, 2007.
- [16] R. Schalk, K. Kundzins, H. Weber, E. Stangl, S. Proyer, and D. Bäuerle, "STM observation of dislocation chains suitable for flux pinning in  $\text{YBa}_2\text{Cu}_3\text{O}_{7-x}$  films," *Physica C: Superconductivity and its applications*, vol. 257, no. 3-4, pp. 341-354, 1996.
- [17] B. Dam, J. Huijbregtse, F. Klaassen, R. Van der Geest, G. Doornbos, J. Rector, A. Testa, S. Freisem, J. Martinez, and B. Stäuble-Pümpin, "Origin of high critical currents in  $\text{YBa}_2\text{Cu}_3\text{O}_{7-\delta}$  superconducting thin films," *Nature*, vol. 399, no. 6735, p. 439, 1999.

- [18] F. Klaassen, G. Doornbos, J. Huijbregtse, R. Van der Geest, B. Dam, and R. Griessen, "Vortex pinning by natural linear defects in thin films of  $\text{YBa}_2\text{Cu}_3\text{O}_{7-\delta}$ ," *Physical Review B*, vol. 64, no. 18, p. 184523, 2001.
- [19] J. Huijbregtse, F. Klaassen, A. Szepielow, J. Rector, B. Dam, R. Griessen, B. Kooi, and J. T. M. De Hosson, "Vortex pinning by natural defects in thin films of  $\text{YBa}_2\text{Cu}_3\text{O}_{7-\delta}$ ," *Superconductor Science and Technology*, vol. 15, no. 3, p. 395, 2002.
- [20] V. Pan, Y. Cherpak, V. Komashko, S. Pozigun, C. Tretiatchenko, A. Semenov, E. Pashitskii, and A. V. Pan, "Supercurrent transport in  $\text{YBa}_2\text{Cu}_3\text{O}_{7-\delta}$  epitaxial thin films in a dc magnetic field," *Physical review B*, vol. 73, no. 5, p. 054508, 2006.
- [21] D. Agassi, D. Christen, and S. Pennycook, "Flux pinning and critical currents at low-angle grain boundaries in high-temperature superconductors," *Applied physics letters*, vol. 81, no. 15, pp. 2803-2805, 2002.
- [22] W. Kwok, U. Welp, G. Crabtree, K. Vandervoort, R. Hulscher, and J. Liu, "Direct observation of dissipative flux motion and pinning by twin boundaries in  $\text{YBa}_2\text{Cu}_3\text{O}_{7-\delta}$  single crystals," *Physical review letters*, vol. 64, no. 8, p. 966, 1990.
- [23] B. Roas, L. Schultz, and G. Saemann-Ischenko, "Anisotropy of the critical current density in epitaxial  $\text{YBa}_2\text{Cu}_3\text{O}_x$  films," *Physical review letters*, vol. 64, no. 4, p. 479, 1990.
- [24] C. Jooss, R. Warthmann, and H. Kronmüller, "Pinning mechanism of vortices at antiphase boundaries in  $\text{YBa}_2\text{Cu}_3\text{O}_{7-\delta}$ ," *Physical Review B*, vol. 61, no. 18, p. 12433, 2000.
- [25] M. Kramer, "Processing controlled stacking faults in  $\text{YBa}_2\text{Cu}_3\text{O}_{7-\delta}$  and their effect on flux pinning," *Applied physics letters*, vol. 58, no. 10, pp. 1086-1088, 1991.
- [26] Y. Jia, U. Welp, G. Crabtree, W. Kwok, A. Malozemoff, M. Rupich, S. Fleshler, and J. Clem, "Microstructure dependence of the c-axis critical

- current density in second-generation YBCO tapes," *Journal of Applied Physics*, vol. 110, no. 8, p. 083923, 2011.
- [27] E. Talantsev, N. Strickland, S. Wimbush, J. Storey, J. Tallon, and N. Long, "Hole doping dependence of critical current density in  $\text{YBa}_2\text{Cu}_3\text{O}_{7-\delta}$  conductors," *Applied Physics Letters*, vol. 104, no. 24, p. 242601, 2014.
- [28] A. Puichaud, S. Wimbush, and R. Knibbe, "Enhanced low-temperature critical current by reduction of stacking faults in REBCO coated conductors," *Superconductor Science and Technology*, vol. 30, no. 7, p. 074005, 2017.
- [29] S. Foltyn, L. Civale, J. MacManus-Driscoll, Q. Jia, B. Maiorov, H. Wang, and M. Maley, "Materials science challenges for high-temperature superconducting wire," *Nature materials*, vol. 6, no. 9, p. 631, 2007.
- [30] X. Obradors and T. Puig, "Coated conductors for power applications: materials challenges," *Superconductor Science and Technology*, vol. 27, no. 4, p. 044003, 2014.
- [31] L. Civale, "Vortex pinning and creep in high-temperature superconductors with columnar defects," *Superconductor Science and Technology*, vol. 10, no. 7A, p. A11, 1997.
- [32] J. MacManus-Driscoll, S. Foltyn, Q. Jia, H. Wang, A. Serquis, L. Civale, B. Maiorov, M. Hawley, M. Maley, and D. Peterson, "Strongly enhanced current densities in superconducting coated conductors of  $\text{YBa}_2\text{Cu}_3\text{O}_{7-x}+\text{BaZrO}_3$ ," *Nature materials*, vol. 3, no. 7, p. 439, 2004.
- [33] A. Xu, L. Delgado, N. Khatri, Y. Liu, V. Selvamanickam, D. Abraimov, J. Jaroszynski, F. Kametani, and D. Larbalestier, "Strongly enhanced vortex pinning from 4 to 77 K in magnetic fields up to 31 T in 15 mol.% Zr-added (Gd,Y)-Ba-Cu-O superconducting tapes," *Apl Materials*, vol. 2, no. 4, p. 046111, 2014.
- [34] S. Miura, Y. Yoshida, Y. Ichino, K. Matsumoto, A. Ichinose, and S.

- Awaji, "Characteristics of high-performance BaHfO<sub>3</sub>-doped SmBa<sub>2</sub>Cu<sub>3</sub>O<sub>y</sub> superconducting films fabricated with a seed layer and low-temperature growth," *Superconductor Science and Technology*, vol. 28, no. 6, p. 065013, 2015.
- [35] A. Llordes, A. Palau, J. Gázquez, M. Coll, R. Vlad, A. Pomar, J. Arbiol, R. Guzman, S. Ye, and V. Rouco, "Nanoscale strain-induced pair suppression as a vortex-pinning mechanism in high-temperature superconductors," *Nature materials*, vol. 11, no. 4, p. 329, 2012.
- [36] P. Mele, R. Guzman, J. Gazquez, T. Puig, X. Obradors, S. Saini, Y. Yoshida, M. Mukaida, A. Ichinose, and K. Matsumoto, "High pinning performance of YBa<sub>2</sub>Cu<sub>3</sub>O<sub>7-x</sub> films added with Y<sub>2</sub>O<sub>3</sub> nanoparticulate defects," *Superconductor Science and Technology*, vol. 28, no. 2, p. 024002, 2014.
- [37] M. Miura, B. Maiorov, M. Sato, M. Kanai, T. Kato, T. Kato, T. Izumi, S. Awaji, P. Mele, and M. Kiuchi, "Tuning nanoparticle size for enhanced functionality in perovskite thin films deposited by metal organic deposition," *NPG Asia Materials*, vol. 9, no. 11, p. e447, 2017.
- [38] T. Horide, T. Kawamura, K. Matsumoto, A. Ichinose, M. Yoshizumi, T. Izumi, and Y. Shiohara, "J<sub>c</sub> improvement by double artificial pinning centers of BaSnO<sub>3</sub> nanorods and Y<sub>2</sub>O<sub>3</sub> nanoparticles in YBa<sub>2</sub>Cu<sub>3</sub>O<sub>7</sub> coated conductors," *Superconductor Science and Technology*, vol. 26, no. 7, p. 075019, 2013.
- [39] J. Feighan, A. Kursumovic, and J. MacManus-Driscoll, "Materials design for artificial pinning centres in superconductor PLD coated conductors," *Superconductor Science and Technology*, vol. 30, no. 12, p. 123001, 2017.
- [40] T. Horide, F. Kametani, S. Yoshioka, T. Kitamura, and K. Matsumoto, "Structural Evolution Induced by Interfacial Lattice Mismatch in Self-Organized YBa<sub>2</sub>Cu<sub>3</sub>O<sub>7-δ</sub> Nanocomposite Film," *ACS nano*, vol. 11, no. 2, pp. 1780-1788, 2017.

- [41] K. Matsumoto and P. Mele, "Artificial pinning center technology to enhance vortex pinning in YBCO coated conductors," *Superconductor Science and Technology*, vol. 23, no. 1, p. 014001, 2009.
- [42] J. Gutierrez, A. Llordes, J. Gazquez, M. Gibert, N. Roma, S. Ricart, A. Pomar, F. Sandiumenge, N. Mestres, and T. Puig, "Strong isotropic flux pinning in solution-derived  $\text{YBa}_2\text{Cu}_3\text{O}_{7-x}$  nanocomposite superconductor films," *Nature materials*, vol. 6, no. 5, p. 367, 2007.
- [43] N. Strickland, N. Long, E. Talantsev, P. Hoefakker, J. Xia, M. Rupich, T. Kodenkandath, W. Zhang, X. Li, and Y. Huang, "Enhanced flux pinning by  $\text{BaZrO}_3$  nanoparticles in metal-organic deposited YBCO second-generation HTS wire," *Physica C: Superconductivity*, vol. 468, no. 3, pp. 183-189, 2008.
- [44] T. J. Haugan, F. J. Baca, M. J. Mullins, N. A. Pierce, T. A. Campbell, E. L. Brewster, P. N. Barnes, H. Wang, and M. D. Sumption, "Temperature and magnetic field dependence of critical current density of YBCO with varying flux pinning additions," *IEEE Transactions on Applied Superconductivity*, vol. 19, no. 3, pp. 3270-3274, 2009.
- [45] B. Maiorov, S. Baily, H. Zhou, O. Ugurlu, J. Kennison, P. Dowden, T. Holesinger, S. Foltyn, and L. Civale, "Synergetic combination of different types of defect to optimize pinning landscape using  $\text{BaZrO}_3$ -doped  $\text{YBa}_2\text{Cu}_3\text{O}_7$ ," *Nature materials*, vol. 8, no. 5, p. 398, 2009.
- [46] M. Coll, S. Ye, V. Rouco, A. Palau, R. Guzman, J. Gazquez, J. Arbiol, H. Suo, T. Puig, and X. Obradors, "Solution-derived  $\text{YBa}_2\text{Cu}_3\text{O}_7$  nanocomposite films with a  $\text{Ba}_2\text{YTao}_6$  secondary phase for improved superconducting properties," *Superconductor Science and Technology*, vol. 26, no. 1, p. 015001, 2012.
- [47] M. Miura, B. Maiorov, J. Willis, T. Kato, M. Sato, T. Izumi, Y. Shiohara, and L. Civale, "The effects of density and size of  $\text{BaMO}_3$  (M= Zr, Nb, Sn) nanoparticles on the vortex glassy and liquid phase in (Y, Gd) $\text{Ba}_2\text{Cu}_3\text{O}_y$  coated conductors," *Superconductor Science and*

- Technology*, vol. 26, no. 3, p. 035008, 2013.
- [48] S. H. Wee, Y. L. Zuev, C. Cantoni, and A. Goyal, "Engineering nanocolumnar defect configurations for optimized vortex pinning in high temperature superconducting nanocomposite wires," *Scientific reports*, vol. 3, p. 2310, 2013.
- [49] G. Ercolano, M. Bianchetti, S.-L. Sahonta, A. Kursumovic, J. Lee, H. Wang, and J. MacManus-Driscoll, "Strong correlated pinning at high growth rates in  $\text{YBa}_2\text{Cu}_3\text{O}_{7-x}$  thin films with  $\text{Ba}_2\text{YNbO}_6$  additions," *Journal of Applied Physics*, vol. 116, no. 3, p. 033915, 2014.
- [50] K.-P. Ko, S.-M. Choi, J.-W. Lee, R.-K. Ko, S.-H. Moon, C. Park, and S.-I. Yoo, "Optimization of the  $\text{BaSnO}_3$  Doping Content in  $\text{GdBa}_2\text{Cu}_3\text{O}_{7-\delta}$  Coated Conductors by Pulsed Laser Deposition," *IEEE Transactions on Applied Superconductivity*, vol. 24, no. 6, pp. 1-8, 2014.
- [51] J. MacManus-Driscoll, M. Bianchetti, A. Kursumovic, G. Kim, W. Jo, H. Wang, J. Lee, G. Hong, and S. Moon, "Strong pinning in very fast grown reactive co-evaporated  $\text{GdBa}_2\text{Cu}_3\text{O}_7$  coated conductors," *APL Materials*, vol. 2, no. 8, p. 086103, 2014.
- [52] A. Tsuruta, Y. Yoshida, Y. Ichino, A. Ichinose, K. Matsumoto, and S. Awaji, "The influence of the geometric characteristics of nanorods on the flux pinning in high-performance  $\text{BaMO}_3$ -doped  $\text{SmBa}_2\text{Cu}_3\text{O}_y$  films (M= Hf, Sn)," *Superconductor Science and Technology*, vol. 27, no. 6, p. 065001, 2014.
- [53] S.-M. Choi, J.-W. Lee, J.-H. Lee, S.-H. Moon, and S.-I. Yoo, "The Effect of Growth Temperature on  $\text{GdBa}_2\text{Cu}_3\text{O}_{7-\delta}$  Coated Conductors Fabricated by the RCE-DR Process," *IEEE Transactions on Applied Superconductivity*, vol. 25, no. 3, pp. 1-5, 2015.
- [54] M. Erbe, J. Hänisch, R. Hühne, T. Freudenberg, A. Kirchner, L. Molina-Luna, C. Damm, G. Van Tendeloo, S. Kaskel, and L. Schultz, " $\text{BaHfO}_3$  artificial pinning centres in TFA-MOD-derived YBCO and GdBCO thin films," *Superconductor Science and Technology*, vol. 28,

- no. 11, p. 114002, 2015.
- [55] L. Jin, S. Zhang, Z. Yu, C. Li, J. Feng, A. Sulpice, Y. Wang, and P. Zhang, "Influences of BaZrO<sub>3</sub> particles on the microstructure and flux pinning of YBCO film prepared by using modified TFA-MOD approach," *Materials Chemistry and Physics*, vol. 149, pp. 188-192, 2015.
- [56] S. Miura, Y. Yoshida, Y. Ichino, A. Tsuruta, K. Matsumoto, A. Ichinose, and S. Awaji, "Vortex pinning at low temperature under high magnetic field in SmBa<sub>2</sub>Cu<sub>3</sub>O<sub>y</sub> superconducting films with high number density and small size of BaHfO<sub>3</sub> nano-rods," *Superconductor Science and Technology*, vol. 28, no. 11, p. 114006, 2015.
- [57] V. Selvamanickam, M. H. Gharahcheshmeh, A. Xu, E. Galstyan, L. Delgado, and C. Cantoni, "High critical currents in heavily doped (Gd,Y)Ba<sub>2</sub>Cu<sub>3</sub>O<sub>x</sub> superconductor tapes," *Applied Physics Letters*, vol. 106, no. 3, p. 032601, 2015.
- [58] A. Xu, J. Jaroszynski, F. Kametani, and D. Larbalestier, "Broad temperature range study of J<sub>c</sub> and H<sub>irr</sub> anisotropy in YBa<sub>2</sub>Cu<sub>3</sub>O<sub>x</sub> thin films containing either Y<sub>2</sub>O<sub>3</sub> nanoparticles or stacking faults," *Applied Physics Letters*, vol. 106, no. 5, p. 052603, 2015.
- [59] T. Horide, K. Taguchi, K. Matsumoto, N. Matsukida, M. Ishimaru, P. Mele, and R. Kita, "Influence of matching field on critical current density and irreversibility temperature in YBa<sub>2</sub>Cu<sub>3</sub>O<sub>7</sub> films with BaMO<sub>3</sub> (M= Zr, Sn, Hf) nanorods," *Applied Physics Letters*, vol. 108, no. 8, p. 082601, 2016.
- [60] J.-W. Lee, S.-M. Choi, W.-J. Oh, J.-H. Lee, S.-H. Moon, and S.-I. Yoo, "Enhanced Pinning Properties of GdBa<sub>2</sub>Cu<sub>3</sub>O<sub>7-δ</sub> Coated Conductors via a Post-Annealing Process," *IEEE Transactions on Applied Superconductivity*, vol. 26, no. 3, pp. 1-6, 2016.
- [61] S. Miura, Y. Yoshida, Y. Ichino, Q. Xu, K. Matsumoto, A. Ichinose, and S. Awaji, "Improvement in J<sub>c</sub> performance below liquid nitrogen

- temperature for  $\text{SmBa}_2\text{Cu}_3\text{O}_y$  superconducting films with  $\text{BaHfO}_3$  nano-rods controlled by low-temperature growth," *Apl Materials*, vol. 4, no. 1, p. 016102, 2016.
- [62] L. Opherden, M. Sieger, P. Pahlke, R. Hühne, L. Schultz, A. Meledin, G. Van Tendeloo, R. Nast, B. Holzapfel, and M. Bianchetti, "Large pinning forces and matching effects in  $\text{YBa}_2\text{Cu}_3\text{O}_{7-\delta}$  thin films with  $\text{Ba}_2\text{Y}(\text{Nb}/\text{Ta})\text{O}_6$  nano-precipitates," *Scientific reports*, vol. 6, p. 21188, 2016.
- [63] W.-J. Oh, I. Park, J.-H. Lee, H. Lee, S.-H. Moon, K. Shinde, K. Chung, and S.-I. Yoo, "The Post-Annealing Effect on the Pinning Properties of  $\text{GdBa}_2\text{Cu}_3\text{O}_{7-\delta}$  Coated Conductors via RCE-DR," *IEEE Transactions on Applied Superconductivity*, vol. 28, no. 4, 2018.
- [64] S. Zhang, S. Xu, Z. Fan, P. Jiang, Z. Han, G. Yang, and Y. Chen, "Broad temperature study of RE-substitution effects on the in-field critical current behavior of REBCO superconducting tapes," *Superconductor Science and Technology*, vol. 31, no. 12, p. 125006, 2018.
- [65] G. Murase, Y. Tsuchiya, Y. Ichino, and Y. Yoshida, "Effects of  $\text{Sm}_{1+x}\text{Ba}_{2-x}\text{Cu}_3\text{O}_y$  Films with Non-Stoichiometric Composition Fabricated by Combinatorial Pulsed Laser Deposition method on the Superconducting Properties," in *Journal of Physics: Conference Series*, 2019, vol. 1293, no. 1: IOP Publishing, p. 012032.
- [66] W.-J. Oh, I. Park, K. Chung, Y. Lee, J. H. Lee, H. Lee, S.-H. Moon, and S.-I. Yoo, "Enhanced Pinning Properties of Sm-doped GdBCO CCs by the RCE-DR process," *IEEE Transactions on Applied Superconductivity*, vol. 29, p. 8002404, 2019.
- [67] A. Usoskin, J. Knoke, F. Garcia-Moreno, A. Issaev, J. Dzick, S. Sievers, and H. C. Freyhardt, "Large-area HTS-coated stainless steel tapes with high critical currents," *IEEE transactions on applied superconductivity*, vol. 11, no. 1, pp. 3385-3388, 2001.
- [68] A. Usoskin, L. Kirchhoff, J. Knoke, B. Prause, A. Rutt, V. Selskij, and

- D. Farrell, "Processing of long-length YBCO coated conductors based on stainless steel tapes," *IEEE Transactions on Applied Superconductivity*, vol. 17, no. 2, pp. 3235-3238, 2007.
- [69] T. Nagaishi, Y. Shingai, M. Konishi, T. Taneda, H. Ota, G. Honda, T. Kato, and K. Ohmatsu, "Development of REBCO coated conductors on textured metallic substrates," *Physica C: Superconductivity*, vol. 469, no. 15-20, pp. 1311-1315, 2009.
- [70] M. Igarashi, K. Kakimoto, S. Hanyu, C. Tashita, T. Hayashida, Y. Hanada, S. Fujita, K. Morita, N. Nakamura, and Y. Sutoh, "Remarkable progress in fabricating RE123 coated conductors by IBAD/PLD technique at Fujikura," in *Journal of Physics: Conference Series*, 2010, vol. 234, no. 2: IOP Publishing, p. 022016.
- [71] S. Lee, V. Petrykin, A. Molodyk, S. Samoilenkov, A. Kaul, A. Vavilov, V. Vysotsky, and S. Fetisov, "Development and production of second generation high  $T_c$  superconducting tapes at SuperOx and first tests of model cables," *Superconductor Science and Technology*, vol. 27, no. 4, p. 044022, 2014.
- [72] V. Selvamanickam, Y. Xie, J. Reeves, and Y. Chen, "MOCVD-based YBCO-coated conductors," *MRS bulletin*, vol. 29, no. 8, pp. 579-582, 2004.
- [73] Y. Xie, V. Selvamanickam, M. Marchevsky, Y. Chen, X. Xiong, A. Rar, K. Lenseth, Y. Qiao, D. Hazelton, and A. Knoll, "Second-generation HTS wire manufacturing and technology advancement at superpower," in *2009 International Conference on Applied Superconductivity and Electromagnetic Devices*, 2009: IEEE, pp. 398-402.
- [74] A. Gupta, R. Jagannathan, E. I. Cooper, E. Giess, J. Landman, and B. Hussey, "Superconducting oxide films with high transition temperature prepared from metal trifluoroacetate precursors," *Applied Physics Letters*, vol. 52, no. 24, pp. 2077-2079, 1988.
- [75] Y. Tokunaga, H. Fuji, R. Teranishi, J. Matsuda, S. Asada, A. Kaneko, T.

- Honjo, T. Izumi, Y. Shiohara, and Y. Yamada, "High critical current YBCO films using advanced TFA-MOD process," *Physica C: Superconductivity*, vol. 412, pp. 910-915, 2004.
- [76] Y. Xu, A. Goyal, K. Leonard, L. Heatherly, and P. Martin, "Liquid phase enhanced hybrid MOD approach for high performance YBCO films development," *IEEE transactions on applied superconductivity*, vol. 15, no. 2, pp. 2617-2619, 2005.
- [77] K. Tsukada, I. Yamaguchi, M. Sohma, W. Kondo, K. Kamiya, T. Kumagai, and T. Manabe, "Preparation of epitaxial  $\text{YBa}_2\text{Cu}_3\text{O}_{7-y}$  films on  $\text{CeO}_2$ -buffered yttria-stabilized zirconia substrates by fluorine-free metalorganic deposition," *Physica C: Superconductivity*, vol. 458, no. 1-2, pp. 29-33, 2007.
- [78] M. W. Rupich, X. Li, S. Sathyamurthy, C. L. Thieme, K. DeMoranville, J. Gannon, and S. Fleshler, "Second generation wire development at AMSC," *IEEE transactions on applied superconductivity*, vol. 23, no. 3, pp. 6601205-6601205, 2012.
- [79] J.-H. Lee, H. Lee, J.-W. Lee, S.-M. Choi, S.-I. Yoo, and S.-H. Moon, "RCE-DR, a novel process for coated conductor fabrication with high performance," *Superconductor Science and Technology*, vol. 27, no. 4, p. 044018, 2014.
- [80] C. Senatore, C. Barth, M. Bonura, M. Kulich, and G. Mondonico, "Field and temperature scaling of the critical current density in commercial REBCO coated conductors," *Superconductor Science and Technology*, vol. 29, no. 1, p. 014002, 2015.

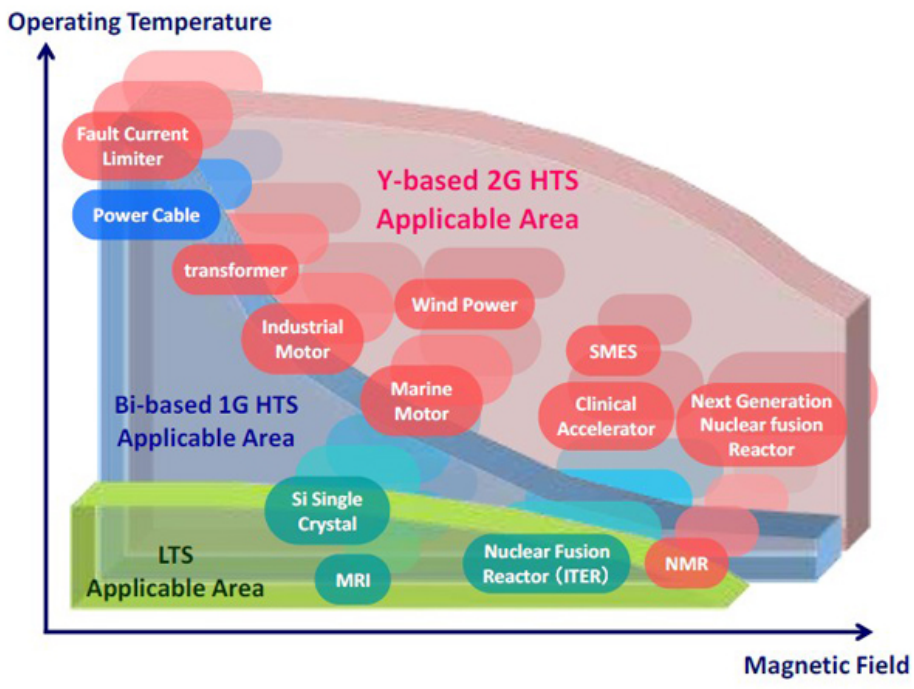


Fig. 1.1. Electric applications of LTS, 1G HTS, and 2G HTS as a function of magnetic field [4].

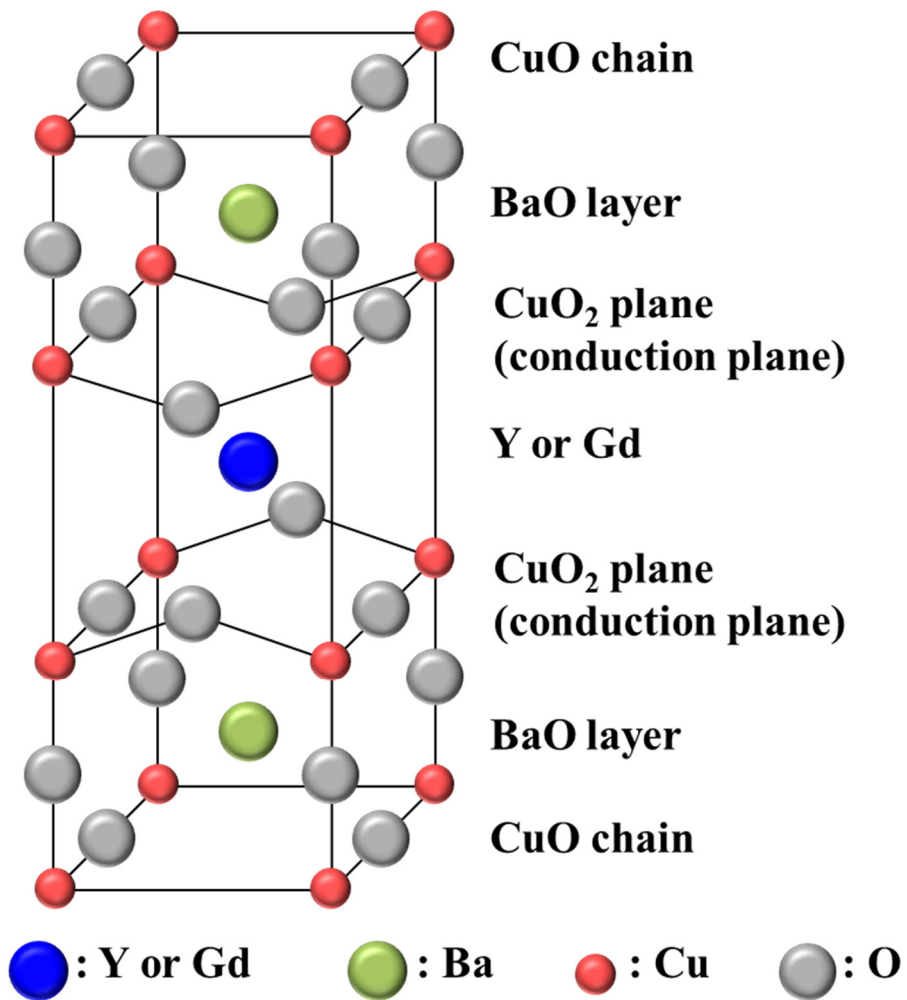


Fig. 1.2. Crystallographic structure of YBCO and REBCO.

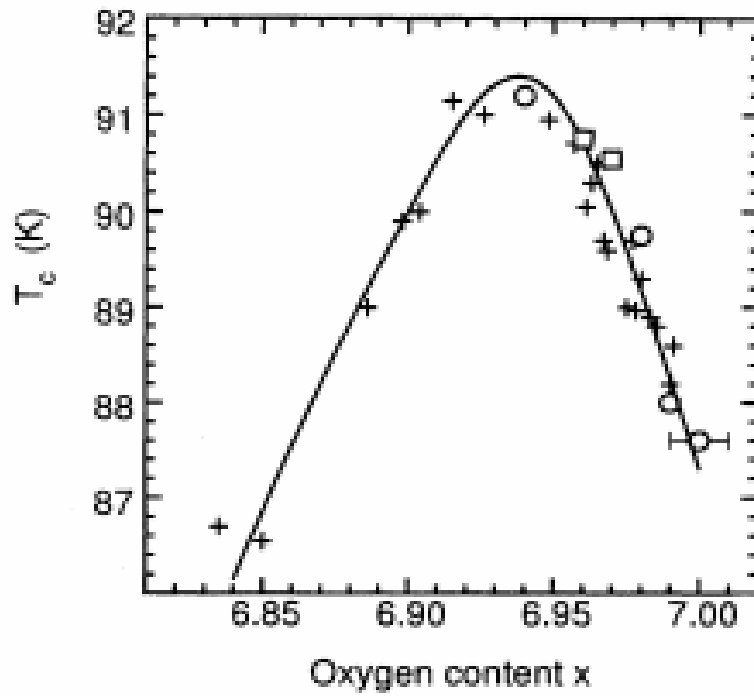


Fig. 1.3.  $T_c$  values of YBCO compound versus the oxygen content  $x$  ( $\text{YBa}_2\text{Cu}_3\text{O}_{7-x}$ ) [5].

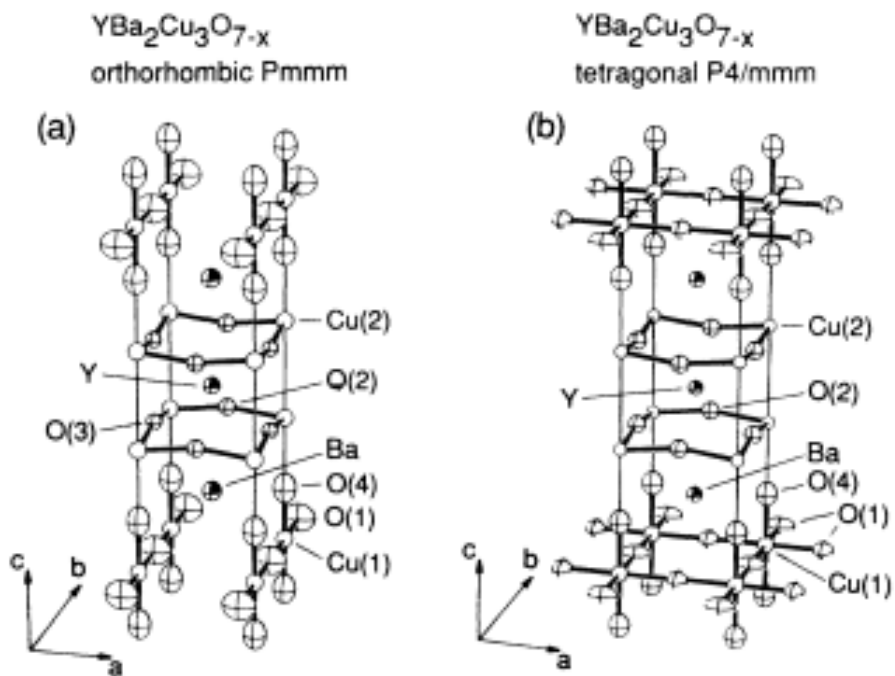


Fig. 1.4. (a) Orthorhombic and (b) tetragonal structures of YBCO compound [7].

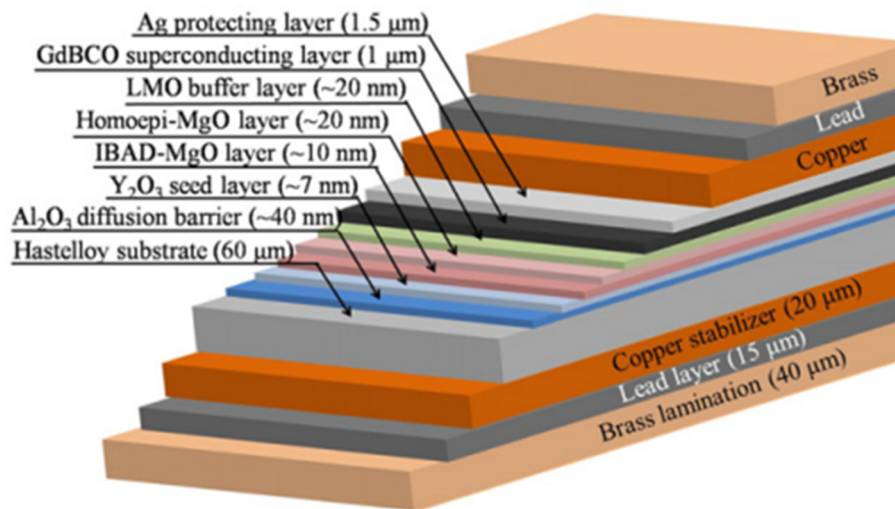


Fig. 1.5. A schematic of the architecture for REBCO CCs [10].

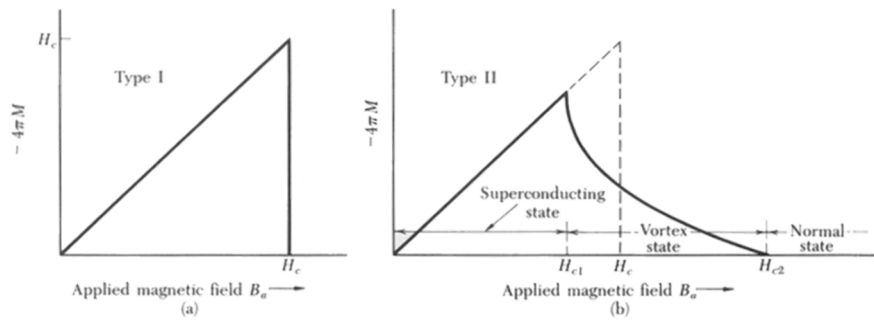


Fig. 1.6. Field dependence of magnetization for (a) type-I superconductor and (b) type-II superconductor.

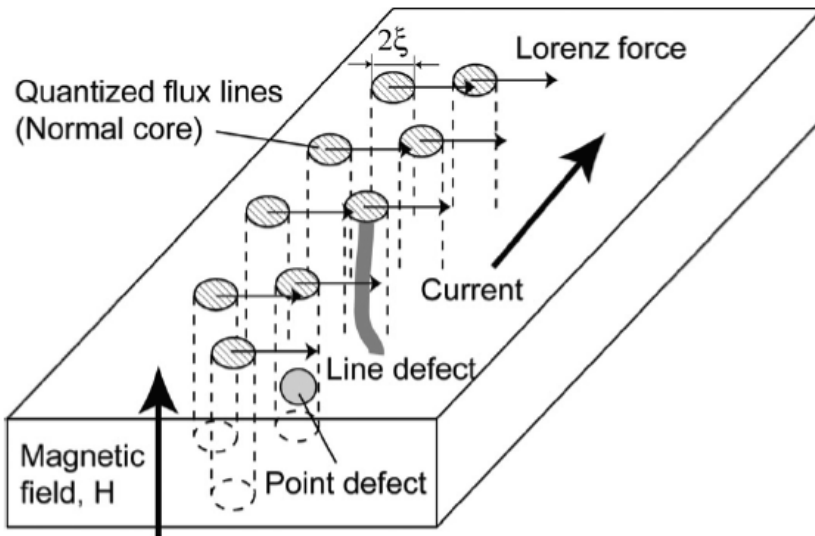


Fig. 1.7. Schematics of quantized flux lines and flux pinning [12].

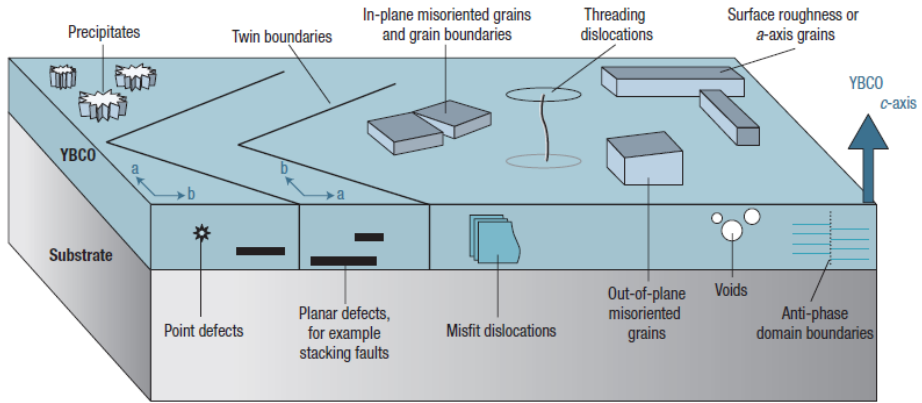


Fig. 1.8. Naturally generated defects in the REBCO films [29].

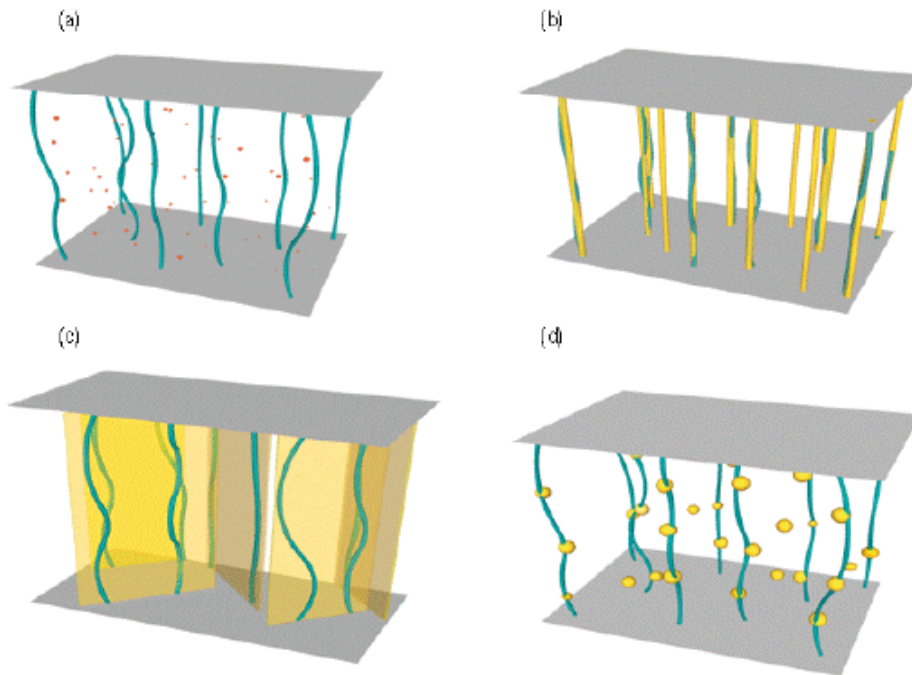


Fig. 1.9. Schematic of the dimensionality of artificial pinning centers (APCs): (a) 0D-APC, (b) 1D-APC, (c) 2D-APC, and (d) 3D-APC [30].

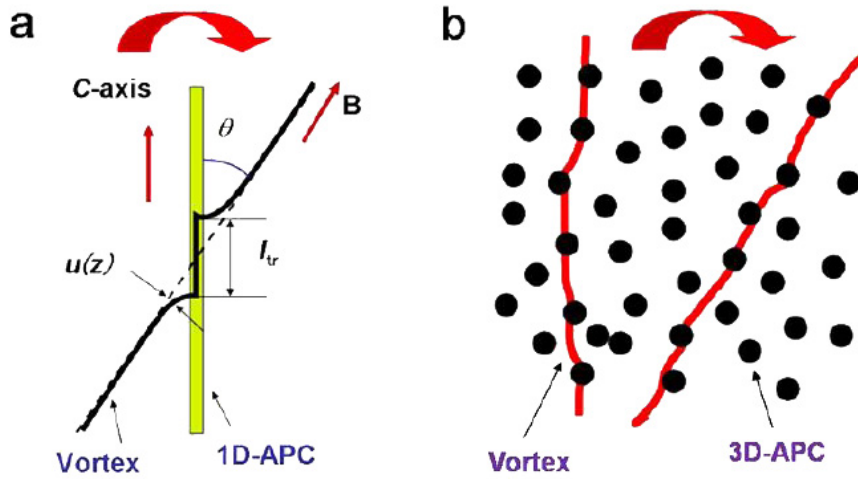


Fig. 1.10. Comparison of the configuration of a pinned vortex by 1D-APCs or 3D-APCs: (a) the zigzag state of the flux line when the magnetic field is applied tilted from the direction of 1D-APCs, (b) the flux line which is pinned by the randomly distributed 3D-APCs in the tilted magnetic field [41].

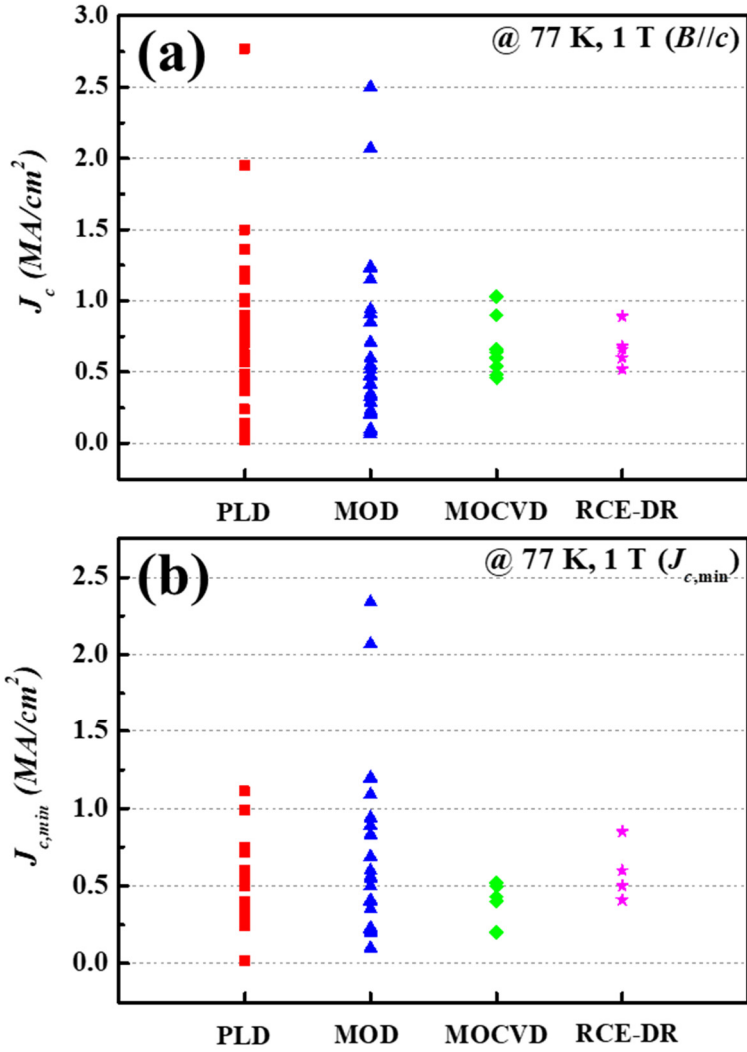


Fig. 1.11. Summarization of the  $J_{c,min}$  and  $J_c$  for  $B//c$  values as function of fabrication technologies.

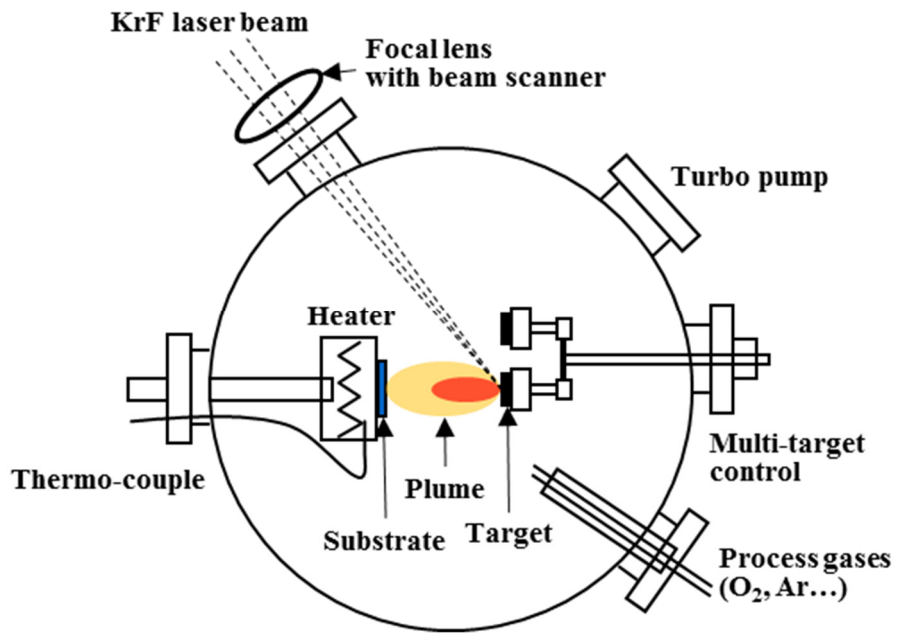


Fig. 1.12. A schematic of PLD system.

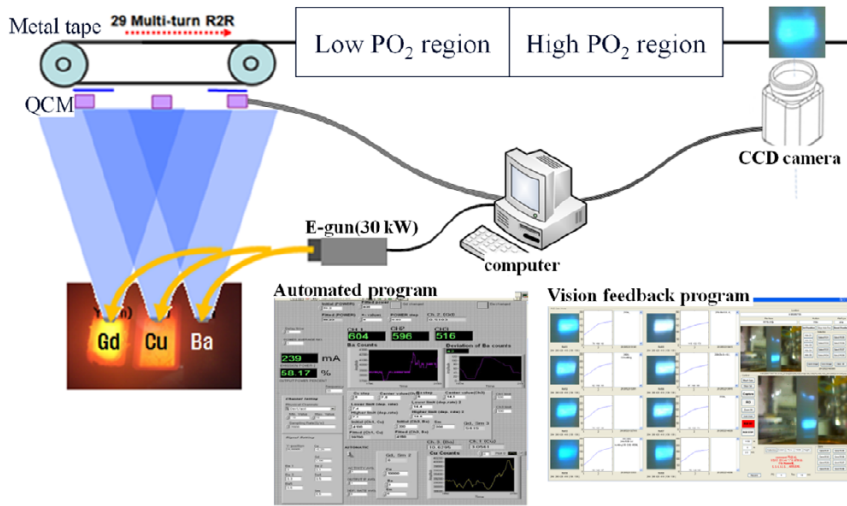


Fig. 1.13. A schematic of the RCE-DR process and the program of the automated deposition control [79].

# **Chapter 2. Improvement of pinning properties of RE<sub>2</sub>O<sub>3</sub>-doped REBCO (RE = Eu, Gd) films by the PLD process**

## **2.1. Introduction**

Practical applications for HTS power devices require enhanced  $J_c$  values in magnetic fields, and thus many groups [1-13] have tried to improve the pinning properties of GdBCO films by introducing nano-sized second phases into the superconducting matrix. Various second phases introduced into the GdBCO films by PLD include yttria-stabilized zirconium (YSZ) [1, 2], Au [4], BaZrO<sub>3</sub> (BZO) [3, 5-8], BaSnO<sub>3</sub> (BSO) [11-13], and BaHfO<sub>3</sub> (BHO) [9, 10]. These dopants commonly exist as columnar defects (or nanorods), known as 1D-APCs, in the GdBCO matrix, and act as  $c$ -axis correlated pinning centers.

Unlike 1D-APCs, Mele *et al.* [14] have reported inclusions of Y<sub>2</sub>O<sub>3</sub> nanoparticles in the YBCO matrix, known as 3D-APCs, for Y<sub>2</sub>O<sub>3</sub>-doped YBCO films by PLD using the ‘surface-modified target’ method. Matsumoto *et al.* [15] have reported that the pinning properties of 3D-APCs, such as nanoparticles, can surpass those of 1D-APCs in all field directions. Also, the combination of nanorods and nanoparticles can improve pinning properties in various magnetic fields [16, 17]. T. Horide *et al.* [16] reported the  $J_c$  improvement by double artificial pinning center of BaSnO<sub>3</sub> nanorods and Y<sub>2</sub>O<sub>3</sub> nanoparticles in YBCO CCs. The YBCO + BSO + Y<sub>2</sub>O<sub>3</sub> films represented very isotropic  $J_c$  at 77 K and

1 T compared with pure YBCO and YBCO + BSO films.

In this chapter, we investigated effect of the  $\text{RE}_2\text{O}_3$  nanoparticles on the pinning properties of REBCO films (RE: Gd, Eu). Compared with the  $\text{Y}_2\text{O}_3$ -doped YBCO films [14], the in-field  $J_c$  values of the  $\text{RE}_2\text{O}_3$ -doped REBCO films were lower than those of the undoped REBCO films above 65 K. The main reason was that the  $\text{RE}_2\text{O}_3$  dopants caused significant  $T_{c,zero}$  drop for the  $\text{RE}_2\text{O}_3$ -doped REBCO films. Therefore, we tried to identify the origin of severe  $T_{c,zero}$  drop and investigated the effect of  $\text{RE}_2\text{O}_3$  nanoparticles on the pinning properties of REBCO films fabricated by PLD process.

## 2.2. Experimental

To obtain highly textured REBCO films on the  $\text{CeO}_2$ -buffered MgO (100) substrate, we first deposited biaxially textured  $\text{CeO}_2$  buffer layer of  $\sim 100$  nm thickness on MgO (100) single crystal substrate via RF-magnetron sputtering with the oxygen pressure ( $P_{\text{O}_2}$ ) of 10 mTorr, RF power of 150 W, the deposition temperature of  $600^\circ\text{C}$ , and the deposition time of 20 min. Next, for the fabrication of  $\text{Gd}_2\text{O}_3$ -doped GdBCO films and  $\text{Eu}_2\text{O}_3$ -doped EuBCO films, a disk-shaped  $\text{Gd}_2\text{O}_3$  and  $\text{Eu}_2\text{O}_3$  target were cut into a pie sector and attached on top of the GdBCO and EuBCO target. We varied the amounts of  $\text{Gd}_2\text{O}_3$  and  $\text{Eu}_2\text{O}_3$  inclusion within the GdBCO and EuBCO matrix by controlling the area of  $\text{Gd}_2\text{O}_3$  and  $\text{Eu}_2\text{O}_3$  sectors. The REBCO and  $\text{RE}_2\text{O}_3$  targets were sintered by the solid-state reaction employing precursors of  $\text{RE}_2\text{O}_3$  (High Purity Co., 99.9%),  $\text{BaCO}_3$  (High Purity Co., 99.9%), and  $\text{CuO}$  (High Purity Co., 99.9%). For the preparation of REBCO target, calcination at  $880^\circ\text{C}$  for 12 h in air was

repeated three times with an intermediate ball milling for 12 h, as-calcined powder was uniaxially pressed into a pellet, and the pellet was further pressed using a Cold Isostatic Press(CIP). Finally, the pellet of 1 inch diameter was sintered at 930°C for 12 h in 1% O<sub>2</sub>/ 99% Ar gas atmosphere. A Lambda Physik KrF excimer laser ( $\lambda= 248$  nm) with the energy density of 1.5 J/cm<sup>2</sup> and the laser frequency of 8 Hz was used to deposit GdBCO films at 800°C in the PO<sub>2</sub> of 300 mTorr and EuBCO films at 800°C in the PO<sub>2</sub> of 400 mTorr. The distance between target and substrate was 4.0 cm. As-deposited samples were annealed at 500°C for 1 h in a pure oxygen atmosphere.

The crystal phases and orientations of REBCO films were analyzed with an X-ray diffractometer (Bruker D8-Advance, Cu  $K\alpha$  radiation). The in-plane texture ( $\Delta\phi$ ) and out-of-texture ( $\Delta\omega$ ) of GdBCO films were analyzed by X-ray  $\phi$ -scan and  $\omega$ -scan (PANalytical X'pert Pro) using REBCO (103) and REBCO (005) reflections, respectively. Field emission-scanning electron microscopy (FE-SEM, MERLIN Compact), transmission electron microscopy (TEM, JEOL JEM-2100F) and scanning transmission electron microscopy (STEM, JEOL ARM200F) were employed to characterize the microstructures of samples. The TEM specimens were prepared by Focused Ion Beam (FIB) (SII Nanotechnology, SMI3050SE). Magnetic  $J_c$  values were evaluated from the magnetic hysteresis curves measured up to 5 T by Quantum Design SQUID magnetometer (MPMS 3 and MPMS-XL) for the field parallel to the  $c$ -axis of REBCO films ( $B//c$ ). The magnetic  $J_c$  values of samples were evaluated using the equation of  $J_c = 20\Delta M/[a(1 - (a/3b))]$  from a modified Bean's critical state model [18], where  $a$  and  $b$  are width and length of the rectangular film measured in centimeter ( $b > a$ ), respectively, and  $\Delta M$  is the magnetization hysteresis loop

width measured in  $\text{emu}/\text{cm}^3$ . The angular dependence of transport  $J_c$  values of REBCO films was measured using the PPMS (Quantum Design, model-6000) after patterning a micro-bridge. A standard four-point probe method was used to measure temperature dependence of electrical resistivity ( $\rho$ - $T$  curve) and current-voltage ( $I$ - $V$ ) curve. The transport critical currents were measured with the criterion of  $1 \mu\text{Vcm}^{-1}$ .

## 2.3. Results and discussion

### 2.3.1. GdBCO films with $\text{Gd}_2\text{O}_3$ nanoparticles

Fig. 2.1 shows the XRD patterns of undoped and  $\text{Gd}_2\text{O}_3$ -doped GdBCO films deposited on  $\text{CeO}_2$ -buffered MgO (100) substrates. From Fig. 2.1, we can see that all GdBCO films are strongly  $c$ -axis oriented. A small peak  $\text{Gd}_2\text{O}_3$  (222) reflection is observable only for 10 mol%  $\text{Gd}_2\text{O}_3$ -doped GdBCO film while it is undetectable for other  $\text{Gd}_2\text{O}_3$ -doped GdBCO samples most probably due to their relatively smaller amounts.

The in-plane ( $\Delta\phi$ ) and out-of-plane textures ( $\Delta\omega$ ) of all GdBCO films are shown in Fig. 2.2. For the analysis of textures,  $\phi$ -scan and  $\omega$ -scan were performed for (103) and (005) reflections, respectively. It is obvious that both in-plane and out-of-plane textures of GdBCO films are gradually deteriorated with increasing the  $\text{Gd}_2\text{O}_3$  content. As shown in Fig. 2.2, both in-plane and out-of-plane textures of GdBCO films exhibit a linear deterioration with increasing up to 5 mol%  $\text{Gd}_2\text{O}_3$  contents. With further increasing the  $\text{Gd}_2\text{O}_3$  content up to 10 mol%, while the linear deterioration of in-plane textures of GdBCO films

become even worse, the out-of-plane textures of GdBCO films become less deteriorated. The lattice mismatch between the GdBCO matrix and trapped  $\text{Gd}_2\text{O}_3$  particles causes a lattice strain that may be responsible for the gradual degradation with increasing the  $\text{Gd}_2\text{O}_3$  content. A similar behavior of in-plane texture with increasing the BSO content was reported on BSO-doped GdBCO films by our group [13]. Compared with undoped SmBCO film, the deterioration of in-plane texture was also reported for 2 vol% BZO-doped SmBCO film [19]. A gradual degradation in the out-of-plane textures with increasing the BSO content has been reported for BSO-doped YBCO films [20].

The  $\rho$ - $T$  curves of all samples are represented in Fig. 2.3(a). As shown in Fig. 2.3(a), the  $\rho$ - $T$  curves at the normal state have a linear metallic behavior, and their  $\rho$  values of GdBCO films are increased with increasing the  $\text{Gd}_2\text{O}_3$  content, which is in accordance with our expectation. As previously reported by many authors [20-23], a gradual increase in the GdBCO lattice strain is considered to be responsible for the degradation in  $T_c$  values with increasing the  $\text{Gd}_2\text{O}_3$  content. The  $T_{c,zero}$  and  $\Delta T$  are plotted in Fig. 2.3(b) as a function of the  $\text{Gd}_2\text{O}_3$  content in the GdBCO matrix. Fig. 2.3(a) shows that the  $T_{c,zero}$  values are gradually decreased, and  $\Delta T$  values are slightly increased with increasing the  $\text{Gd}_2\text{O}_3$  content.

The magnetic field dependency of  $J_c$  at 20, 40, 65 and 77 K for  $B//c$  is shown for all GdBCO samples in Fig. 2.4. The magnetic  $J_c$  values at 20, 40, 65 and 77 K in self-field are slightly decreased with increasing  $\text{Gd}_2\text{O}_3$  content. In the magnetic fields ranging from 0.2 to 5 T at 20 K,  $J_c$  values of 5 mol%  $\text{Gd}_2\text{O}_3$ -doped GdBCO film are superior to those of other samples. At 40 K, the improved magnetic  $J_c$  values can be observed up to 3 T for the same sample

although they become lower than those of undoped GdBCO above 3 T. The exponent  $\alpha$  value, calculated by a linear regression of the  $J_c - H^\alpha$  curve, of undoped GdBCO film was  $\sim 0.58$  at 20 and 40 K while 5 mol% Gd<sub>2</sub>O<sub>3</sub>-doped GdBCO film exhibited slightly smaller  $\alpha$  value of  $\sim 0.47$ . On the other hand, the exponent  $\alpha$  value of undoped GdBCO film exhibited smaller value of  $\sim 0.90$  than that of  $\sim 1.23$  for 5 mol% Gd<sub>2</sub>O<sub>3</sub>-doped GdBCO film at 65 K. The exponent  $\alpha$  value could not be evaluated at 77 K because all Gd<sub>2</sub>O<sub>3</sub>-doped GdBCO films show a nonlinear behavior in the power-law region.

The pinning force density,  $F_p (= J_c \times B)$  at 20, 40, 65 and 77 K as a function of the magnetic field for  $B//c$  is shown in Fig. 2.5. The 5 mol% Gd<sub>2</sub>O<sub>3</sub>-doped GdBCO film shows the  $F_{p,max}$  of 119 GN/m<sup>3</sup> near 3.8 T at 20 K, and 40 GN/m<sup>3</sup> near 2.2 T at 40 K, which are higher than those of undoped GdBCO film. While the largest  $F_{p,max}$  value is achieved from the 5 mol% Gd<sub>2</sub>O<sub>3</sub>-doped GdBCO film, implying that the optimum doping content of Gd<sub>2</sub>O<sub>3</sub> is 5 mol% below 40 K, all Gd<sub>2</sub>O<sub>3</sub> doped-GdBCO films show a degradation in the pinning properties above 65 K, implying that Gd<sub>2</sub>O<sub>3</sub>-doped GdBCO films are effective in lower temperature region. However, this tendency differs from that of Y<sub>2</sub>O<sub>3</sub>-doped YBCO films which show enhanced magnetic  $J_c$  values at 65 K. This difference might be partially attributable to relatively higher  $T_{c,zero}$  drop in 2.2 vol% Gd<sub>2</sub>O<sub>3</sub>-doped GdBCO films ( $\sim 2.4$  K) compared with 2.5 vol% Y<sub>2</sub>O<sub>3</sub>-doped YBCO films ( $\sim 1.3$  K) [14]. Interestingly, we could find two peaks in  $F_p$  versus  $B$  plot at 77 K, which has never been reported yet. The large  $F_p$  peaks of all GdBCO films below 1 T might be related to random pinning center due to Gd<sub>2</sub>O<sub>3</sub> nanoparticles. The other small  $F_p$  peaks above 2 T are attributable to  $c$ -axis correlated pinning center since GdBCO films with columnar defects or

nanorods commonly exhibit these peaks [9, 13, 20, 21]. Since our samples do not include nanorods, the origin for these peaks is unclear at the moment and thus requires further study.

Fig. 2.6 shows field orientation dependence of  $J_c$  for undoped, 2 mol%, and 5 mol%  $\text{Gd}_2\text{O}_3$ -doped GdBCO films. All three films show a very sharp  $J_c$  peak at  $\theta = 90^\circ$  ( $B//ab$ ) due to intrinsic pinning as previously reported for YBCO films [24, 25]. However, the  $J_c$  peak near  $\theta = 180^\circ$  ( $B//c$ ) was unobservable for  $\text{Gd}_2\text{O}_3$ -doped GdBCO films, indicating 3D-APCs are randomly distributed in the GdBCO matrix [14]. In accordance with the behavior of magnetic  $J_c$  at 77K, there is no enhancement of transport  $J_c$  for  $B//c$  at 77K in 1 T with the  $\text{Gd}_2\text{O}_3$  dopant. Unfortunately, although we tried to measure the angular dependence of transport  $J_c$  at 20 K in 7 T, we failed to measure it because the electrode contact for current flow was burnt out. If we could measure the transport  $J_c$  values at 20 K, 5 mol%  $\text{Gd}_2\text{O}_3$ -doped GdBCO film might reveal improved pinning properties along the field direction parallel to the  $c$ -axis.

In order to investigate the origin of improved pinning properties, cross-sectional TEM analysis was performed for 5mol%  $\text{Gd}_2\text{O}_3$ -doped GdBCO film. As shown in Fig. 2.7, the round-shaped  $\text{Gd}_2\text{O}_3$  nanoparticles with an average diameter of 18 nm are randomly dispersed in the GdBCO matrix, which is much larger than  $\text{Y}_2\text{O}_3$  nanoparticles of  $\sim 8$  nm in diameter for  $\text{Y}_2\text{O}_3$ -doped YBCO film [14]. Also, the crystallographic orientation of the  $\text{Gd}_2\text{O}_3$  nanoparticles are represented in Fig. 2.8. For the same volume fraction of nanoparticles, the  $\text{Gd}_2\text{O}_3$  nanoparticles would produce much less lattice strain compared with  $\text{Y}_2\text{O}_3$  nanoparticles because of much larger particle size, resulting in less effective pinning. Thus, the peculiar pinning behavior of 2.2 vol%  $\text{Gd}_2\text{O}_3$ -

doped GdBCO films in comparison with 2.5 vol% Y<sub>2</sub>O<sub>3</sub>-doped YBCO film [14] might also be related to larger particle size of Gd<sub>2</sub>O<sub>3</sub> in addition to higher  $T_{c,zero}$  drop.

### 2.3.2. EuBCO films with Eu<sub>2</sub>O<sub>3</sub> nanoparticles

As shown in Fig. 2.9, both the pristine and Eu<sub>2</sub>O<sub>3</sub>-doped EuBCO films show *c*-axis oriented epitaxial growth. In addition to (00*l*) peaks of EuBCO films, we can observe the CeO<sub>2</sub> and MgO substrates peaks while the Eu<sub>2</sub>O<sub>3</sub> peak is unobservable in the XRD patterns. In previous reports [16, 26], the Y<sub>2</sub>O<sub>3</sub> and Gd<sub>2</sub>O<sub>3</sub> peaks were also unobservable in the Y<sub>2</sub>O<sub>3</sub>-doped YBCO and Gd<sub>2</sub>O<sub>3</sub>-doped GdBCO films by PLD using the modified surface target. Fig.2.10 shows that both the in plane ( $\Delta\phi$ ) and out-of-plane ( $\Delta\omega$ ) textures of EuBCO films are gradually deteriorated with increasing Eu<sub>2</sub>O<sub>3</sub> doping contents. Especially, the in plane ( $\Delta\phi$ ) textures of Eu<sub>2</sub>O<sub>3</sub>-doped EuBCO films become even worse above 5 mol% Eu<sub>2</sub>O<sub>3</sub> doping contents. The degradation of textures was responsible for the strain effect induced by the lattice mismatch between the superconducting matrix and second phases [13, 14, 20, 22, 23, 26, 27].

The  $\rho$ -*T* curves are represented in Fig. 2.11(a). The  $\rho - T$  curves of all samples have a linear metallic behavior. The  $T_{c,zero}$  values of Eu<sub>2</sub>O<sub>3</sub>-doped EuBCO films were degraded with increasing the Eu<sub>2</sub>O<sub>3</sub> doping contents compared with the pristine sample. Also, the normal state resistivity and transition widths ( $\Delta T$ ) values of the Eu<sub>2</sub>O<sub>3</sub>-doped EuBCO films increased with further increasing the Eu<sub>2</sub>O<sub>3</sub> doping content. In the previous studies [13, 14, 20, 22, 23, 26, 27], the degradation of the  $T_{c,zero}$  values might be responsible for the

strain effect with increasing doping contents due to the lattice mismatch between the superconducting matrix and dopants. In addition to the strain effect, the formation of a solid solution could affect the  $T_{c,zero}$  values in the  $\text{Eu}_2\text{O}_3$ -doped EuBCO films since the Eu elements were abundant during the deposition. The effect of the solid solution on the  $T_{c,zero}$  drop will be discussed later.

The field dependency of magnetic  $J_c$  values at 20, 40, 65 and 77 K for  $B//c$  is shown in the Fig. 2.12. The  $J_c$  values of the pristine sample in self-field were higher than those of  $\text{Eu}_2\text{O}_3$ -doped EuBCO films at 20, 40, 65 and 77 K, respectively. However, the  $J_c$  values of  $\text{Eu}_2\text{O}_3$ -doped EuBCO films were higher than those of the pristine sample at 20 K in magnetic fields up to 5 T except the 8 mol%  $\text{Eu}_2\text{O}_3$ -doped EuBCO film, indicating that the  $\text{Eu}_2\text{O}_3$  nanoparticles were effective for improving pinning properties at relatively low temperatures. Especially, the 4 mol%  $\text{Eu}_2\text{O}_3$ -doped EuBCO sample exhibits the highest  $J_c$  value compared with other samples in magnetic fields ranging from 0.2 to 5 T at 20 and 40 K in Fig. 2.12(a) and (b). The exponent  $\alpha$  value, calculated by a linear regression of the  $J_c - H^\alpha$  curve, of 4 mol%  $\text{Eu}_2\text{O}_3$ -doped EuBCO film was  $\sim 0.21$  at 20 K while that of pristine sample represented higher value of  $\sim 0.49$ . Above 65 K, we can observe that the  $J_c$  values of  $\text{Eu}_2\text{O}_3$ -doped EuBCO samples were lower than those of the pristine sample. This particular results were observable in the  $\text{Gd}_2\text{O}_3$ -doped GdBCO films [26]. The main reason of the in-field  $J_c$  degradation at high temperatures was that the  $T_{c,zero}$  values of  $\text{RE}_2\text{O}_3$ -doped REBCO films were significantly degraded with increasing the  $\text{RE}_2\text{O}_3$  doping contents.

The  $F_p$  values, calculated by the relationship of  $F_p = J_c \times B$ , are represented as function of the magnetic field at 20, 40, 65 and 77 K for  $B//c$  in Fig. 2.13. As

shown in Fig. 2.13(a) and Fig. 2.13(b), the pinning force densities of 4 mol%  $\text{Eu}_2\text{O}_3$ -doped EuBCO film show the  $F_{p,max}$  of  $125 \text{ GN/m}^3$  near 4 T at 20 K and  $55 \text{ GN/m}^3$  near 3 T at 40. Compared with other  $\text{Eu}_2\text{O}_3$ -doped EuBCO films, the 4 mol%  $\text{Eu}_2\text{O}_3$ -doped EuBCO film exhibited highest  $F_{p,max}$ , indicating that the 4 mol% was the optimum doping content below 40 K. On the other hand, the pinning force densities of the pristine sample were higher than those of  $\text{Eu}_2\text{O}_3$ -doped EuBCO films above 65 K except 4 mol%  $\text{Eu}_2\text{O}_3$ -doped EuBCO film, which showed still higher maximum pinning force density than the pristine sample up to 65 K. Actually, the optimum  $\text{Y}_2\text{O}_3$  doping content of 5.44 A% [27] was higher than the optimum  $\text{Eu}_2\text{O}_3$  doping content of 1.94 A% (4 mol%). Since the EuBCO films were seriously affected by the  $T_{c,zero}$  drop, it was difficult to increase the amounts of dopants. If the  $T_{c,zero}$  drop become less with further increasing  $\text{Eu}_2\text{O}_3$  doping content, it is believed that the pinning properties of  $\text{Eu}_2\text{O}_3$ -doped EuBCO films at high temperatures could be improved significantly as much as those of the  $\text{Y}_2\text{O}_3$ -doped YBCO films [27].

The angular dependency of transport  $J_c$  for both the pristine and 4 mol%  $\text{Eu}_2\text{O}_3$ -doped EuBCO film is represented in Fig. 2.14. As shown in Fig. 2.14, the pristine sample has a sharp  $J_c$  peak at  $\theta = 90^\circ$  ( $B//ab$ ), which is responsible for the extended planar defects and intrinsic pinning due to layered structure [25]. The transport  $J_c$  values of 4 mol%  $\text{Eu}_2\text{O}_3$ -doped EuBCO film were lower than those of the pristine sample in the whole angular region at 77 K, which was correspond to magnetic  $J_c$  values for  $B//c$  at 77 K. Unfortunately, we failed to measure the angular dependency of transport  $J_c$  below 40 K due to the current limit of measurement system. Interestingly,  $J_c$  peak near  $\theta = 180^\circ$  ( $B//c$ ) was unobservable for the undoped and  $\text{Gd}_2\text{O}_3$ -doped GdBCO film in our previous

report [26] while the undoped and  $\text{Eu}_2\text{O}_3$ -doped EuBCO films have a broad  $J_c$  peak near  $\theta = 180^\circ$  ( $B//c$ ). This different results on the angular dependence of  $J_c$  between the GdBCO and EuBCO films might be responsible for the different PLD processing conditions. There were many reports on the origin of  $J_c$  peak along the  $c$ -axis direction, including the twin boundaries [28-30], SFs [1, 31-33], and dislocations [34-38]. In chapter. 3, we will discuss the effect of PLD processing conditions on the  $J_c$  peak for  $B//c$ .

To investigate microstructures of  $\text{Eu}_2\text{O}_3$ -doped EuBCO films, the cross-sectional TEM analysis was performed for the 4 mol%  $\text{Eu}_2\text{O}_3$ -doped EuBCO film. Fig. 2.15 shows the cross-sectional TEM images of the 4 mol%  $\text{Eu}_2\text{O}_3$ -doped EuBCO film. The round-shaped  $\text{Eu}_2\text{O}_3$  nanoparticles with an average diameter of 18 nm were randomly dispersed in the EuBCO matrix. In comparison with the size of  $\text{Y}_2\text{O}_3$  nanoparticle [14], the size of  $\text{Eu}_2\text{O}_3$  nanoparticles was much larger than that of  $\text{Y}_2\text{O}_3$  nanoparticles with a diameter of  $\sim 8\text{nm}$ . However, the size of  $\text{Eu}_2\text{O}_3$  nanoparticles is similar to that of  $\text{Gd}_2\text{O}_3$  nanoparticles [26]. The in-field  $J_c$  improvement of the  $\text{RE}_2\text{O}_3$ -doped REBCO films at low temperatures was less than that of  $\text{Y}_2\text{O}_3$ -doped YBCO films due to the size variation between the  $\text{RE}_2\text{O}_3$  and  $\text{Y}_2\text{O}_3$  nanoparticles in addition to the  $T_{c,zero}$  drop. From the selected area FFT patterns represented in Fig. 2.15(b), we identified these particles as the  $\text{Eu}_2\text{O}_3$  nanoparticles.

In order to identify the origin of the significant  $T_{c,zero}$  drop in the  $\text{RE}_2\text{O}_3$ -doped REBCO films, we plotted the normalized  $T_{c,zero}$  values as a function of doping contents for  $\text{Y}_2\text{O}_3$ -doped YBCO and  $\text{RE}_2\text{O}_3$ -doped REBCO films in Fig. 2.16. As shown in Fig. 2.16, the significant  $T_{c,zero}$  drop of the  $\text{RE}_2\text{O}_3$ -doped REBCO films is observable in this study and our previous paper [26] compared

with the  $\text{Y}_2\text{O}_3$ -doped YBCO films [27]. As we mentioned, the  $\text{RE}_{1+x}\text{Ba}_{2-x}\text{Cu}_3\text{O}_{7-\delta}$ -type solid solution could be formed by doping the  $\text{RE}_2\text{O}_3$  contents, indicating that excess RE elements were substituted for Ba site in the matrix. According to previous reports [39, 40], the  $T_c$  values in the  $\text{RE}_{1+x}\text{Ba}_{2-x}\text{Cu}_3\text{O}_{7-\delta}$  systems were depressed with increasing  $x$  values. The solid solution could induce the oxygen disorder on the Cu-O chains, resulting in the depression of the  $T_c$  value [41]. To clarify the formation of the solid solution for the Eu and Ba substitutions, we employed the TEM-EDS point analysis to calculate the Eu/Ba ratio. As shown in Fig. 2.17, the Eu/Ba ratio increases with increasing  $\text{Eu}_2\text{O}_3$  doping contents, indicating that the  $\text{Eu}_{1+x}\text{Ba}_{2-x}\text{Cu}_3\text{O}_{7-\delta}$ -type solid solutions with higher  $x$  value can be formed due to the introduction of excess Eu elements during the deposition. Compared with  $\text{Y}_2\text{O}_3$ -doped YBCO films [27], therefore, more degraded  $T_{c,zero}$  values in  $\text{Eu}_2\text{O}_3$ -doped EuBCO films might be responsible for the formation of solid solutions, leading to the significant degradation of pinning properties at relatively high temperatures. Also, we can observe that the  $c$  lattice parameter of  $\text{Eu}_2\text{O}_3$ -doped REBCO films is reduced compared with the pristine sample in Fig. 2.17 except the 8 mol%  $\text{Eu}_2\text{O}_3$ -doped EuBCO film. It is well-known that the  $c$  lattice parameter of REBCO compound decreases with increasing RE/Ba substitution [39, 42]. While the  $c$  lattice parameter of 2 mol%  $\text{Eu}_2\text{O}_3$ -doped EuBCO decreased, that of the  $\text{Eu}_2\text{O}_3$ -doped EuBCO films increases with further increasing  $\text{Eu}_2\text{O}_3$  doping contents due to the strain effect [43-45]. The strain effect induced by lattice mismatch between the EuBCO matrix and  $\text{Eu}_2\text{O}_3$  nanoparticles could cause the elongation of  $c$  lattice parameter. Even though the  $c$  lattice parameter of  $\text{Eu}_2\text{O}_3$ -doped EuBCO films was reduced by the solid solution, the strain effect on the  $c$  lattice parameter

was dominant with further increasing  $\text{Eu}_2\text{O}_3$  doping contents.

In addition to the solid solution, the another origin of  $T_{c,zero}$  drop was the strain effect. M. Miura *et al* [46] reported that coherent interfaces between the superconducting matrix and dopants in PLD strongly influenced the  $T_c$  and self-field  $J_c$  since the strain region with coherent interfaces at the boundary between the superconducting matrix and dopants was more extended than that with incoherent interfaces. The strain region near the interfaces between the superconducting matrix and pinning centers caused  $T_c$  drop due to the formation of strain-induced oxygen vacancies [47]. According to the strain mappings, obtained from the geometric phase analysis (GPA), we can also observe that tensile and compressive strain are extended near the  $\text{Eu}_2\text{O}_3$  nanoparticle in Fig. 2.18. The strain regions which were formed at the interfaces affected the lattice structure of EuBCO matrix. Consequently, the significant  $T_c$  drop of the  $\text{Eu}_2\text{O}_3$ -doped EuBCO films by PLD was responsible for the formation of the solid solution by doping excess Eu elements and strain effect induced by coherent interfaces.

## 2.4. Summary

We tried to identify the effect of the  $\text{Gd}_2\text{O}_3$  and  $\text{Eu}_2\text{O}_3$  dopant on the pinning properties of PLD-processed GdBCO and EuBCO films on  $\text{CeO}_2$ -buffered MgO (100) substrate in order to optimize its content. First, the  $T_{c,zero}$  values of GdBCO films are monotonously decreased from 92 to 87 K with increasing the  $\text{Gd}_2\text{O}_3$  contents up to 10 mol%. The optimum doping content is 5 mol% at lower temperatures below 40 K since only the GdBCO film with 5 mol%  $\text{Gd}_2\text{O}_3$

addition exhibits improved pinning properties at 20 and 40 K compared with undoped GdBCO film. The round-shaped  $\text{Gd}_2\text{O}_3$  nanoparticles with an average diameter of 18 nm, randomly dispersed in the GdBCO matrix, might be responsible for enhanced pinning properties.

Also, both the pristine and  $\text{Eu}_2\text{O}_3$ -doped EuBCO films were prepared on the  $\text{CeO}_2$ -buffered MgO (100) single crystal substrates by the PLD process employing the surface modified target in order to investigate the pinning properties of  $\text{Eu}_2\text{O}_3$ -doped EuBCO films. With increasing  $\text{Eu}_2\text{O}_3$  doping contents up to 8 mol%, the  $T_{c,zero}$  values of  $\text{Eu}_2\text{O}_3$ -doped EuBCO films were degraded from 91.4 to 87.1 K. Among the  $\text{Eu}_2\text{O}_3$ -doped EuBCO films, the 4 mol%  $\text{Eu}_2\text{O}_3$ -doped EuBCO exhibited the highest  $J_c$  and  $F_{p,max}$  values for  $B//c$  below 40 K, indicating the optimum doping content is 4 mol% at lower temperatures. From the HR-TEM analysis results, it was obvious that the round-shaped  $\text{Eu}_2\text{O}_3$  nanoparticles with average diameter of 18 nm, which were randomly dispersed in the matrix, were responsible for the enhancement of pinning properties below 40 K. However, the pinning properties of the  $\text{Eu}_2\text{O}_3$ -doped EuBCO films at relatively high temperatures were degraded, which were attributable to the significant  $T_{c,zero}$  drop. We identified that the  $T_{c,zero}$  drop of  $\text{Eu}_2\text{O}_3$ -doped EuBCO films originated from the formation of the solid solution and strain effect. Unlike the  $\text{Y}_2\text{O}_3$ -doped YBCO films, the  $\text{RE}_2\text{O}_3$ -doped REBCO films were affected seriously by the solid solution in addition to the strain effect, leading to the degradation of pinning properties at higher temperatures.

## References

- [1] Y. Yamada, K. Takahashi, H. Kobayashi, M. Konishi, T. Watanabe, A. Ibi, T. Muroga, S. Miyata, T. Kato, and T. Hirayama, "Epitaxial nanostructure and defects effective for pinning in Y(RE)Ba<sub>2</sub>Cu<sub>3</sub>O<sub>7-x</sub> coated conductors," *Applied Physics Letters*, vol. 87, no. 13, p. 132502, 2005.
- [2] T. Kato, H. Sasaki, Y. Gotoh, Y. Sasaki, T. Hirayama, K. Takahashi, M. Konishi, H. Kobayashi, A. Ibi, and T. Muroga, "Nanostructural characterization of Y123 and Gd123 with BaZrO<sub>3</sub> rods fabricated by pulsed-laser deposition," *Physica C: Superconductivity and its applications*, vol. 445, pp. 628-632, 2006.
- [3] K. Takahashi, H. Kobayashi, Y. Yamada, A. Ibi, H. Fukushima, M. Konishi, S. Miyata, Y. Shiohara, T. Kato, and T. Hirayama, "Investigation of thick PLD-GdBCO and ZrO<sub>2</sub> doped GdBCO coated conductors with high critical current on PLD-CeO<sub>2</sub> capped IBAD-GZO substrate tapes," *Superconductor Science and Technology*, vol. 19, no. 9, p. 924, 2006.
- [4] T. Horide, K. Matsumoto, A. Ichinose, M. Mukaida, Y. Yoshida, and S. Horii, "Vortex Pinning by Gold Nanorods in GdBa<sub>2</sub>Cu<sub>3</sub>O<sub>7-δ</sub> Thin Films," *IEEE Transactions on Applied Superconductivity*, vol. 17, no. 2, pp. 3729-3732, 2007.
- [5] Y. Shiohara, M. Yoshizumi, T. Izumi, and Y. Yamada, "Present status and future prospect of coated conductor development and its application in Japan," *Superconductor Science and Technology*, vol. 21, no. 3, p. 034002, 2008.
- [6] S. Lee, N. Chikumoto, T. Yokoyama, T. Machi, K. Nakao, and K. Tanabe, "Development of in-plume pulsed laser deposition of high-I<sub>c</sub> GdBCO films for coated conductors," *IEEE Transactions on Applied*

- Superconductivity*, vol. 19, no. 3, pp. 3192-3195, 2009.
- [7] K. Schlesier, H. Huhtinen, P. Paturi, Y. P. Stepanov, and R. Laiho, "Structural and superconducting properties of undoped and BZO-doped GdBCO thin films," *IEEE Transactions on Applied Superconductivity*, vol. 19, no. 3, pp. 3407-3411, 2009.
- [8] K. Kaneko, K. Furuya, K. Yamada, S. Sadayama, J. Barnard, P. Midgley, T. Kato, T. Hirayama, M. Kiuchi, and T. Matsushita, "Three-dimensional analysis of BaZrO<sub>3</sub> pinning centers gives isotropic superconductivity in GdBa<sub>2</sub>Cu<sub>3</sub>O<sub>7- $\delta$</sub> ," *Journal of Applied Physics*, vol. 108, no. 6, p. 063901, 2010.
- [9] T. Matsushita, H. Nagamizu, K. Tanabe, M. Kiuchi, E. Otake, H. Tobita, M. Yoshizumi, T. Izumi, Y. Shiohara, and D. Yokoe, "Improvement of flux pinning performance at high magnetic fields in GdBa<sub>2</sub>Cu<sub>3</sub>O<sub>y</sub> coated conductors with BHO nano-rods through enhancement of B<sub>c2</sub>," *Superconductor Science and Technology*, vol. 25, no. 12, p. 125003, 2012.
- [10] H. Tobita, K. Notoh, K. Higashikawa, M. Inoue, T. Kiss, T. Kato, T. Hirayama, M. Yoshizumi, T. Izumi, and Y. Shiohara, "Fabrication of BaHfO<sub>3</sub> doped Gd<sub>1</sub>Ba<sub>2</sub>Cu<sub>3</sub>O<sub>7- $\delta$</sub>  coated conductors with the high I<sub>c</sub> of 85 A/cm-w under 3 T at liquid nitrogen temperature (77 K)," *Superconductor Science and Technology*, vol. 25, no. 6, p. 062002, 2012.
- [11] D. Tran, W. Putri, C. Wie, B. Kang, N. Lee, W. Kang, J. Lee, and W. Seong, "Thickness dependence of critical current density in GdBa<sub>2</sub>Cu<sub>3</sub>O<sub>7- $\delta$</sub>  thin films with BaSnO<sub>3</sub> addition," *Journal of Applied Physics*, vol. 111, no. 7, p. 07D714, 2012.
- [12] D. Tran, W. Putri, B. Kang, N. Lee, W. Kang, and W. Seong, "Reducing thickness dependence of critical current density in GdBa<sub>2</sub>Cu<sub>3</sub>O<sub>7- $\delta$</sub>  thin films by addition of nanostructured defects," *Journal of Applied Physics*, vol. 113, no. 17, p. 17E134, 2013.

- [13] K.-P. Ko, S.-M. Choi, J.-W. Lee, R.-K. Ko, S.-H. Moon, C. Park, and S.-I. Yoo, "Optimization of the BaSnO<sub>3</sub> Doping Content in GdBa<sub>2</sub>Cu<sub>3</sub>O<sub>7-δ</sub> Coated Conductors by Pulsed Laser Deposition," *IEEE Transactions on Applied Superconductivity*, vol. 24, no. 6, pp. 1-8, 2014.
- [14] P. Mele, K. Matsumoto, T. Horide, A. Ichinose, M. Mukaida, Y. Yoshida, and S. Horii, "Insertion of nanoparticulate artificial pinning centres in YBa<sub>2</sub>Cu<sub>3</sub>O<sub>7-x</sub> films by laser ablation of a Y<sub>2</sub>O<sub>3</sub>-surface modified target," *Superconductor Science and Technology*, vol. 20, no. 7, p. 616, 2007.
- [15] K. Matsumoto and P. Mele, "Artificial pinning center technology to enhance vortex pinning in YBCO coated conductors," *Superconductor Science and Technology*, vol. 23, no. 1, p. 014001, 2009.
- [16] T. Horide, T. Kawamura, K. Matsumoto, A. Ichinose, M. Yoshizumi, T. Izumi, and Y. Shiohara, "J<sub>c</sub> improvement by double artificial pinning centers of BaSnO<sub>3</sub> nanorods and Y<sub>2</sub>O<sub>3</sub> nanoparticles in YBa<sub>2</sub>Cu<sub>3</sub>O<sub>7</sub> coated conductors," *Superconductor Science and Technology*, vol. 26, no. 7, p. 075019, 2013.
- [17] M. A. P. Sebastian, J. N. Reichart, M. M. Ratcliff, T. J. Bullard, J. L. Burke, C. R. Ebbing, G. Y. Panasyuk, C.-F. Tsai, W. Zhang, and J. Huang, "Study of the flux pinning landscape of YBCO thin films with single and mixed phase additions BaMO<sub>3</sub> + Z: M= Hf, Sn, Zr and Z= Y<sub>2</sub>O<sub>3</sub>, Y<sub>2</sub>11," *IEEE Transactions on Applied Superconductivity*, vol. 27, no. 4, pp. 1-5, 2017.
- [18] E. Gyorgy, R. Van Dover, K. Jackson, L. Schneemeyer, and J. Waszczak, "Anisotropic critical currents in Ba<sub>2</sub>YCu<sub>3</sub>O<sub>7</sub> analyzed using an extended Bean model," *Applied physics letters*, vol. 55, no. 3, pp. 283-285, 1989.
- [19] T. Ozaki, Y. Yoshida, Y. Ichino, Y. Takai, K. Matsumoto, A. Ichinose, S. Horii, and M. Mukaida, "Flux pinning properties of Sm<sub>1+x</sub>Ba<sub>2-x</sub>Cu<sub>3</sub>O<sub>y</sub> films with BaZrO<sub>3</sub> nanorods fabricated by low-

- temperature growth technique," *Physica C: Superconductivity*, vol. 468, no. 15-20, pp. 1615-1618, 2008.
- [20] P. Mele, K. Matsumoto, A. Ichinose, M. Mukaida, Y. Yoshida, S. Horii, and R. Kita, "Systematic study of the BaSnO<sub>3</sub> insertion effect on the properties of YBa<sub>2</sub>Cu<sub>3</sub>O<sub>7-x</sub> films prepared by pulsed laser ablation," *Superconductor Science and Technology*, vol. 21, no. 12, p. 125017, 2008.
- [21] J. MacManus-Driscoll, S. Foltyn, Q. Jia, H. Wang, A. Serquis, L. Civale, B. Maiorov, M. Hawley, M. Maley, and D. Peterson, "Strongly enhanced current densities in superconducting coated conductors of YBa<sub>2</sub>Cu<sub>3</sub>O<sub>7-x</sub>+ BaZrO<sub>3</sub>," *Nature materials*, vol. 3, no. 7, p. 439, 2004.
- [22] R. Teranishi, S. Yasunaga, H. Kai, K. Yamada, M. Mukaida, N. Mori, T. Fujiyoshi, A. Ichinose, S. Horii, and K. Matsumoto, "Superconducting properties of ErBCO films with BaMO<sub>3</sub> nanorods (M= Zr and Sn) by pulsed laser deposition," *Physica C: Superconductivity*, vol. 468, no. 15-20, pp. 1522-1526, 2008.
- [23] A. Ichinose, P. Mele, K. Matsumoto, H. Kai, M. Takamura, K. Yamada, M. Mukaida, S. Horii, S. Funaki, and Y. Ichino, "Microstructures of REBa<sub>2</sub>Cu<sub>3</sub>O<sub>y</sub> films containing artificial pinning centers of various dimensions," *Physica C: Superconductivity*, vol. 469, no. 15-20, pp. 1374-1379, 2009.
- [24] L. Civale, B. Maiorov, A. Serquis, S. Foltyn, Q. Jia, P. Arendt, H. Wang, J. Willis, J. Coulter, and T. Holesinger, "Influence of crystalline texture on vortex pinning near the ab-plane in YBa<sub>2</sub>Cu<sub>3</sub>O<sub>7</sub> thin films and coated conductors," *Physica C: Superconductivity*, vol. 412, pp. 976-982, 2004.
- [25] L. Civale, B. Maiorov, J. MacManus-Driscoll, H. Wang, T. Holesinger, S. Foltyn, A. Serquis, and P. Arendt, "Identification of intrinsic ab-plane pinning in YBa<sub>2</sub>Cu<sub>3</sub>O<sub>7</sub> thin films and coated conductors," *IEEE transactions on applied superconductivity*, vol. 15, no. 2, pp. 2808-

2811, 2005.

- [26] W.-J. Oh, J.-E. Kim, and S.-I. Yoo, "Enhanced Pinning Properties of  $\text{GdBa}_2\text{Cu}_3\text{O}_{7-\delta}$  Films With the  $\text{Gd}_2\text{O}_3$  Nanoparticles," *IEEE Transactions on Applied Superconductivity*, vol. 27, no. 4, pp. 1-5, 2016.
- [27] P. Mele, R. Guzman, J. Gazquez, T. Puig, X. Obradors, S. Saini, Y. Yoshida, M. Mukaida, A. Ichinose, and K. Matsumoto, "High pinning performance of  $\text{YBa}_2\text{Cu}_3\text{O}_{7-x}$  films added with  $\text{Y}_2\text{O}_3$  nanoparticulate defects," *Superconductor Science and Technology*, vol. 28, no. 2, p. 024002, 2014.
- [28] L. Civale, B. Maiorov, A. Serquis, J. Willis, J. Coulter, H. Wang, Q. Jia, P. Arendt, J. a. MacManus-Driscoll, and M. Maley, "Angular-dependent vortex pinning mechanisms in  $\text{YBa}_2\text{Cu}_3\text{O}_7$  coated conductors and thin films," *Applied Physics Letters*, vol. 84, no. 12, pp. 2121-2123, 2004.
- [29] V. Rouco, A. Palau, R. Guzman, J. Gazquez, M. Coll, X. Obradors, and T. Puig, "Role of twin boundaries on vortex pinning of CSD YBCO nanocomposites," *Superconductor Science and Technology*, vol. 27, no. 12, p. 125009, 2014.
- [30] A. A. Armenio, L. Piperno, G. De Marzi, V. Pinto, A. Mancini, F. Rizzo, A. Vannozzi, A. Rufoloni, A. Augieri, and R. B. Mos, "Stranger APCs: Study of surface decoration material for YBCO films," *IEEE Transactions on Applied Superconductivity*, vol. 29, no. 5, pp. 1-5, 2019.
- [31] K. Takahashi, Y. Yamada, M. Konishi, T. Watanabe, A. Ibi, T. Muroga, S. Miyata, Y. Shiohara, T. Kato, and T. Hirayama, "Magnetic field dependence of  $J_c$  for Gd-123 coated conductor on PLD- $\text{CeO}_2$  capped IBAD-GZO substrate tapes," *Superconductor Science and Technology*, vol. 18, no. 8, p. 1118, 2005.
- [32] J. Wang, J. Kwon, J. Yoon, H. Wang, T. Haugan, F. Baca, N. Pierce, and P. Barnes, "Flux pinning in  $\text{YBa}_2\text{Cu}_3\text{O}_{7-\delta}$  thin film samples linked to stacking fault density," *Applied Physics Letters*, vol. 92, no. 8, p.

- 082507, 2008.
- [33] J. Gazquez, M. Coll, N. Roma, F. Sandiumenge, T. Puig, and X. Obradors, "Structural defects in trifluoroacetate derived  $\text{YBa}_2\text{Cu}_3\text{O}_7$  thin films," *Superconductor Science and Technology*, vol. 25, no. 6, p. 065009, 2012.
- [34] R. Schalk, K. Kundzins, H. Weber, E. Stangl, S. Proyer, and D. Bäuerle, "STM observation of dislocation chains suitable for flux pinning in  $\text{YBa}_2\text{Cu}_3\text{O}_{7-x}$  films," *Physica C: Superconductivity and its Applications*, vol. 257, no. 3-4, pp. 341-354, 1996.
- [35] B. Dam, J. Huijbregtse, F. Klaassen, R. Van der Geest, G. Doornbos, J. Rector, A. Testa, S. Freisem, J. Martinez, and B. Stäuble-Pümpin, "Origin of high critical currents in  $\text{YBa}_2\text{Cu}_3\text{O}_{7-\delta}$  superconducting thin films," *Nature*, vol. 399, no. 6735, p. 439, 1999.
- [36] F. Klaassen, G. Doornbos, J. Huijbregtse, R. Van der Geest, B. Dam, and R. Griessen, "Vortex pinning by natural linear defects in thin films of  $\text{YBa}_2\text{Cu}_3\text{O}_{7-\delta}$ ," *Physical Review B*, vol. 64, no. 18, p. 184523, 2001.
- [37] J. Huijbregtse, F. Klaassen, A. Szepielow, J. Rector, B. Dam, R. Griessen, B. Kooi, and J. T. M. De Hosson, "Vortex pinning by natural defects in thin films of  $\text{YBa}_2\text{Cu}_3\text{O}_{7-\delta}$ ," *Superconductor Science and Technology*, vol. 15, no. 3, p. 395, 2002.
- [38] V. Pan, Y. Cherpak, V. Komashko, S. Pozigun, C. Tretiatchenko, A. Semenov, E. Pashitskii, and A. V. Pan, "Supercurrent transport in  $\text{YBa}_2\text{Cu}_3\text{O}_{7-\delta}$  epitaxial thin films in a dc magnetic field," *Physical Review B*, vol. 73, no. 5, p. 054508, 2006.
- [39] K. Zhang, B. Dabrowski, C. Segre, D. Hinks, I. K. Schuller, J. Jorgensen, and M. Slaski, "Solubility and superconductivity in  $\text{RE}(\text{Ba}_{2-x}\text{RE}_x)\text{Cu}_3\text{O}_{7+\delta}$  systems (RE= Nd, Sm, Eu, Gd, Dy)," *Journal of Physics C: Solid State Physics*, vol. 20, no. 34, p. L935, 1987.
- [40] M. Murakami, N. Sakai, T. Higuchi, and S. Yoo, "Melt-processed light rare earth element-Ba-Cu-O," *Superconductor Science and Technology*,

- vol. 9, no. 12, p. 1015, 1996.
- [41] M. Kramer, S. Yoo, R. McCallum, W. Yelon, H. Xie, and P. Allenspach, "Hole filling, charge transfer and superconductivity in  $\text{Nd}_{1+x}\text{Ba}_{2-x}\text{Cu}_3\text{O}_{7+\delta}$ ," *Physica C: Superconductivity*, vol. 219, no. 1-2, pp. 145-155, 1994.
- [42] K. Miyachi, K. Sudoh, Y. Ichino, Y. Yoshida, and Y. Takai, "The effect of the substitution of Gd for Ba site on  $\text{Gd}_{1+x}\text{Ba}_{2-x}\text{Cu}_3\text{O}_{6+\delta}$  thin films," *Physica C: Superconductivity*, vol. 392, pp. 1261-1264, 2003.
- [43] A. Ichinose, K. Naoe, T. Horide, K. Matsumoto, R. Kita, M. Mukaida, Y. Yoshida, and S. Horii, "Microstructures and critical current densities of YBCO films containing structure-controlled  $\text{BaZrO}_3$  nanorods," *Superconductor Science and Technology*, vol. 20, no. 12, p. 1144, 2007.
- [44] A. Tsuruta, Y. Yoshida, Y. Ichino, A. Ichinose, K. Matsumoto, and S. Awaji, "The influence of the geometric characteristics of nanorods on the flux pinning in high-performance  $\text{BaMO}_3$ -doped  $\text{SmBa}_2\text{Cu}_3\text{O}_y$  films (M= Hf, Sn)," *Superconductor Science and Technology*, vol. 27, no. 6, p. 065001, 2014.
- [45] S. Miura, Y. Yoshida, Y. Ichino, K. Matsumoto, A. Ichinose, and S. Awaji, "Characteristics of high-performance  $\text{BaHfO}_3$ -doped  $\text{SmBa}_2\text{Cu}_3\text{O}_y$  superconducting films fabricated with a seed layer and low-temperature growth," *Superconductor Science and Technology*, vol. 28, no. 6, p. 065013, 2015.
- [46] M. Miura, B. Maiorov, M. Sato, M. Kanai, T. Kato, T. Kato, T. Izumi, S. Awaji, P. Mele, and M. Kiuchi, "Tuning nanoparticle size for enhanced functionality in perovskite thin films deposited by metal organic deposition," *NPG Asia Materials*, vol. 9, no. 11, p. e447, 2017.
- [47] T. Horide, F. Kametani, S. Yoshioka, T. Kitamura, and K. Matsumoto, "Structural evolution induced by interfacial lattice mismatch in self-organized  $\text{YBa}_2\text{Cu}_3\text{O}_{7-\delta}$  nanocomposite film," *ACS Nano*, vol. 11, no. 2, pp. 1780-1788, 2017.

- [48] J.-E. Kim, "Enhanced pinning properties of  $\text{EuBa}_2\text{Cu}_3\text{O}_{7-\delta}$  films with  $\text{Eu}_2\text{O}_3$  addition prepared by pulsed laser deposition," Master thesis, Seoul National University, 2017.
- [49] A. A. Armenio, V. Pinto, A. Mancini, A. Augieri, V. Galluzzi, F. Rizzo, A. Rufoloni, A. Vannozzi, and G. Celentano, "Analysis of the growth process and pinning mechanism of low-fluorine MOD  $\text{YBa}_2\text{Cu}_3\text{O}_{7-\delta}$  films with and without  $\text{BaZrO}_3$  artificial pinning centers," *IEEE Transactions on Applied Superconductivity*, vol. 25, no. 3, pp. 1-5, 2015.
- [50] W.-J. Oh, I. Park, J.-H. Lee, H. Lee, S.-H. Moon, K. Shinde, K. Chung, and S.-I. Yoo, "The Post-Annealing Effect on the Pinning Properties of  $\text{GdBa}_2\text{Cu}_3\text{O}_{7-\delta}$  Coated Conductors via RCE-DR," *IEEE Transactions on Applied Superconductivity*, vol. 28, no. 4, 2018.

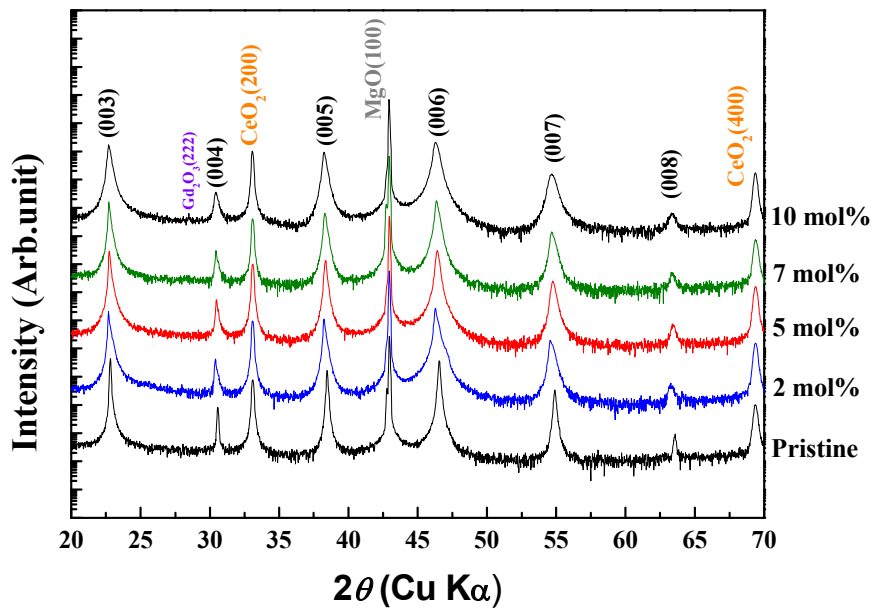


Fig. 2.1. XRD patterns of all GdBCO films deposited on CeO<sub>2</sub>-buffered MgO (100) substrates

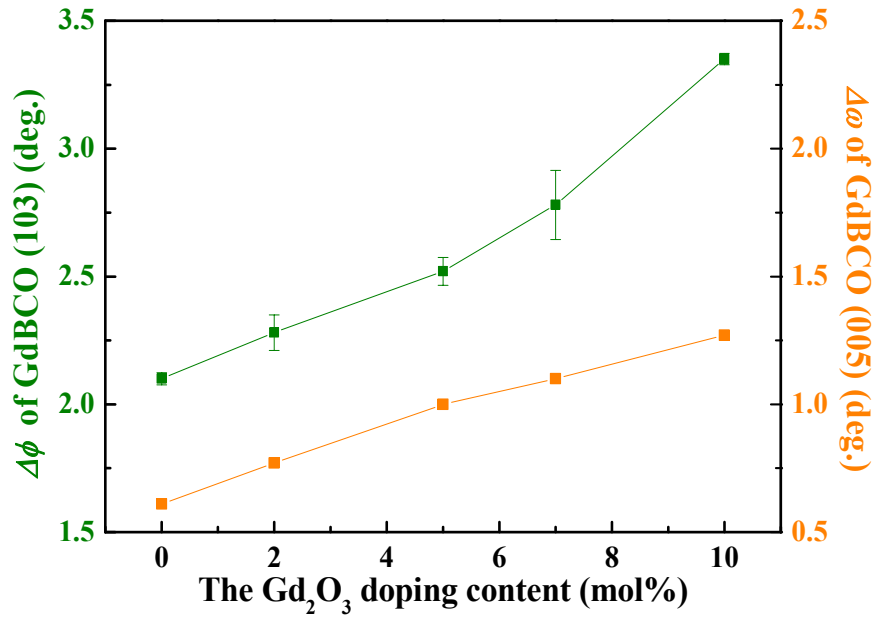


Fig. 2.2. The in-plane ( $\Delta\phi$ ) and out-of-plane textures ( $\Delta\omega$ ) of  $\omega$ -scan of all GdBCO films as a function of the Gd<sub>2</sub>O<sub>3</sub> doping content.

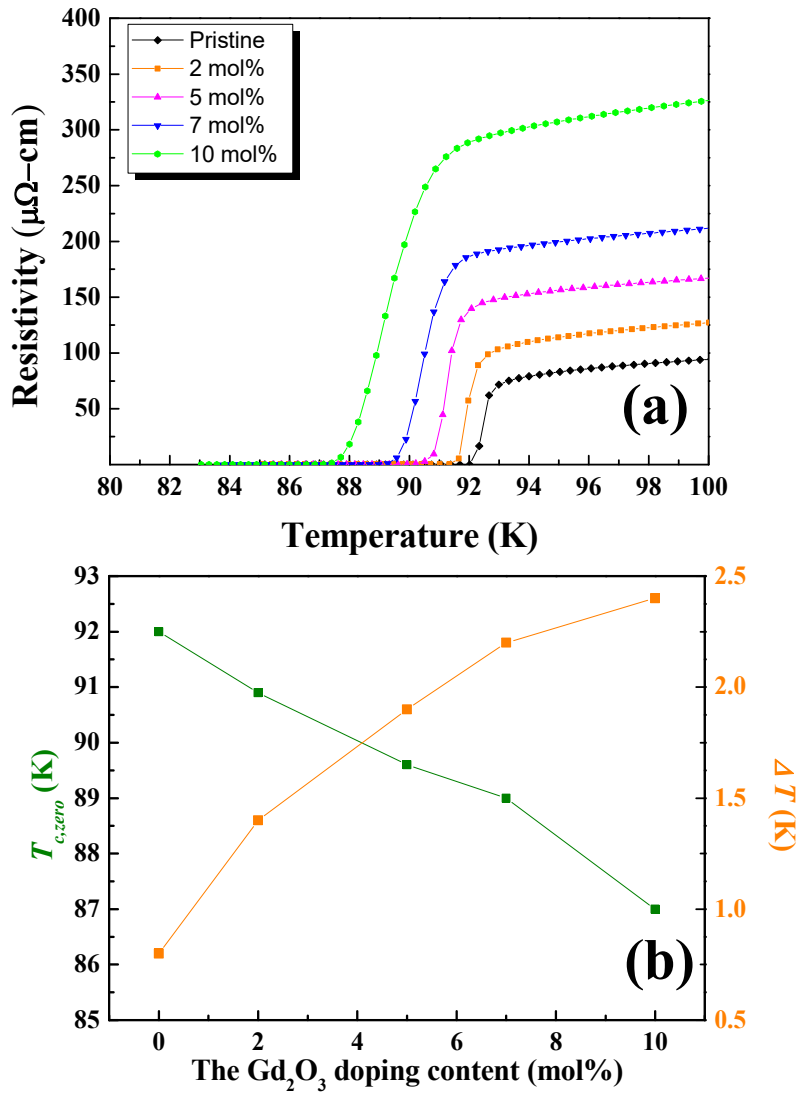


Fig. 2.3. (a) Electrical resistivity versus temperature curves, (b) the variation of the  $T_{c,zero}$  and  $\Delta T$  values with increasing  $\text{Gd}_2\text{O}_3$  doping contents for all GdBCO samples.

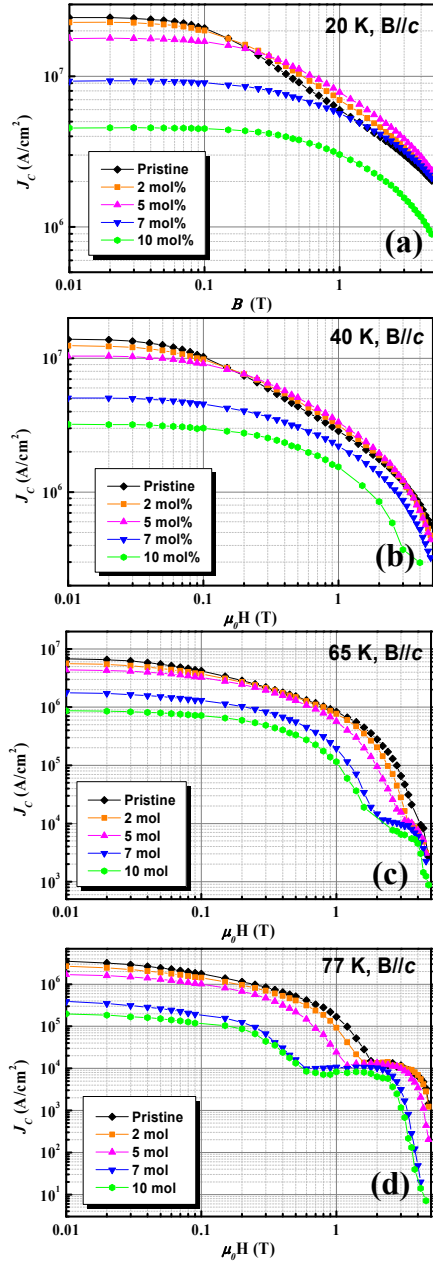


Fig. 2.4. Magnetic  $J_c$  versus applied field for all GdBCO films at (a) 20, (b) 40, (c) 65, and (d) 77 K

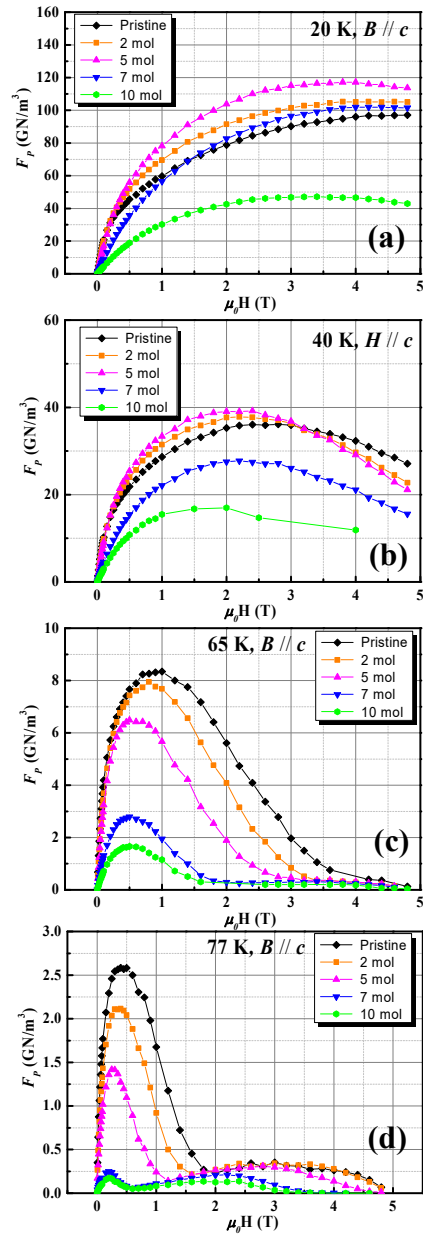


Fig. 2.5. The pinning force density ( $F_p = J_c \times B$ ) values at (a) 20, (b) 40, (c) 65, and (d) 77 K for  $B // c$  as a function of the magnetic field for all samples.

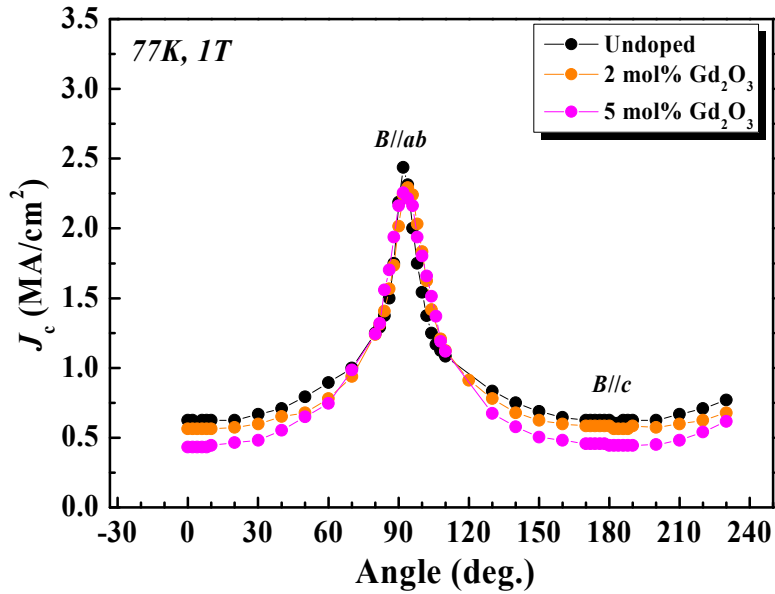


Fig. 2.6. Field-orientation dependence of the transport  $J_c$  values for undoped, 2mol% and 5 mol% Gd<sub>2</sub>O<sub>3</sub>-doped GdBCO samples measured at 77 K, 1 T

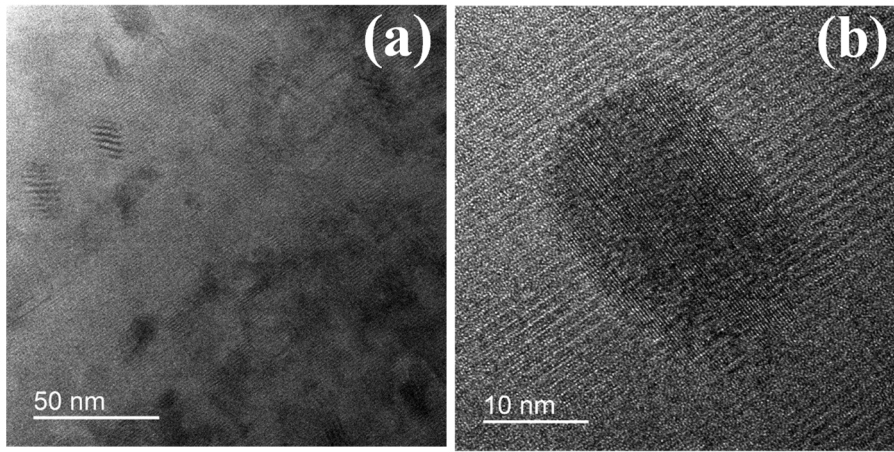


Fig. 2.7. Cross-section HR-TEM images of 5 mol%  $\text{Gd}_2\text{O}_3$ -doped GdBCO film.

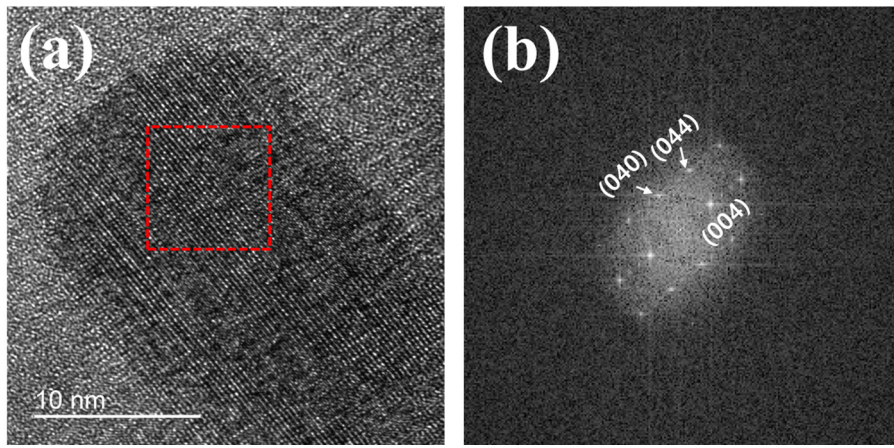


Fig. 2.8. (a) Cross-section HR-TEM images and (b) FFT indexing diffraction data of 5 mol%  $\text{Gd}_2\text{O}_3$ -doped GdBCO film.

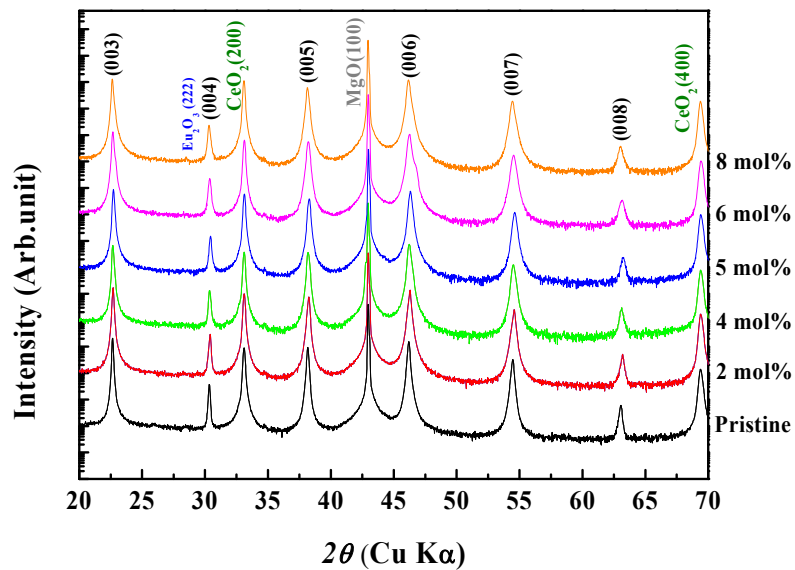


Fig. 2.9. XRD patterns of all EuBCO films deposited on CeO<sub>2</sub>-buffered MgO (100) substrates [48].

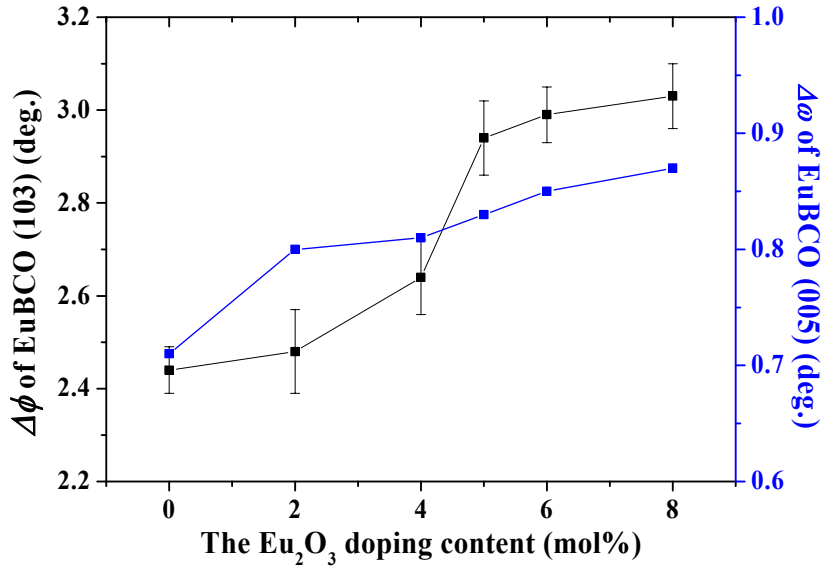


Fig. 2.10. The in-plane ( $\Delta\phi$ ) and out-of-plane textures ( $\Delta\omega$ ) of  $\omega$ -scan of EuBCO films as a function of the  $\text{Eu}_2\text{O}_3$  doping content [48].

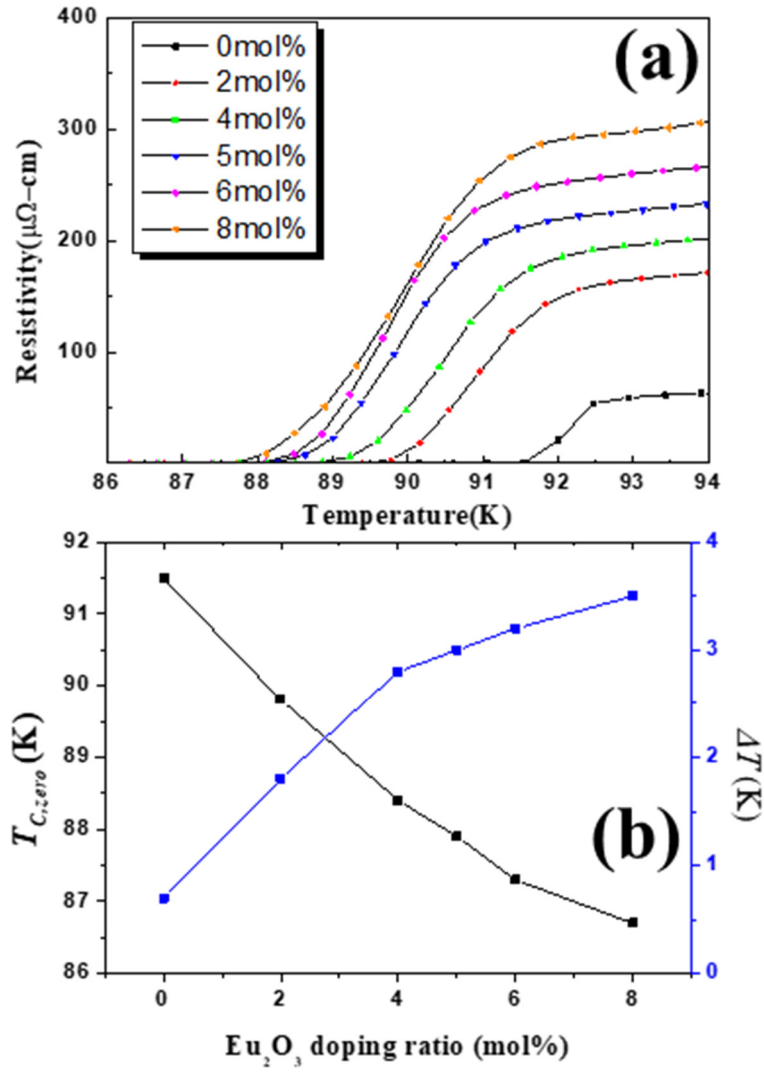


Fig. 2.11. (a) Electrical resistivity versus temperature curves, (b) the variation of the  $T_{c,zero}$  and  $\Delta T$  values with increasing  $\text{Eu}_2\text{O}_3$  doping contents for all EuBCO samples [48].

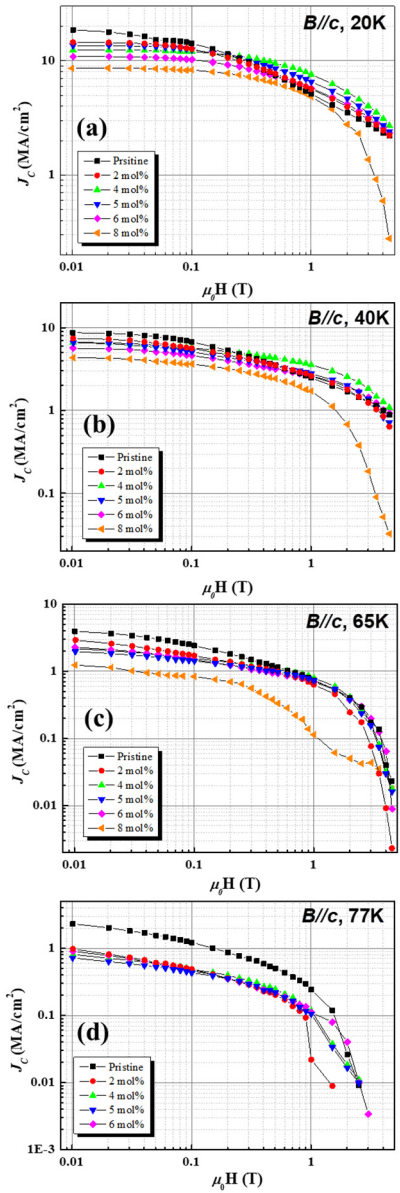


Fig. 2.12. Magnetic  $J_c$  versus magnetic field applied parallel to the  $c$ -axis for pristine and 2-8 mol%  $\text{Eu}_2\text{O}_3$ -doped EuBCO films at (a) 20, (b) 40, (c) 65 and (d) 77 K [48].

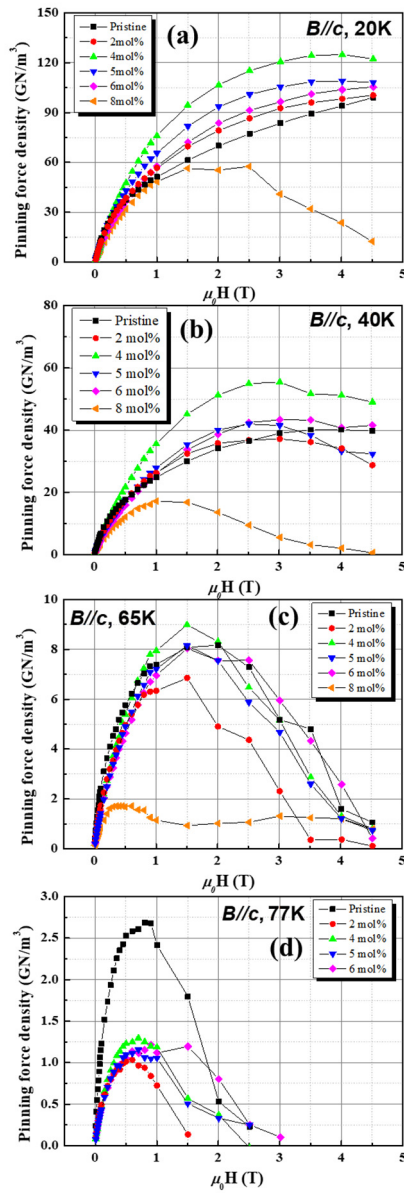


Fig. 2.13. The pinning force density ( $F_p = J_c \times B$ ) values at (a) 20, (b) 40, (c) 65 and (d) 77 K for  $B//c$  as a function of the magnetic field for pristine and 2-8 mol%  $\text{Eu}_2\text{O}_3$ -doped EuBCO films [48].

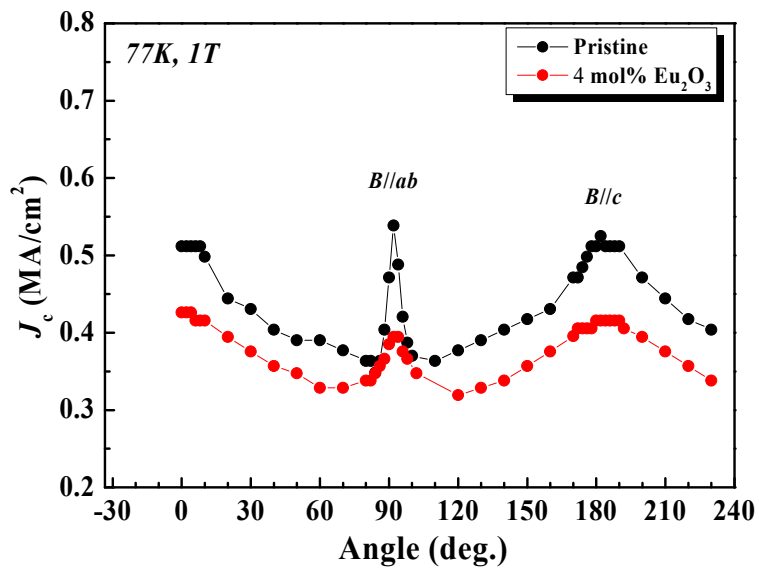


Fig. 2.14. Field-orientation dependence of the transport  $J_c$  values for pristine, and 4 mol%  $\text{Eu}_2\text{O}_3$ -doped EuBCO samples measured at 77 K, 1 T.

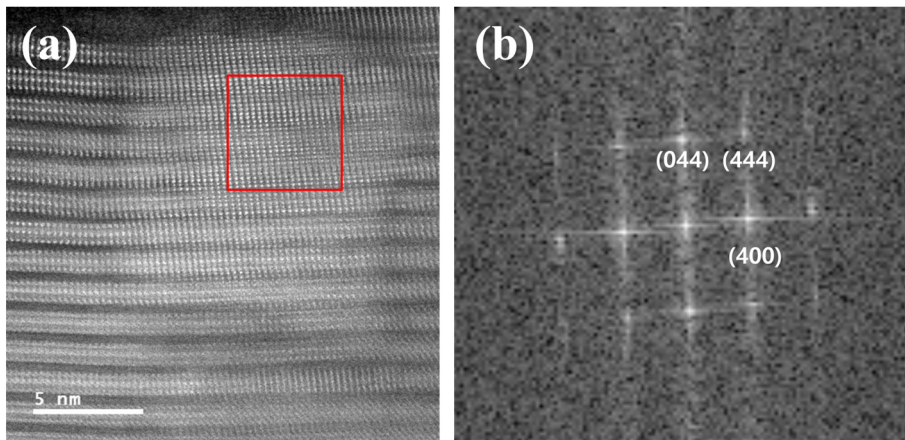


Fig. 2.15. Cross-sectional HR-STEM image (a) and FFT indexing diffraction data (b) of 4 mol%  $\text{Eu}_2\text{O}_3$ -doped EuBCO films by PLD.

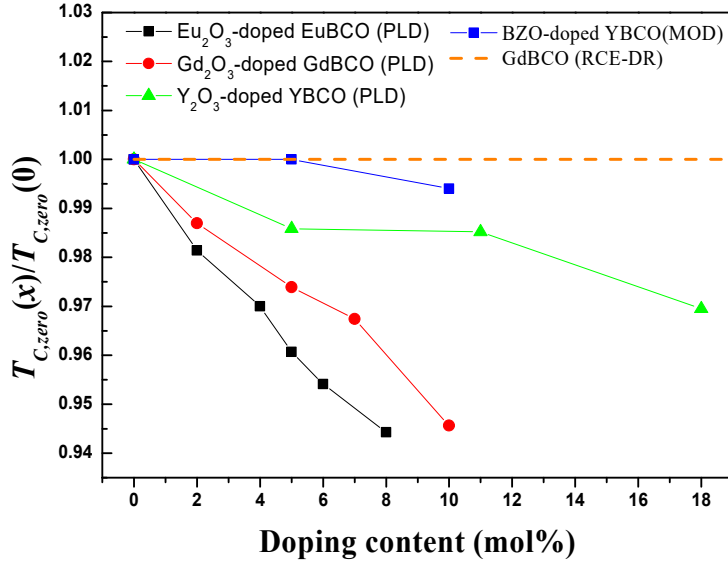


Fig. 2.16. The comparison of the  $T_{c,zero}$  and  $\Delta T$  values with increasing doping contents for Y<sub>2</sub>O<sub>3</sub>-doped YBCO by PLD [27], RE<sub>2</sub>O<sub>3</sub>-doped REBCO by PLD (RE = Eu [this study], Gd [26]), BZO-doped YBCO by MOD [49], and GdBCO CCs by RCE-DR [50], REBCO samples.

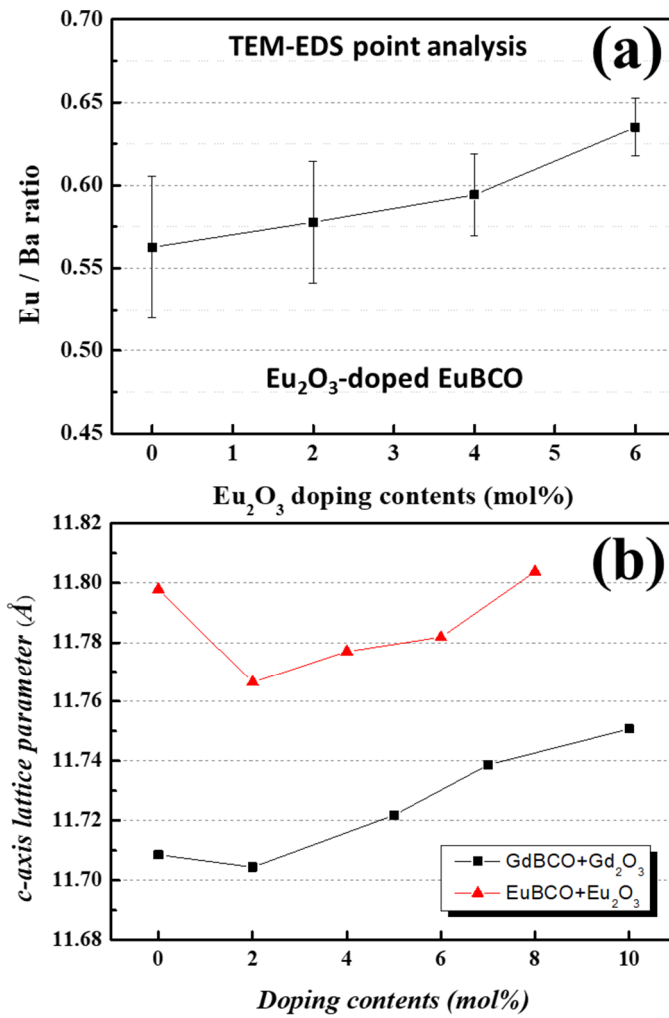


Fig. 2.17. (a) Eu/Ba elements ratio and (b) *c*-axis lattice parameter as function of RE<sub>2</sub>O<sub>3</sub> doping contents

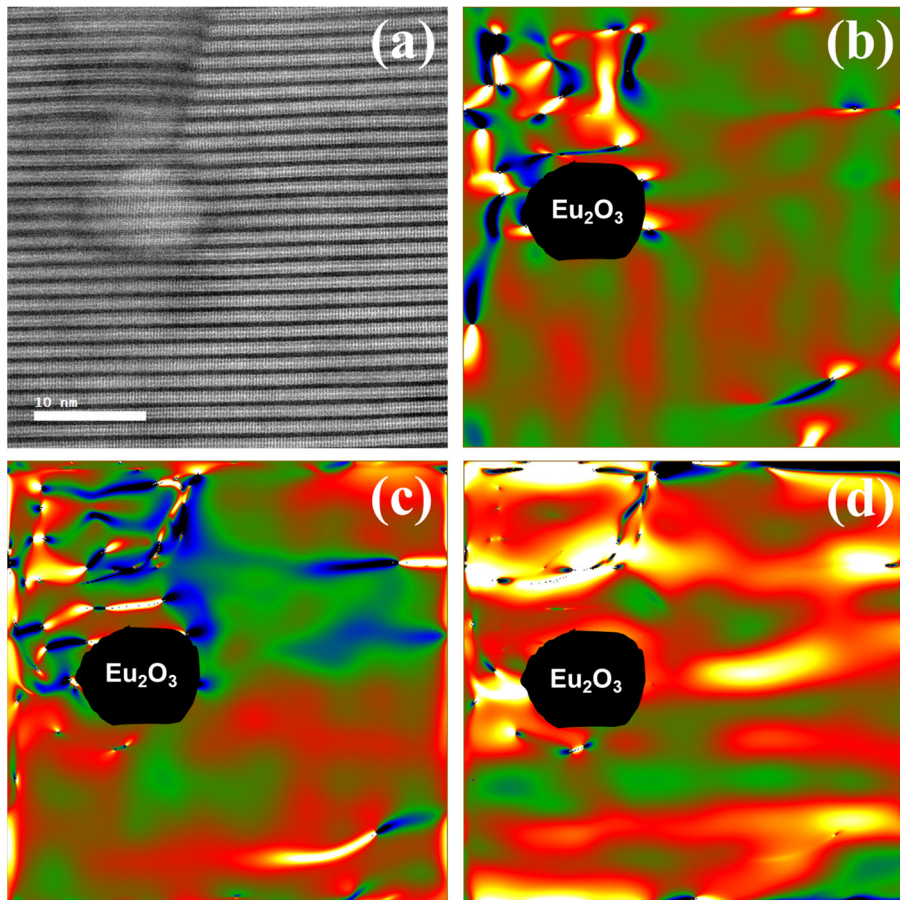


Fig. 2.18. (a) HAADF-STEM image of 4 mol%  $\text{Eu}_2\text{O}_3$ -doped EuBCO films, nanostrain maps of (b)  $\epsilon_{xx}$ , (c)  $\epsilon_{xz}$ , and (d)  $\epsilon_{zz}$ ,

## **Chapter 3. Origin of $J_c$ peak along the $c$ -axis direction for the GdBCO films by the PLD process**

### **3.1. Introduction**

Since the reason for the degradation of in-field  $J_c$  is the Lorentz force which causes the motion of flux lines, it is important to introduce pinning centers into the matrix in order to improve pinning properties. In general, the pinning centers can be roughly categorized as natural defects and APCs. A wide variety of defects which can act as pinning centers can be formed in the superconducting matrix [1]. In terms of naturally generated defects, there were many reports such as oxygen vacancies [2, 3], cation disorder [4], dislocation [5-9], small angle boundaries [9, 10], twin boundaries [11, 12], anti-phase boundaries [13], SFs [14-17], and etc. However, understanding the relationship between naturally generated defects and in-field  $J_c$  is quite complicated.

Among the previous studies, especially, there were different arguments about defects operating as the  $c$ -axis correlated pinning centers such as precipitates [18], twin boundaries [19-21], dislocation [5-9] and SFs [14-17]. The difference of origin for  $J_c$  peak for  $B//c$  has motivated this study to identify the accurate interpretation using the GdBCO films by the PLD process. In this study, we suggested the empirical evidence of  $c$ -axis correlated defects operating pinning centers in the GdBCO matrix. To clarify the mechanism of the pinning behavior, we employed the TEM microstructure analysis and  $J_c$ - $B$ - $T$ - $\theta$  measurement.

## 3.2. Experimental

The GdBCO films were deposited on CeO<sub>2</sub>-buffered MgO (100) single crystal substrate using the PLD process. The biaxial textured CeO<sub>2</sub> buffer layers on MgO (100) single crystal substrate were grown by RF-magnetron sputtering. The details of deposition conditions were described in chapter 2. The GdBCO targets were prepared by the solid-state reaction employing precursors of Gd<sub>2</sub>O<sub>3</sub> (High Purity Co., 99.9%), BaCO<sub>3</sub> (Cerac., 99.9%), and CuO (High Purity Co., 99.9%). A Lambda Physik KrF excimer laser ( $\lambda = 248$  nm) was used to deposit GdBCO films at the energy density of  $\sim 1.5$  J/cm<sup>2</sup> and the laser frequency of 8 Hz. The substrate temperature of 800°C and the oxygen pressure of 300 mTorr were used to fabricate GdBCO films. The details of growth condition were described in chapter 2. For fabrication of another GdBCO films having the  $J_c$  peak for  $B//c$ , we adjusted the position of a laser focal point. The sample A was fabricated by the narrow spot size compared to the sample B. After deposition, all samples were annealed at 500°C for 1 h in a pure oxygen atmosphere.

The XRD patterns were obtained using an X-ray diffractometer (Bruker D8-Advance, Cu K $\alpha$  radiation). The in-plane texture ( $\Delta\phi$ ) and out-of-texture ( $\Delta\omega$ ) of GdBCO films were analyzed by high resolution (HR) XRD (PANalytical X'pert Pro). Field emission-scanning electron microscopy (FE-SEM, MERLIN Compact) and scanning transmission electron microscopy (STEM, JEOL JEM-ARM200F) were employed to characterize the microstructures of samples. Also, STEM-EDS (energy dispersive X-ray spectroscopy) was employed to perform the compositional analyses. A standard four-point probe technique was

used to measure the superconducting properties of samples. The angular dependence of transport  $J_c$  values were evaluated by measuring the  $I$ - $V$  curves with the  $1 \mu\text{V}/\text{cm}$  criterion using the physical property measurement system (PPMS, Quantum Design model-6000).

### 3.3. Results and discussion

Fig. 3.1 shows the  $\theta$ - $2\theta$  scans of both sample A and B films deposited on  $\text{CeO}_2$ -buffered  $\text{MgO}$  (100) substrate. As shown in Fig. 3.1, the GdBCO (00 $l$ ) reflections are observable in the XRD patterns of GdBCO films, indicating that all GdBCO films are strongly  $c$ -axis oriented. The typical characteristics of both the sample A and B are listed in Table 3.1. The  $\Delta\phi$  and  $\Delta\omega$  values of the sample A are degraded compared to those of the sample B. Also, the  $T_{c,zero}$  value of 90.3 K for the sample A is lower than that of 91.8 K for the sample B.

The FE-SEM plan-view micrographs of both sample A and B are shown in Fig. 3.2. It is obvious that the morphology of top surface for the sample B is found to be relatively smooth compared with the sample A as shown in Fig. 3.2. We can observe that a lot of outgrowths are formed on the top surface for the sample A. In order to identify the outgrowth, we analyzed it by elemental mapping with the STEM-EDS analyses. As shown in Fig. 3.2(c), the outgrowth corresponds to the  $\text{CuO}$  phase and Gd123 matrix. The extra  $\text{CuO}$  phases were formed on the top surface for the sample A. As we mentioned, the in-plane and out-of-plane textures of sample A were more degraded than that of sample B. The outgrowth on the surface of sample A might be responsible for the degradation of texture quality.

Fig. 3.3 shows field orientation dependence of  $J_c$  for both the sample A and B. The  $J_c$  peak for  $B//c$  was observable in the sample A while that was unobservable in the sample B at 77 K in 1 T. However, the  $J_c$  peak for  $B//c$  disappeared in the sample A with increasing magnetic fields up to 5 T at 77 K. While the GdBCO films with BaSnO<sub>3</sub> nanorods clearly showed the  $J_c$  peak for  $B//c$  up to 5 T at 77 K [22], the  $c$ -axis peak was unobservable in the sample A above 3 T, indicating that the  $c$ -axis correlated pinning mechanism in the sample A was quite different. Also, the sample A exhibited the  $J_c$  degradation for  $B//ab$ . It is well-known that the  $J_c$  peak for  $B//ab$  is responsible for the intrinsic pinning and planar defects [23]. Furthermore, we observed small  $J_c$  peaks for  $B//c$  at 65 K in 3 and 5 T even though  $J_c$  peak for  $B//c$  in the sample B was unobservable at 77 K.

As shown in Fig. 3.4, the threading dislocations along the  $c$ -axis are observable in both the sample A and B. Nie *et al.* [24] reported that the  $J_c$  peak for  $B//c$  at 60 K was responsible for the egg-shaped precipitates and threading dislocations which were aligned along the  $c$ -axis. Even though the precipitates were unobservable in both sample A and B, we observed that the threading dislocations were aligned along the  $c$ -axis direction. Therefore, we considered that a small  $J_c$  peak for  $B//c$  at 65 K in 3 and 5 T were attributed to the threading dislocations for both the sample A and B. However, the origin of  $J_c$  peak for  $B//c$  in the sample A at 77 K in 1 T was not attributable to the threading dislocation due to the absence of  $J_c$  peak for  $B//c$  in the sample B at 77 K in 1 T.

According to previous reports [19, 20], the  $J_c$  peak for  $B//c$  was responsible for the twin boundaries. However, we considered that the  $J_c$  peak for  $B//c$  at 77

K in 1 T might be responsible for the another defects not twin boundaries for the sample A. As shown in Fig. 3.5, we also observe the TBs for both the sample A and B. We only observed the  $J_c$  peak for  $B//c$  in the sample A at 77 K in 1 T. Armenio *et al.* [21] argued that the  $J_c$  peak for  $B//c$  at 77 K in 5 T was attributable to the twin boundaries. Also, the  $J_c$  peak for  $B//c$  at 77 K above 5 T was reported [20, 25]. The apperence of  $J_c$  peak for  $B//c$  is quite different depending on the measurement conditions, indicating that the defect operating  $c$ -axis correlated pinnign center in this study was different to that in previous reports. We agree that the twin boundaries might be responsible for the  $J_c$  peak for  $B//c$  in high magnetic fields. However, the  $J_c$  peak for  $B//c$  at 77 K in 1 T was unobservable in the sample B which possessed twin boudnaries in the superconducting matrix. Thus, we considered the twin boundaries were not the main reason for the  $J_c$  peak for  $B//c$  at 77 K in 1 T.

To further investigate microstructure of both the sample A and B, we performed the HR-STEM analysis. As shown in Fig. 3.6(a), a lot of SFs are observed in the sample A compared with the sample B. The SFs density of sample A is higher than that of sample B. Also, the SFs length of sample A is much smaller than that of sample B. In the previous reports, the SFs could improve not only the  $J_c$  values for  $B//ab$  [23, 27-29] but also the  $J_c$  values for  $B//c$  [30-33]. The SFs can be formed by the addition of an extra CuO layer, resulting in an edge dislocation at the boundary of SFs. Wang *et al.* [32] suggest that the terminating points of the SFs can introduce additional defects acting as effective pinning centers, leading to the enhancement of in-field  $J_c$  for  $B//c$ . Also, Takahashi *et al* [30] suggested that much higher SFs and screw dislocations in undoped GdBCO films could act as  $c$ -axis correlated pinning

centers at 77 K in 1 T. As shown in Fig. 3.6(b) and (d), the edge dislocation of the sample A is more than that of the sample B. The schematic of the short SFs operating the  $c$ -axis correlated pinning centers is presented in Fig. 3.7. When the magnetic fields are parallel to  $c$ -axis direction, the flux lines can be pinned at the boundaries of short SFs due to the edge dislocation, leading to the  $J_c$  peak for  $B//c$  at 77 K in 1 T.

### 3.4. Summary

The GdBCO films were successfully fabricated by the PLD process on the CeO<sub>2</sub>-buffered MgO (100) single crystal substrate. By modifying the position of focal point in the PLD system, we fabricated the GdBCO films having the  $J_c$  peak for  $B//c$  and tried to identify the origin of the  $J_c$  peak for  $B//c$ . From the angular dependence of  $J_c$ , the sample A showed the  $J_c$  peak for  $B//c$  at 77 K in 1 T while the  $J_c$  peak for  $B//c$  was unobservable in the sample B. In the cross-sectional STEM micrographs, we observed the threading dislocation and twin boundaries in both the sample A and B, leading to the appearance of the small  $J_c$  peak for  $B//c$  at 65 K in 3 and 5 T. Interestingly, the short SFs were observable in sample A unlike the sample B. The short SFs dispersed in the matrix caused the numerous edge dislocation at the boundary of SFs, leading to the  $J_c$  peak for  $B//c$  at 77 K in 1 T. Consequently, the origin of  $J_c$  peak for  $B//c$  was different depending on the conditions such as a temperature and intensity of magnetic field.

## References

- [1] S. Foltyn, L. Civale, J. MacManus-Driscoll, Q. Jia, B. Maiorov, H. Wang, and M. Maley, "Materials science challenges for high-temperature superconducting wire," *Nature materials*, vol. 6, no. 9, p. 631, 2007.
- [2] M. Daeumling, J. Seuntjens, and D. Larbalestier, "Oxygen-defect flux pinning, anomalous magnetization and intra-grain granularity in  $\text{YBa}_2\text{Cu}_3\text{O}_{7-\delta}$ ," *Nature*, vol. 346, no. 6282, p. 332, 1990.
- [3] T. Hylton and M. Beasley, "Flux-pinning mechanisms in thin films of  $\text{YBa}_2\text{Cu}_3\text{O}_x$ ," *Physical Review B*, vol. 41, no. 16, p. 11669, 1990.
- [4] V. Maroni, Y. Li, D. Feldmann, and Q. Jia, "Correlation between cation disorder and flux pinning in the  $\text{YBa}_2\text{Cu}_3\text{O}_7$  coated conductor," *Journal of Applied Physics*, vol. 102, no. 11, p. 113909, 2007.
- [5] R. Schalk, K. Kundzins, H. Weber, E. Stangl, S. Proyer, and D. Bäuerle, "STM observation of dislocation chains suitable for flux pinning in  $\text{YBa}_2\text{Cu}_3\text{O}_{7-x}$  films," *Physica C: Superconductivity and its applications*, vol. 257, no. 3-4, pp. 341-354, 1996.
- [6] B. Dam, J. Huijbregtse, F. Klaassen, R. Van der Geest, G. Doornbos, J. Rector, A. Testa, S. Freisem, J. Martinez, and B. Stäuble-Pümpin, "Origin of high critical currents in  $\text{YBa}_2\text{Cu}_3\text{O}_{7-\delta}$  superconducting thin films," *Nature*, vol. 399, no. 6735, p. 439, 1999.
- [7] F. Klaassen, G. Doornbos, J. Huijbregtse, R. Van der Geest, B. Dam, and R. Griessen, "Vortex pinning by natural linear defects in thin films of  $\text{YBa}_2\text{Cu}_3\text{O}_{7-\delta}$ ," *Physical Review B*, vol. 64, no. 18, p. 184523, 2001.
- [8] J. Huijbregtse, F. Klaassen, A. Szepielow, J. Rector, B. Dam, R. Griessen, B. Kooi, and J. T. M. De Hosson, "Vortex pinning by natural defects in thin films of  $\text{YBa}_2\text{Cu}_3\text{O}_{7-\delta}$ ," *Superconductor Science and Technology*, vol. 15, no. 3, p. 395, 2002.
- [9] V. Pan, Y. Cherpak, V. Komashko, S. Pozigun, C. Tretiatchenko, A.

- Semenov, E. Pashitskii, and A. V. Pan, "Supercurrent transport in  $\text{YBa}_2\text{Cu}_3\text{O}_{7-\delta}$  epitaxial thin films in a dc magnetic field," *Physical review B*, vol. 73, no. 5, p. 054508, 2006.
- [10] D. Agassi, D. Christen, and S. Pennycook, "Flux pinning and critical currents at low-angle grain boundaries in high-temperature superconductors," *Applied physics letters*, vol. 81, no. 15, pp. 2803-2805, 2002.
- [11] W. Kwok, U. Welp, G. Crabtree, K. Vandervoort, R. Hulscher, and J. Liu, "Direct observation of dissipative flux motion and pinning by twin boundaries in  $\text{YBa}_2\text{Cu}_3\text{O}_{7-\delta}$  single crystals," *Physical review letters*, vol. 64, no. 8, p. 966, 1990.
- [12] B. Roas, L. Schultz, and G. Saemann-Ischenko, "Anisotropy of the critical current density in epitaxial  $\text{YBa}_2\text{Cu}_3\text{O}_x$  films," *Physical review letters*, vol. 64, no. 4, p. 479, 1990.
- [13] C. Jooss, R. Warthmann, and H. Kronmüller, "Pinning mechanism of vortices at antiphase boundaries in  $\text{YBa}_2\text{Cu}_3\text{O}_{7-\delta}$ ," *Physical Review B*, vol. 61, no. 18, p. 12433, 2000.
- [14] M. Kramer, "Processing controlled stacking faults in  $\text{YBa}_2\text{Cu}_3\text{O}_{7-\delta}$  and their effect on flux pinning," *Applied physics letters*, vol. 58, no. 10, pp. 1086-1088, 1991.
- [15] Y. Jia, U. Welp, G. Crabtree, W. Kwok, A. Malozemoff, M. Rupich, S. Fleshler, and J. Clem, "Microstructure dependence of the c-axis critical current density in second-generation YBCO tapes," *Journal of Applied Physics*, vol. 110, no. 8, p. 083923, 2011.
- [16] E. Talantsev, N. Strickland, S. Wimbush, J. Storey, J. Tallon, and N. Long, "Hole doping dependence of critical current density in  $\text{YBa}_2\text{Cu}_3\text{O}_{7-\delta}$  conductors," *Applied Physics Letters*, vol. 104, no. 24, p. 242601, 2014.
- [17] A. Puichaud, S. Wimbush, and R. Knibbe, "Enhanced low-temperature critical current by reduction of stacking faults in REBCO coated

- conductors," *Superconductor Science and Technology*, vol. 30, no. 7, p. 074005, 2017.
- [18] K. Nakaoka, J. Matsuda, Y. Kitoh, T. Goto, Y. Yamada, T. Izumi, and Y. Shiohara, "Influence of starting solution composition on superconducting properties of YBCO coated conductors by advanced TFA-MOD process," *Physica C: Superconductivity and its applications*, vol. 463, pp. 519-522, 2007.
- [19] L. Civale, B. Maiorov, A. Serquis, J. Willis, J. Coulter, H. Wang, Q. Jia, P. Arendt, J. a. MacManus-Driscoll, and M. Maley, "Angular-dependent vortex pinning mechanisms in  $\text{YBa}_2\text{Cu}_3\text{O}_7$  coated conductors and thin films," *Applied Physics Letters*, vol. 84, no. 12, pp. 2121-2123, 2004.
- [20] V. Rouco, A. Palau, R. Guzman, J. Gazquez, M. Coll, X. Obradors, and T. Puig, "Role of twin boundaries on vortex pinning of CSD YBCO nanocomposites," *Superconductor Science and Technology*, vol. 27, no. 12, p. 125009, 2014.
- [21] A. A. Armenio, L. Piperno, G. De Marzi, V. Pinto, A. Mancini, F. Rizzo, A. Vannozzi, A. Rufoloni, A. Augieri, and R. B. Mos, "Stranger APCs: Study of Surface Decoration Material for YBCO Films," *IEEE Transactions on Applied Superconductivity*, vol. 29, no. 5, pp. 1-5, 2019.
- [22] K.-P. Ko, S.-M. Choi, J.-W. Lee, R.-K. Ko, S.-H. Moon, C. Park, and S.-I. Yoo, "Optimization of the  $\text{BaSnO}_3$  Doping Content in  $\text{GdBa}_2\text{Cu}_3\text{O}_{7-\delta}$  Coated Conductors by Pulsed Laser Deposition," *IEEE Transactions on Applied Superconductivity*, vol. 24, no. 6, pp. 1-8, 2014.
- [23] L. Civale, B. Maiorov, A. Serquis, S. Foltyn, Q. Jia, P. Arendt, H. Wang, J. Willis, J. Coulter, and T. Holesinger, "Influence of crystalline texture on vortex pinning near the ab-plane in  $\text{YBa}_2\text{Cu}_3\text{O}_7$  thin films and coated conductors," *Physica C: Superconductivity*, vol. 412, pp. 976-982, 2004.
- [24] J. Nie, H. Yamasaki, H. Yamada, Y. Nakagawa, K. Develos-Bagarinao,

- and Y. Mawatari, "Evidence for c-axis correlated vortex pinning in  $\text{YBa}_2\text{Cu}_3\text{O}_{7-\delta}$  films on sapphire buffered with an atomically flat  $\text{CeO}_2$  layer having a high density of nanodots," *Superconductor Science and Technology*, vol. 17, no. 7, p. 845, 2004.
- [25] T. Puig, J. Gutiérrez, A. Pomar, A. Llordés, J. Gazquez, S. Ricart, F. Sandiumenge, and X. Obradors, "Vortex pinning in chemical solution nanostructured YBCO films," *Superconductor Science and Technology*, vol. 21, no. 3, p. 034008, 2008.
- [26] R. Guzman, J. Gazquez, V. Rouco, A. Palau, C. Magen, M. Varela, J. Arbiol, X. Obradors, and T. Puig, "Strain-driven broken twin boundary coherence in  $\text{YBa}_2\text{Cu}_3\text{O}_{7-\delta}$  nanocomposite thin films," *Applied Physics Letters*, vol. 102, no. 8, p. 081906, 2013.
- [27] E. D. Specht, A. Goyal, J. Li, P. M. Martin, X. Li, and M. Rupich, "Stacking faults in  $\text{YBa}_2\text{Cu}_3\text{O}_{7-x}$ : Measurement using x-ray diffraction and effects on critical current," *Applied physics letters*, vol. 89, no. 16, p. 162510, 2006.
- [28] R. Goswami, T. Haugan, P. Barnes, G. Spanos, and R. Holtz, "Effects of nanoscale defects on critical current density of  $(\text{Y}_{1-x}\text{Eu}_x)\text{Ba}_2\text{Cu}_3\text{O}_{7-\delta}$  thin films," *Physica C: Superconductivity*, vol. 470, no. 5-6, pp. 318-322, 2010.
- [29] H. Yamasaki, K. Ohki, I. Yamaguchi, M. Sohma, W. Kondo, H. Matsui, T. Manabe, and T. Kumagai, "Strong flux pinning due to dislocations associated with stacking faults in  $\text{YBa}_2\text{Cu}_3\text{O}_{7-\delta}$  thin films prepared by fluorine-free metal organic deposition," *Superconductor Science and Technology*, vol. 23, no. 10, p. 105004, 2010.
- [30] K. Takahashi, Y. Yamada, M. Konishi, T. Watanabe, A. Ibi, T. Muroga, S. Miyata, Y. Shiohara, T. Kato, and T. Hirayama, "Magnetic field dependence of  $J_c$  for Gd-123 coated conductor on PLD- $\text{CeO}_2$  capped IBAD-GZO substrate tapes," *Superconductor Science and Technology*, vol. 18, no. 8, p. 1118, 2005.

- [31] Y. Yamada, K. Takahashi, H. Kobayashi, M. Konishi, T. Watanabe, A. Ibi, T. Muroga, S. Miyata, T. Kato, and T. Hirayama, "Epitaxial nanostructure and defects effective for pinning in Y(RE)Ba<sub>2</sub>Cu<sub>3</sub>O<sub>7-x</sub> coated conductors," *Applied Physics Letters*, vol. 87, no. 13, p. 132502, 2005.
- [32] J. Wang, J. Kwon, J. Yoon, H. Wang, T. Haugan, F. Baca, N. Pierce, and P. Barnes, "Flux pinning in YBa<sub>2</sub>Cu<sub>3</sub>O<sub>7-δ</sub> thin film samples linked to stacking fault density," *Applied Physics Letters*, vol. 92, no. 8, p. 082507, 2008.
- [33] J. Gazquez, M. Coll, N. Roma, F. Sandiumenge, T. Puig, and X. Obradors, "Structural defects in trifluoroacetate derived YBa<sub>2</sub>Cu<sub>3</sub>O<sub>7</sub> thin films," *Superconductor Science and Technology*, vol. 25, no. 6, p. 065009, 2012.

Table 3.1. The  $T_{c,zero}$ ,  $\phi$  scan of (103) reflection, and  $\omega$  scan of (005) reflection

	$T_{c,zero}$ (K)	$\phi$ scan of (103) reflection	$\omega$ scan of (005) reflection
Sample A	90.3	$2.20 \pm 0.02$	1.15
Sample B	91.8	$1.93 \pm 0.02$	0.89

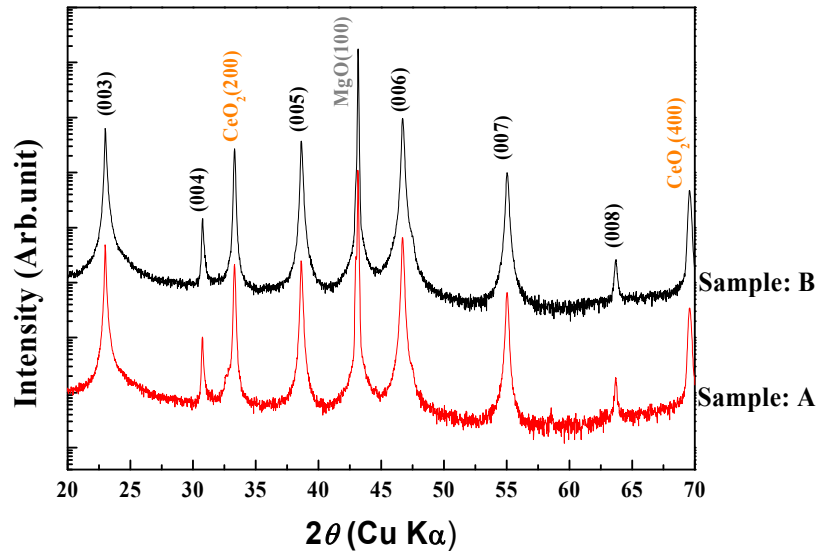


Fig. 3.1. XRD patterns of the GdBCO films (sample A (red) and sample B(black)).

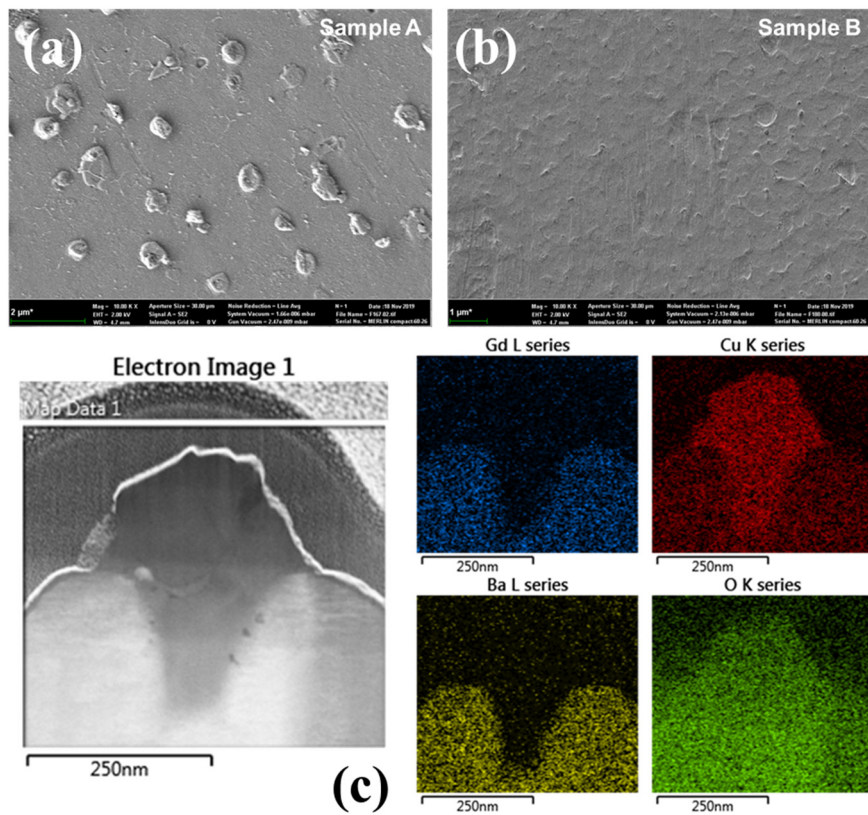


Fig. 3.2. FE-SEM micrographs of (a) sample A and sample B. (c) Z-contrast images of the outgrowth for the top surface of sample A, and the Gd, Ba, Cu, and O spectral images.

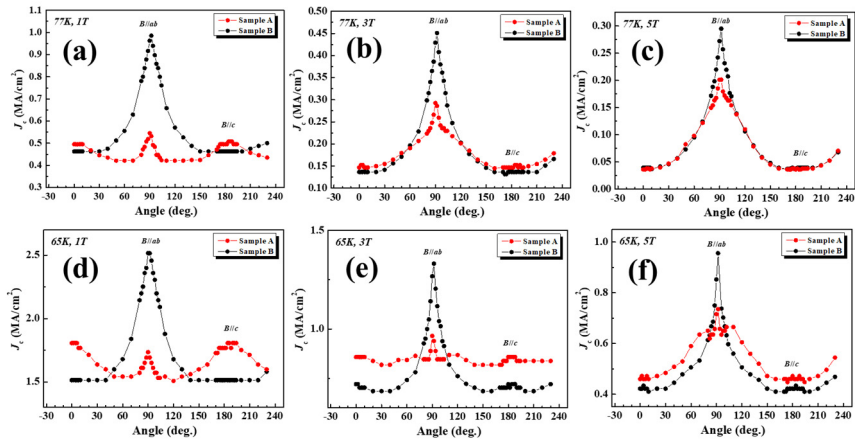


Fig. 3.3. Angular dependence of  $J_c$  at 77 K in (a) 1 T, (b) 3 T, and (c) 5 T, and at 65 K in (d) 1 T, (e) 3 T, and (f) 5 T for both the sample A and B.

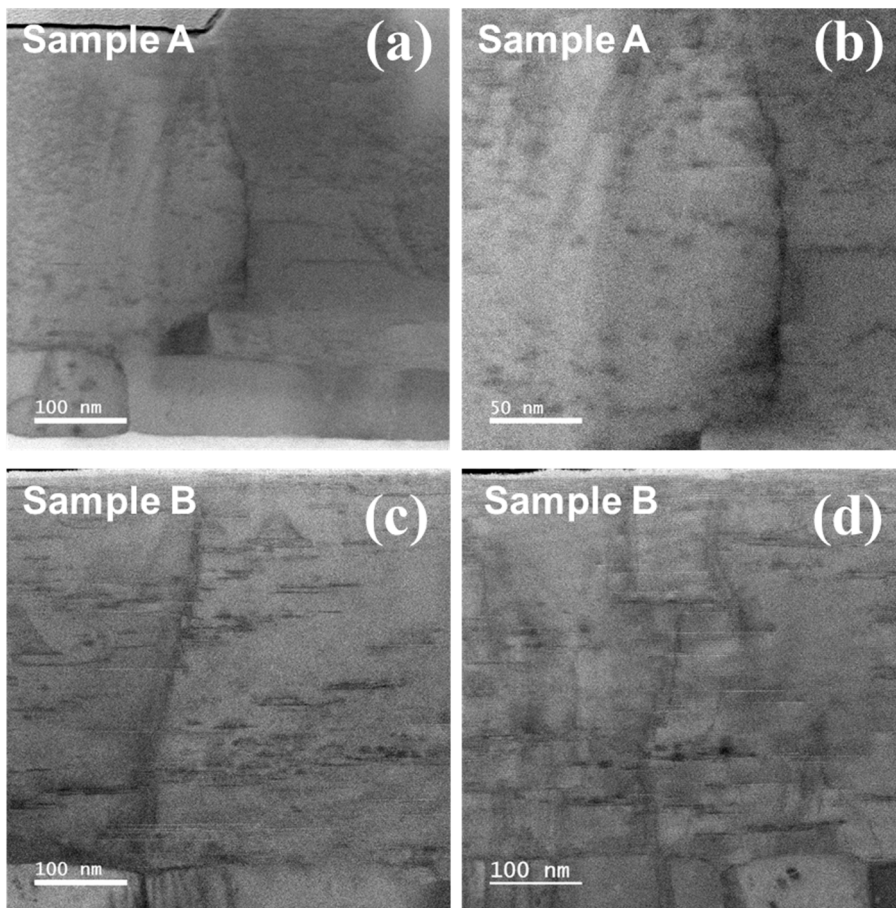


Fig. 3.4. Cross-sectional STEM micrographs of both the sample A and sample B.

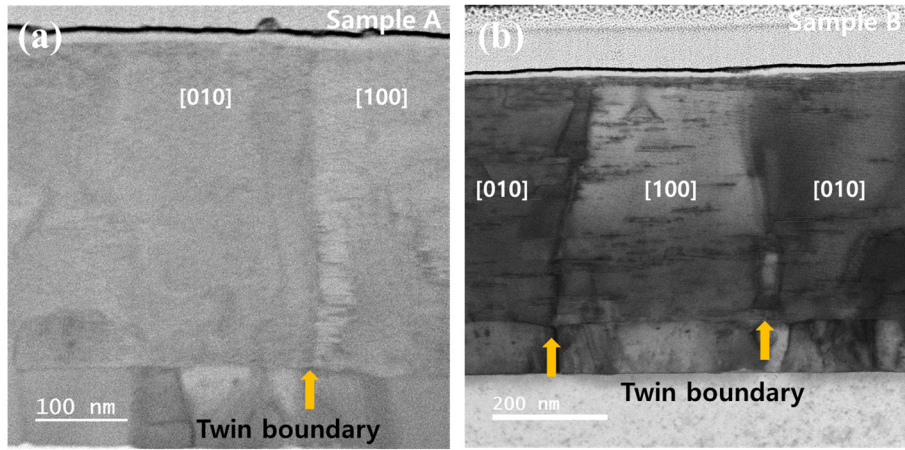


Fig. 3.5. Cross-sectional BF STEM micrographs of both the sample A (a) and B (b).

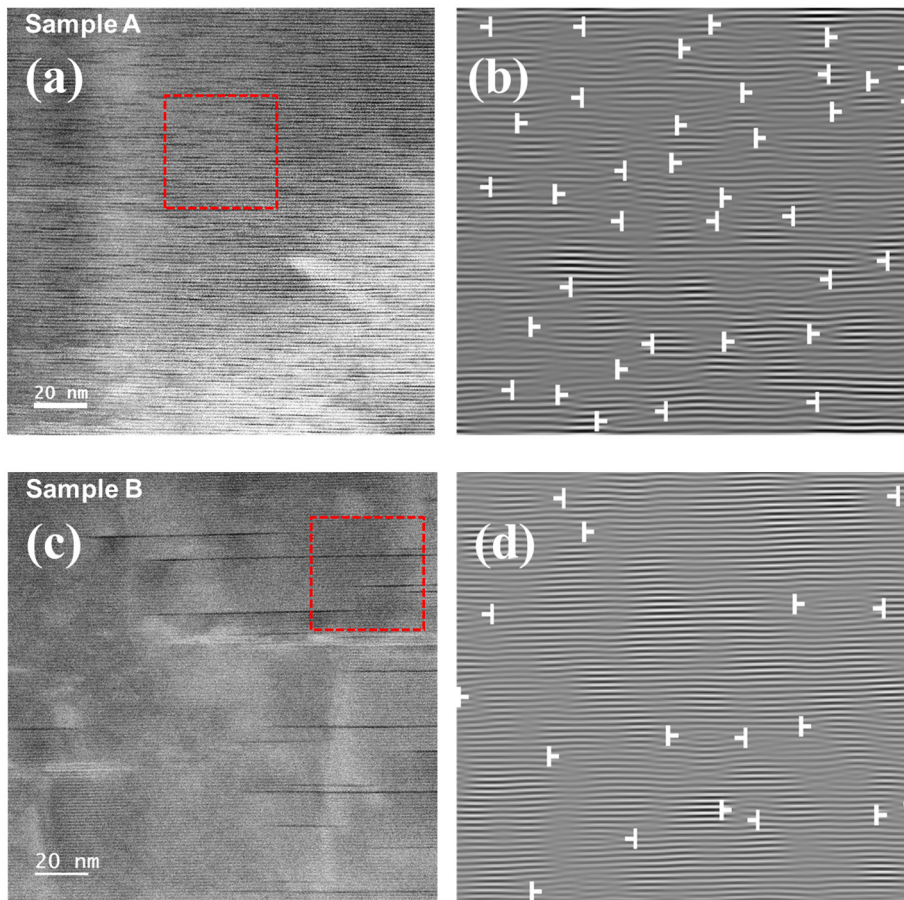


Fig. 3.6. HAADF STEM images of the sample A (a) and sample B (c), and reconstructed masked inverse FFT images for the sample A (b) and sample B (d) analyzed for the square area related by red dashed line in (a) and (c).

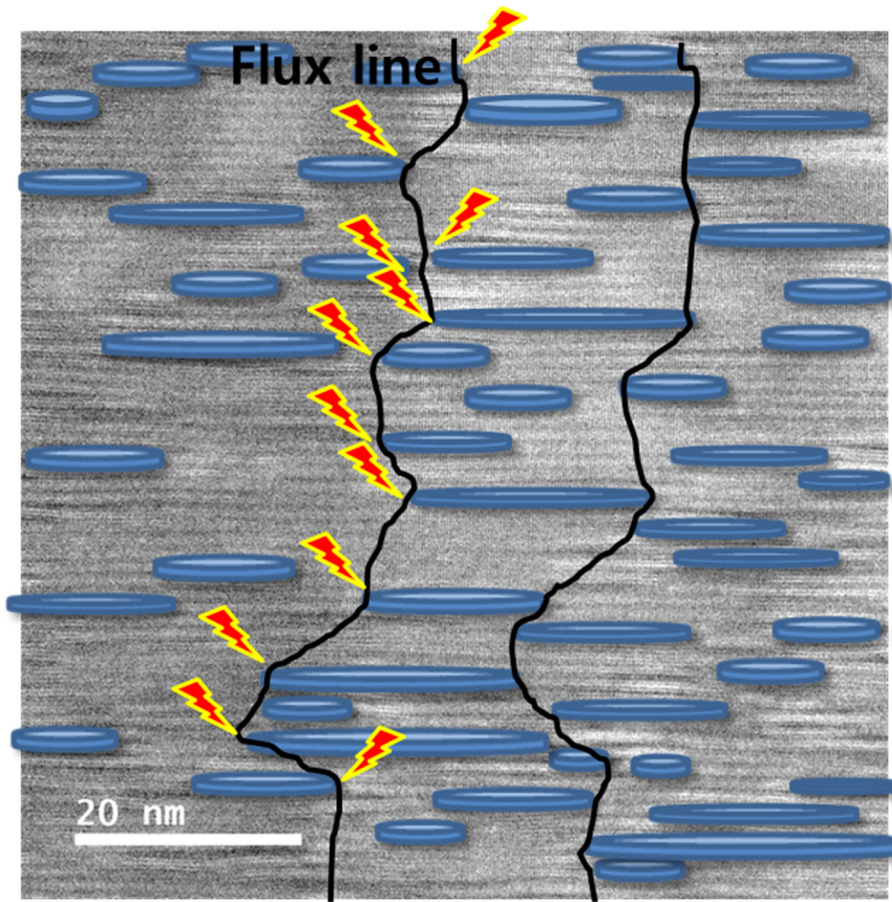


Fig. 3.7. Schematic of the pinning model for the stacking faults acting as the *c*-axis related pinning center.

# **Chapter 4. Effect of post-annealing on the pinning properties of GdBCO CCs by the RCE-DR process**

## **4.1. Introduction**

REBCO CCs are very promising for electric power applications such as cables, transformers, fault current limiters, and high field magnets due to their high current carrying capacity [1]. So far, REBCO CCs have been developed by various technologies such as PLD, MOD, MOCVD, and RCE-DR [2-6]. Among REBCO CCs fabricated by many manufacturers, the GdBCO CCs by the RCE-DR process have attracted attention of many researchers due to high  $J_c$  value ( $> 4 \text{ MA/cm}^2$ ) at 77 K in self-field in addition to the strong technological advantages of high throughput and high yield [6]. However, the pinning properties of GdBCO CCs should be improved since the in-field  $J_c$  values of GdBCO CCs are inferior to those of REBCO CCs fabricated by other manufacturing technologies [7].

Up to now, we have tried many efforts to enhance the in-field  $J_c$  values of the GdBCO CCs via RCE-DR. Such efforts include the controlling the growth temperature [8], varying initial compositions [9], adding the another RE element [10], applying the post-annealing process [11], and proton irradiation [12]. Particularly, when RCE-DR-processed GdBCO CCs were annealed at 750 in in the  $PO_2$  of 300 mTorr for 5 min, the minimum  $J_c$  values were significantly

improved with increasing applied fields at 77 and 65 K due to lowered SF density compared with the pristine sample [11].

Similarly, Specht *et al.* [13] reported that the YBCO films fabricated by the MOD process exhibited a reduced SF density after post-annealing at 750°C in the 500 ppms O<sub>2</sub> atmosphere, leading to suppressed  $J_c^{ab}$  values at 77 K in 1 T. Also, Puichaud *et al.* [14] reported that the YBCO CCs which were annealed at various temperatures in flowing oxygen showed different SF density. With increasing the annealing temperature, the SF density of the YBCO CCs increased, resulting in the improved  $J_c^{ab}$  value at 77 K in 1 T.

The  $J_c$  peak for  $B//ab$  at 77 K in 1 T is reported to have a close relationship with the SF density [14, 15]. However, the relationship between the SF density and  $J_{c,min}$  value in high fields has never been clarified yet. To fully investigate the effect of post-annealing on the pinning properties of GdBCO CCs, in this study, we extended the annealing condition down to 450 °C in the  $PO_2$  of 300 mTorr. Contrary to our previous study [11] on GdBCO CCs post-annealed at 750 °C, exhibiting a reduced SF density, the samples annealed at the temperature region of 450-600 °C for 1 h included not only an increased SF density but also the Gd124 phase in the GdBCO matrix, leading to significantly different pinning properties.

## 4.2. Experimental

The GdBCO CCs used in this study were fabricated by SuNAM Co. in Korea. The GdBCO layer was grown on LaMnO<sub>3</sub> (LMO)-buffered IBAD MgO template using the RCE-DR process. The architecture of GdBCO CCs is the

following multi-layer structure: GdBCO/LMO/epi-MgO/IBAD MgO/Y<sub>2</sub>O<sub>3</sub>/Al<sub>2</sub>O<sub>3</sub>/SUS201. For the fabrication of the GdBCO CC, we transferred amor-phous precursor film with the cation ratio of Gd:Ba:Cu≈1:1:2.5 from lower  $PO_2$  zone of  $\sim 10^{-5}$  Torr to higher  $PO_2$  zone of  $\sim 150$  mTorr and passed this zone for 2 min to grow  $\sim 1.5$   $\mu\text{m}$ -thick GdBCO layer in a reel-to-reel furnace at 860°C as described in our previous papers [4], [5]. Detailed growth conditions for the GdBCO CCs are described in our previous report [6]. Short samples with the dimension of 10 mm length  $\times$  6 mm width were cut from long-length GdBCO CCs and post-annealed in a reel-to-reel furnace. The pristine GdBCO CCs by the RCE-DR process were post-annealed at 750°C in the  $PO_2$  of 300 mTorr for 5 ~ 60 min and in the  $PO_2$  of 10, 30, 300 and 1000 mTorr for 15 min. Also, in a reduced oxygen pressure ( $PO_2$  of 300 mTorr), as-grown samples were annealed at the temperatures ranging from 450 to 650°C for 1 h and at 750°C for 5 min. Among various GdBCO CCs samples, as-prepared sample (sample A), the sample annealed at 750 °C in the  $PO_2$  of 300 mTorr for 5 min (sample B), and the sample annealed at 500 °C in the  $PO_2$  of 300 mTorr for 1 h (sample C) were selected to characterize their microstructures and angular dependence of  $J_c$ . After post-annealing, both pristine and post-annealed samples were oxygenated at 500°C for 1 h in pure oxygen gas atmosphere.

To analyze the phase and crystallinity, X-ray diffraction (XRD) was performed on both the pristine and post-annealed GdBCO CCs with X-ray diffractometer (Bruker, D8-advance) with Cu- $K\alpha$  radiation. Transmission electron microscopy (TEM) (JEOL, JEM-2100F) and scanning transmission electron microscopy (STEM) (JEOL, ARM-200F) were employed for the

microstructural analyses of samples. TEM specimens were prepared by focused ion beam (FIB) (FEI, Helios 650). The critical temperature ( $T_c$ ) was measured with a standard four-point probe measurement system. The angular dependency  $J_c$  values of samples were measured using the physical property measurement system (PPMS) (Quantum Design, model-6000) at 50, 65, and 77 K after patterning a micro-bridge.

### 4.3. Results and discussion

#### 4.3.1. High temperature annealing in low $PO_2$ region

Angular dependency of in-field  $J_c$  values for GdBCO CC samples before and after the post-annealing process were measured at 77 K in 1, 5 T, and 65 K in 3, 7 T. The results are shown in Fig. 4.1. It is obvious that angular dependency of  $J_c$  for the pristine sample is quite different from those for the samples annealed at 750°C in the  $PO_2$  of 300 mTorr for 5, 15, and 30 min. The  $J_c$  peak near  $B//ab$  is known to be related to the intrinsic pinning associated with the layered structure of REBCO and also to the extended planar defects such as the SFs [15]. The  $J_c$  peaks of post-annealed samples for  $B//ab$  are significantly degraded at 77 K in 1 T while the  $J_c$  values of the samples annealed for 15 min are improved for  $B//c$  in comparison with those of the pristine sample.

Although the in-field  $J_c$  values of the sample annealed for 15 min are improved for  $B//c$ , the  $J_c$  enhancement at 77 K in 1 T is relatively smaller compared with that in our previous study [16]. This difference is attributable to a difference in the quality of GdBCO CCs fabricated by the RCE-DR process.

Compared with previous pristine sample of GdBCO CC by RCE-DR, the present pristine sample possesses higher  $T_{c,zero}$  and in-field  $J_c$  values, which will be described later. However, we can observe that the minimum  $J_c$  values of post-annealed samples are gradually increased with increasing the magnetic fields at 77 and 65 K. Especially, the minimum  $J_c$  values for post-annealed samples are improved in the relatively high field region even though the minimum  $J_c$  values of post-annealed samples are still lower than those of the pristine sample at 77 K, 1 T and 65 K, 3 T.

In order to observe the difference in the microstructures of samples before and after the post-annealing, we performed TEM analysis on the pristine sample and post-annealed samples at 750°C in the  $PO_2$  of 300 mTorr for 15 min, and the micrographs are shown in Fig. 4.2. The SFs are observed as clear straight lines in this figure because they are well known as the intergrowths of extra CuO plane parallel to ab-plane of GdBCO. However, it can also be observed that the density of SFs is significantly decreased after the post-annealing process. The average linear density of SF was characterized by analyzing the number of SF on three different cross-sectional TEM images (526 x 526 nm<sup>2</sup>) of each sample, including the micrographs shown in Fig. 4.2. The linear SF density was obtained by dividing the number of SFs existing in the view plane by the length of an arbitral line perpendicular to the straight lines of SFs. Their values are listed in table I. As shown in table I, the average SF density is about twice higher in the pristine sample. This abrupt decrease of the SF density in the sample annealed for 15 min is considered to be responsible for a severe reduction in in-field  $J_c$  for  $B//ab$  at 77 K. Accordingly, it can be seen that the effect of the SFs on the in-field  $J_c$  peak for  $B//ab$  is more dominant than that of

the intrinsic pinning of layered structure. This result is in good agreement with previous study [15].

Besides the TEM analysis, the difference in the SF density could also be identified by XRD analysis. E. D. Specht *et al.* [17] suggested that  $\text{YBa}_2\text{Cu}_4\text{O}_8$  (Y124)-type SFs in the YBCO matrix made the peak broadening of (003) reflection peak in the XRD patterns. We also found the peak broadening of (003) reflection in the pristine sample as shown in Fig. 4.3(a), and evaluated it by analyzing the full-width at half maximum (FWHM) values of (003) reflections as written in table 4.1. From this table, one can see that the FWHM values of post-annealed samples are lower than those of pristine, indicating that the SF density of the pristine sample is higher than those of the post-annealed samples, which also matches with the TEM analysis results of the average SF density.

As shown in Fig. 4.4, the SFs are piled up along the  $c$ -axis in the GdBCO CCs annealed at  $750^\circ\text{C}$  in the  $\text{PO}_2$  of 300 mTorr for 15 min, indicating that the piled-up streaks composed of the SFs are responsible for the enhancement of in-field  $J_c$  for  $B//c$ . In the previous study, the SFs are reported to improve not only the pinning properties for  $B//ab$  [15, 17-19] but also the  $J_c$  values for  $B//c$  [20-23] due to a strain effect around the boundary of SFs. J. Wang *et al.* [22] suggest that the terminating points of the SFs can introduce additional defects acting as effective pinning centers, leading to the enhancement of in-field  $J_c$  for  $B//c$ . According to the reports from Obradors group [23, 24], for the standard YBCO film by MOD, it is reported that the SFs break the coherence of twin boundary (TB) along the  $c$ -axis, and hence a decrease in the  $J_c (B//c)$  peak is observed in agreement with an increase in the  $J_c (B//ab)$  peak. However, similar to YBCO-BZO nanocomposites in ref. [24], our GdBCO films also include a

lot of  $\text{Gd}_2\text{O}_3$  particles within the GdBCO matrix [6, 25, 26]. Like very small, since the TB effect on  $J_c$  ( $B//c$ ) is negligibly small for YBCO-BZO nanocomposites [24] due to the broken coherence of TB by BZO nanoparticles, it is believed to be negligibly small for all our samples. In addition, in ref. [17], with the post-annealing conditions of  $750^\circ\text{C}$ ,  $PO_2$  of 500 ppm ( $\sim 380$  mTorr), very similar to our annealing condition, the standard MOD-YBCO film also showed negligibly small  $J_c$  ( $B//c$ ) peaks at 77 K in 1 T after post-annealing, supporting that the TB contribution may be very small if any.

Although the SF density is reduced by post-annealing, the  $J_c$  ( $B//c$ ) peaks of annealed samples are similar to that of pristine except the sample annealed for 15 min as shown in Fig. 4.1. Therefore, the enhanced  $J_c$  ( $B//c$ ) peak of the sample annealed for 15 min is surely attributable to the piled-up SFs rather than TB.

In order to investigate the  $PO_2$  effect during the post-annealing process, the GdBCO CCs were annealed at the  $750^\circ\text{C}$  in the  $PO_2$  of 10, 30, and 300 mTorr for 15 min. As shown in Fig. 4.5, the in-field  $J_c$  values of samples annealed in the  $PO_2$  of 10 and 30 mTorr are higher than those of the sample annealed in the  $PO_2$  of 300 mTorr for  $B//ab$ , indicating that the SF density is higher in the  $PO_2$  of 10 and 30 mTorr than 300 mTorr. Also, the peak broadening of (003) reflection in the  $PO_2$  of 10 and 30 mTorr is larger than that in the  $PO_2$  of 300 mTorr as shown in Fig. 4.3(b). Thus, the SFs are considered to be more effectively reduced by the post-annealing in the higher  $PO_2$  region ( $\geq 300$  mTorr).

There are only a few papers [16, 17, 27] reporting the effect of post-annealing on the SF density. Interestingly, compared with the results from E. F.

Talantsev *et al.* [27], although our post-annealing conditions for GdBCO are quite different from their conditions ( $PO_2$  of 1 ~ 760 Torr, 400°C) for MOD-YBCO, it is in good agreement that the SF density is increased with decreasing the oxygen partial pressure.

As shown in table 4.1, post-annealed samples exhibit depressed  $T_{c,zero}$  values and larger transition width ( $\Delta T_c$ ). This phenomena of reduced  $T_{c,zero}$  and increased  $\Delta T_c$  values by post-annealing were also observable in our previous study [16]. To clarify the sample quality, we also listed the magnetic  $J_c$  values of samples which were evaluated using a modified Bean model [28] from the loop widths of field-dependent magnetization hysteresis loops measured by an MPMS SQUID magnetometer. As we previously mentioned, the present GdBCO CCs fabricated by the RCE-DR process have higher  $T_{c,zero}$  value of 94.2 K compared with that of 89.9 K in our previous study [16], indicating that present GdBCO CCs are considered to have the  $Gd_{1+x}Ba_{2-x}Cu_3O_{7-\delta}$ -type solid solutions with lower  $x$  value compared with the pristine sample in our previous study since the  $T_{c,zero}$  value is sensitive to the  $x$  value [29, 30]. While the  $T_{c,zero}$  increase from 89.9 K to 93.7 K was obtainable from the sample after for 5 min at 800°C in 300 mTorr in our previous study [16], the  $T_{c,zero}$  values gradually decrease after post-annealing, which might cause less significant enhancement of the pinning properties in the present study.

#### 4.3.2. Low temperature annealing in low $PO_2$ region

The XRD patterns of both the pristine and post-annealed GdBCO CCs are shown in Fig. 4.6. As shown in Fig. 4.6(a), one can observe the (00 $l$ ) reflections

for all samples, indicating that both the pristine and post-annealed samples are highly *c*-axis oriented. In addition to the substrate peaks of MgO and Ni (of hastelloy), the second phases such as Gd<sub>2</sub>O<sub>3</sub> and CuO are also observable for all GdBCO CC samples. Since the growth mechanism of GdBCO film fabricated by the RCE-DR process is known to follow a melt-growth process based on the pseudobinary peritectic recombination of Gd<sub>2</sub>O<sub>3</sub> + liquid → GdBCO [6], the CuO phase is considered to be formed by the solidification of the CuO-rich liquid phase. Interestingly, unlike the pristine sample, samples post-annealed at the temperatures ranging from 450 to 600 °C in the *PO*<sub>2</sub> of 300 mTorr for 1 h exhibit the (00*l*) reflections of the Gd124 phase. As shown in Fig. 4.7(a), although the SFs are randomly distributed in the GdBCO matrix of the pristine sample, the Gd124 phase peak is undetectable for the pristine sample. Another interesting point is that, in comparison with the samples post-annealed at the temperatures ranging from 450 to 600 °C in the *PO*<sub>2</sub> of 300 mTorr for 1 h, the peak width of the (003) reflection for the samples post-annealed at 650 °C (1 h) and 750 °C (5 min) in the *PO*<sub>2</sub> of 300 mTorr is narrower than that for the pristine sample as shown in Fig. 4.7(b). This clearly indicates that the SF density is significantly reduced after post-annealing at 650 and 750 °C. Like other previous reports on YBCO and REBCO films by MOD [13, 14, 31, 32], the XRD peak broadening of the (003) reflection for the pristine GdBCO CC by RCE-DR was attributable to high SF density within the Gd123 matrix in our previous study [11].

Fig. 4.7 shows the cross-sectional TEM images of both the pristine and post-annealed GdBCO CC samples. It is obvious that the SFs, observable as the dark streaks, are randomly distributed in the Gd123 matrix for all samples. Also,

the round-shaped  $\text{Gd}_2\text{O}_3$  particles are observable in all samples, which is in good agreement with the XRD data in Fig. 4.7(a). The SFs are shown along the dashed white lines in Fig. 4.7. The average linear density of SFs was calculated by counting the number of SFs with three different cross-sectional TEM images ( $526 \times 526 \text{ nm}^2$ ). We represent the average linear density of SFs,  $T_c$ ,  $\Delta T$ , and FWHM of (003) reflection in table 4.2. As shown in table 4.2, the linear SF density of sample B is lower than those of both samples A and C, which is in good agreement with the corresponding FWHM values of the (003) reflection in the XRD patterns of Fig. 4.6(b). According to previous study on YBCO films by Zhang *et al.* [33] the SFs can be arbitrarily formed by introducing extra CuO chain source into the Y123 matrix, where the Y123 films were buried into CuO powder and then post-annealed at 900 °C in high  $PO_2$  region of 700 atm  $O_2$ . In the case of GdBCO CCs fabricated by the RCE-DR process, the CuO phase is normally observed within the Gd123 matrix and also on the top surface of the GdBCO film [5]. For the sample C, we performed the STEM-EDS elemental mapping as shown in Fig. 4.8. In accordance with our previous reports [5, 10], the CuO phase, indicated by red arrows, is observed within the Gd123 matrix and also on the top surface of sample in this figure.

Actually, while the SFs are observable in all samples as shown in Fig. 4.7, the XRD peaks of Gd124 are detectable only for the GdBCO CCs post-annealed at the temperatures below 600 °C as shown in Fig. 4.6. In order to identify the location of the Gd124 phase within the GdBCO matrix, we performed the STEM analysis for the sample C as shown in Fig. 4.9. Fig. 4.9(a) and (c) are the magnified HAADF images which are indicated by the red and white rectangles in Fig. 4.8(a), respectively. As shown in Fig. 4.9(a) and (c), the

Gd124 phase can be observed near the top surface of the Gd123 matrix. The Gd124 phase is distinguishable from the Gd123 matrix, and the extra CuO chains in the Gd124 phase appear as a thick dark streak. While the dark streaks are randomly distributed for both pristine and post-annealed samples in Fig. 4.7, those of GdBCO CCs post-annealed at 500 °C in the  $PO_2$  of 300 mTorr for 1 h are formed sequentially near the top surface of films. The magnified HAADF images in Fig. 4.9(b) and (d) clearly reveal that the double CuO chains, which are indicated by red arrows, are arranged in a regular sequence along the  $c$ -axis.

For the sample C, the reason for the formation of the Gd124 phase near the top surface of GdBCO film can be easily understood if we consider that the CuO phase predominantly locates at the top surface of GdBCO film since the CuO phase can act as a reservoir to supply extra CuO chains. On the other hand, the double CuO chains can also be formed continuously near the CuO phase trapped in the Gd123 matrix, leading to a local formation of the Gd124 phase. Therefore, as shown in Fig. 4.10, we obtained high resolution HAADF images around the CuO phase trapped in the Gd123 matrix. It is obvious that the Gd124 phase can also be formed near the CuO phase within the GdBCO matrix for the sample C in Fig. 4.10(a) while the CuO double chains are not arranged continuously in figures Figs. 4.10(b)-(d).

To further investigate detailed microstructure of the Gd124 phase, we performed the high-magnification HAADF-STEM analysis on the sample C as shown in Fig. 4.11(a). These HAADF-STEM images reveal the position of atomic arrangements in this sample. As shown in Fig. 4.11(a), thicker dark streaks can be identified as the double CuO chains while thinner dark streaks can be identified as the single CuO chains as shown in Fig. 4.11(b). The lattice

positions of Gd, Ba, and Cu elements are indicated by red, blue, and orange circles, respectively. It is well known that the sequence of the Y124 phase is BaO-CuO<sub>2</sub>-Y-CuO<sub>2</sub>-BaO-CuO-CuO [34]. Since the sequence of the Gd124 unit cell must be identical to that of the YBa<sub>2</sub>Cu<sub>4</sub>O<sub>8</sub> (Y124) unit cell, having two adjacent CuO layers, the Gd124 unit cell has the sequence of BaO-CuO<sub>2</sub>-Gd-CuO<sub>2</sub>-BaO-CuO-CuO as shown in the inset of Fig. 4.11(a). Interestingly, regions with triple CuO chains, corresponding to Gd125, are observable in the sample C.

Zhang *et al.* [33] reported that Y124, Y<sub>2</sub>Ba<sub>4</sub>Cu<sub>7</sub>O<sub>15</sub> (Y247), YBa<sub>2</sub>Cu<sub>5</sub>O<sub>9</sub> (Y125), and YBa<sub>2</sub>Cu<sub>6</sub>O<sub>10</sub> (Y126) phases were observable in the YBCO films annealed in high oxygen pressure. Fu *et al.* [35] also reported the existence of the Y125 phase in the Y123 matrix, and argued that no shift of Ba atoms has occurred in the Y125 phase while Ba atoms shift along the direction of 1/2[010] in the Y124 phase. We can also observe the Gd125 phase in the matrix as shown in figure 6(a). The BaO layers, indicated by red arrows, are shifted along the direction of 1/2[010] at two adjacent CuO chains while those are not shifted but consistent along the direction of *c*-axis at three adjacent CuO chains. Zhang *et al.* [36] reported that the XRD peaks of the Y247 phase were undetectable in the XRD patterns of the Y123 films even though the Y247 phase was observable in the HAADF-STEM images. If one layer of double CuO chains were randomly introduced into the Gd123 unit cell, only a half unit cell of the Gd124 phase would occur in the pristine sample, and thus the Gd124 phase would be undetectable in the XRD patterns. The Gd124 phase might be detectable in the XRD pattern if the double CuO chains were more continuous along the *c*-axis.

The angular dependency of in-field  $J_c$  values was measured for all samples at 77, 65, and 50 K in the fields ranging from 1 to 13 T and plotted in Fig. 4.12. Here, it should be noted that the data curves at 77 K in 1 T, 5 T and at 65 K in 3 T, 7 T for samples A and B in figure 7 are very similar but not completely overlapped with those of our previous report [11]. The reason is that we sampled different parts of GdBCO CCs for this study because the micro-bridges of samples in our previous report [11] were deteriorated and thus inappropriate for further measurements in higher fields. As shown in figure 4.12, all samples show anisotropic  $J_c$  behavior due to the intrinsic pinning of layered structure of REBCO and extrinsic pinning caused by extended planar defects. Unlike other samples, the sample B shows less anisotropic  $J_c$  peaks when the field is applied parallel to the  $ab$  plane of GdBCO at 77 K in 1 T. The  $J_c$  peaks for  $B//ab$  of the sample B are significantly degraded at 77 K in 1 T. In comparison with the sample A, the minimum  $J_c$  value of the sample B was improved at 77 K in 5 T although the  $J_c$  value for  $B//ab$  was degraded at 77 K in 1 T. The  $J_c$  suppression for  $B//ab$  at 77 K in 1 T is strongly related to the SF density. There are many reports [13-15, 37, 38] on the relationship between extended planar defects, which are called SFs, and the in-field  $J_c$  peak at  $\theta = 90^\circ$ . We also reported that the SF density was sensitive to the  $J_c$  peak at  $\theta = 90^\circ$  ( $B//ab$ ) at 77 K in 1 T in our previous report [11]. As shown in Fig. 4.7 and table 4.2, the linear SF density value of the sample B was decreased from  $0.37 \times 10^6/\text{cm}$  to  $0.28 \times 10^6/\text{cm}$  compared with the sample A after post-annealing, resulting in a degraded  $J_c$  peak for  $B//ab$  at 77 K in 1 T as shown in Fig. 4.12(a). Similarly, Specht *et al.* [13] reported that the  $J_c$  peak for  $B//ab$  was significantly degraded with the annealing condition of 750 °C in 500 ppm O<sub>2</sub> due to the reduction in

SF density. Puichaud *et al.* [14] reported that the SF density was increased by the oxygen annealing temperature of 700 °C, leading to improved  $J_c$  peak for  $B//ab$  at 77 K in 1 T. Compared with previous report [14] on YBCO CCs with oxygen annealing temperature of 700 °C, our post-annealing temperatures above 650 °C induced relatively lower SF density. On the basis of Y123, Y247, and Y124 phase diagrams [39], one can see that the Y123 phase is stable at relatively high temperature in the  $PO_2$  of 300 mTorr while the Y124 phase is stable at relatively high temperature in the  $PO_2$  of 760 Torr. Since the  $PO_2$  region of this study is lower than that of Puichaud *et al.* [14], the Gd123 phase is stable at relatively high temperature and thus Gd124 can be decomposed into Gd123 and CuO phases.

On the other hand, the sample C shows enhanced  $J_c$  peaks for  $B//ab$  at 77 K in 1 T compared with the sample A. Although it was impossible to measure the  $J_c$  values for  $B//ab$  at 77 K in 1 T due to the current limit in the PPMS equipment, it is obvious that the  $J_c$  peak for  $B//ab$  of the sample C is higher than that of the pristine sample at 77 K in 5 T as shown in Fig. 4.12(b). Also, in Fig. 4.12(a), we can see that the  $J_{c,min}$  values of the sample C are slightly enhanced compared with those of the pristine sample at 77 K in 1 T. However, there is no significant difference in the  $J_{c,min}$  values of both samples A and C at 77 K in 5 T (Fig. 4.12(b)). This tendency of GdBCO CCs is observable below 77 K. At 65 K in 3 T (Fig. 4.12(c)), in-field  $J_c$  values of the sample A are decreased with increasing angle from  $\theta = 0^\circ$  to  $70^\circ$  while those of the sample C are less decreased. With further decreasing the measuring temperature to 50 K and increasing applied fields to 13 T, both the sample A and sample B show the plateau region of  $J_c$  values in Fig. 4.12(e) while the in-field  $J_c$  values of the

sample C are increased with increasing  $\theta$  to  $90^\circ$ . However, the  $J_{c,min}$  values of the sample C are decreased with increasing the applied magnetic field.

the GdBCO CCs annealed at  $500^\circ\text{C}$  in the  $PO_2$  of 300 mTorr for 1 h show improved  $J_c$  peaks for  $B//ab$  at 77 K in 1 T compared with the pristine sample. Even though we failed to measure  $J_c$  values for  $B//ab$  at 77 K in 1 T due to the current limit in the PPMS equipment, it was obvious that the  $J_c$  peak for  $B//ab$  of GdBCO CCs annealed at  $500^\circ\text{C}$  in the  $PO_2$  of 300 mTorr for 1 h was higher than that of the pristine sample at 77 K in 5 T. Also, the  $J_{c,min}$  values of GdBCO CCs annealed at  $500^\circ\text{C}$  in the  $PO_2$  of 300 mTorr for 1 h were slightly enhanced compared with those of the pristine sample at 77 K in 1 T. However, there was no significant difference in the minimum  $J_c$  values of both the pristine and the GdBCO CCs annealed at  $500^\circ\text{C}$  in the  $PO_2$  of 300 mTorr for 1 h at 77 K in 5 T.

This tendency of GdBCO CCs was observable below 77 K. At 65 K in 3 T, in-field  $J_c$  of the pristine sample decreased with increasing angle from  $\theta = 0^\circ$  to  $70^\circ$  while the GdBCO CCs annealed at  $500^\circ\text{C}$  in the  $PO_2$  of 300 mTorr for 1 h had less a  $J_c$  decrease. With decreasing the temperature to 50 K, both the pristine sample and GdBCO CCs annealed at  $750^\circ\text{C}$  in the  $PO_2$  of 300 mTorr for 5 min show the plateau region of  $J_c$  values while the in-field  $J_c$  of the GdBCO CCs annealed at  $500^\circ\text{C}$  in the  $PO_2$  of 300 mTorr for 1 h increase with increasing  $\theta$  to  $90^\circ$ . However, the  $J_{c,min}$  values of GdBCO CCs annealed at  $500^\circ\text{C}$  in the  $PO_2$  of 300 mTorr for 1 h are decreased with increasing the applied magnetic field.

The field dependency of the  $J_{c,min}$  values is shown in Fig. 4.13. We can observe that the  $J_{c,min}$  values of the sample B are increased with increasing the applied fields. Especially, a significant improvement in the  $J_{c,min}$  value is obtainable from the sample B at relatively lower temperatures (50 K) in high

magnetic field (13 T), indicating that the post-annealed GdBCO CCs which have lower SF density are effective for the improvement of the  $J_{c,min}$  values in high magnetic fields. It is highly probable that the GdBCO CCs with lower SF density would represent larger improvement of  $J_{c,min}$  at lower temperature ( $< 50$  K) in the higher magnetic fields ( $> 13$  T). On the other hand, the  $J_{c,min}$  values of the sample C decrease at relatively lower temperatures in high magnetic field. Actually, it is well known that the SFs act as the strong pinning centers for  $B//ab$  at 77 K at 1 T. However, present results show that  $J_{c,min}$  values of the GdBCO CCs with higher SF density are degraded with increasing magnetic fields. The reason is that, in high magnetic fields, the SF is believed to block the supercurrent path in the REBCO matrix rather than to play a role of flux pinning center since the vortex-vortex interaction is too strong to pin the vortex. Chen *et al.* [40] reported that naturally generated defects such as antiphase boundaries, SFs, and edge dislocations could act as the strong pinning centers at 77 K in the applied field below 4 T. However, above 4 T, they reported that the in-field  $J_c$  values of the sample with high defect density were lower compared with the sample with low defect density, indicating that these defects are ineffective for improving the pinning properties at high field regions. As shown in Fig. 4.13, the  $J_{c,min}$  values of the sample with low SF density (sample B) are improved at higher field region with decreasing the temperature since the thermal depinning becomes less at low temperature. Consequently, it is very important to control the SF density of GdBCO CC via RCE-DR for the optimization of its pinning properties.

### 4.3. Summary

We have systematically investigated the effect of post-annealing process on the superconducting properties of the GdBCO CCs grown by the RCE-DR process. By controlling annealing conditions such as temperature and annealing time in a reduced oxygen pressure, it was possible to control the SF density of the pristine GdBCO CCs. We annealed the pristine sample at 750°C in the  $PO_2$  of 300 mTorr for 5-60 min. Among the post-annealed samples, the GdBCO CCs annealed for 15 min show enhanced in-field  $J_c$  values for  $B//c$  due to the SFs piled up along the c-axis of GdBCO film although the enhancement is not so significant. Also, the  $J_{c,min}$  values of post-annealed samples were slightly improved with increasing magnetic fields due to the reduced SF density. With the post-annealing temperatures ranging from 450 to 600°C in the  $PO_2$  of 300 mTorr for 1 h, the Gd124 phase was detectable for post-annealed samples. However, the GdBCO CCs annealed at 650 °C for 1 h and 750°C for 5 min represent the reduced SF density. In the cross-sectional HAADF-STEM images, the Gd124 phases existed predominantly near the top surface of GdBCO CCs annealed at 500°C in the  $PO_2$  of 300 mTorr for 1 h due to the CuO phase segregated at the top surface of GdBCO CCs while the SFs are dispersed randomly in the Gd123 matrix. Compared with pristine sample, the  $J_{c,min}$  values of GdBCO CCs annealed at 750°C in the  $PO_2$  of 300 mTorr for 5 min were improved with increasing the applied fields and decreasing temperatures due to the reduction of SF density. The  $J_{c,min}$  values of GdBCO CCs annealed at 500°C in the  $PO_2$  of 300 mTorr for 1 h were slightly improved at high temperature in low magnetic fields while those are degraded at 50 K in 11, and 13 T. In

conclusion, the elimination of SFs in the RE123 matrix is effective for improving the  $J_{c,min}$  values at relatively low temperature in high magnetic fields while the  $J_{c,min}$  values can be enhanced by the formation of Gd124 phases in the RE123 matrix at relatively high temperature in low magnetic fields. In conclusion, the reduction of SF in the RE123 matrix is effective for improving the  $J_{c,min}$  values at relatively low temperature in high magnetic fields while the  $J_{c,min}$  values can be enhanced by both increment in the SF density and the formation of Gd124 phases in the RE123 matrix at relatively high temperature in low magnetic fields.

## References

- [1] D. Larbalestier, A. Gurevich, D. M. Feldmann, and A. Polyanskii, "High- $T_c$  superconducting materials for electric power applications," *Nature*, pp. 311-320, 2001.
- [2] H. Kutami, T. Hayashida, S. Hanyu, C. Tashita, M. Igarashi, H. Fuji, Y. Hanada, K. Kakimoto, Y. Iijima, and T. Saitoh, "Progress in research and development on long length coated conductors in Fujikura," *Physica C: Superconductivity*, vol. 469, no. 15-20, pp. 1290-1293, 2009.
- [3] M. W. Rupich, X. Li, C. Thieme, S. Sathyamurthy, S. Fleshler, D. Tucker, E. Thompson, J. Schreiber, J. Lynch, and D. Buczek, "Advances in second generation high temperature superconducting wire manufacturing and R&D at American Superconductor Corporation," *Superconductor Science and Technology*, vol. 23, no. 1, p. 014015, 2009.
- [4] V. Selvamanickam, Y. Chen, X. Xiong, Y. Y. Xie, M. Martchevski, A. Rar, Y. Qiao, R. M. Schmidt, A. Knoll, and K. P. Lenseth, "High performance 2G wires: From R&D to pilot-scale manufacturing," *IEEE transactions on applied superconductivity*, vol. 19, no. 3, pp. 3225-3230, 2009.
- [5] S.-M. Choi, J.-W. Lee, G.-H. Shin, J.-H. Lee, G.-W. Hong, S.-H. Moon, and S.-I. Yoo, "Characteristics of high  $J_c$  GdBCO coated conductors fabricated by the RCE-DR process," *IEEE Transactions on Applied Superconductivity*, vol. 23, no. 3, p. 8001004, 2013.
- [6] J.-H. Lee, H. Lee, J.-W. Lee, S.-M. Choi, S.-I. Yoo, and S.-H. Moon, "RCE-DR, a novel process for coated conductor fabrication with high performance," *Superconductor Science and Technology*, vol. 27, no. 4, p. 044018, 2014.

- [7] C. Senatore, C. Barth, M. Bonura, M. Kulich, and G. Mondonico, "Field and temperature scaling of the critical current density in commercial REBCO coated conductors," *Superconductor Science and Technology*, vol. 29, no. 1, p. 014002, 2015.
- [8] S.-M. Choi, J.-W. Lee, J.-H. Lee, S.-H. Moon, and S.-I. Yoo, "The Effect of Growth Temperature on  $\text{GdBa}_2\text{Cu}_3\text{O}_{7-d}$  Coated Conductors Fabricated by the RCE-DR Process," *IEEE Transactions on Applied Superconductivity*, vol. 25, no. 3, pp. 1-5, 2015.
- [9] J. MacManus-Driscoll, M. Bianchetti, A. Kursumovic, G. Kim, W. Jo, H. Wang, J. Lee, G. Hong, and S. Moon, "Strong pinning in very fast grown reactive co-evaporated  $\text{GdBa}_2\text{Cu}_3\text{O}_7$  coated conductors," *APL Materials*, vol. 2, no. 8, p. 086103, 2014.
- [10] W.-J. Oh, I. Park, K. Chung, Y. Lee, J. H. Lee, H. Lee, S.-H. Moon, and S.-I. Yoo, "Enhanced Pinning Properties of Sm-doped GdBCO CCs by the RCE-DR process," *IEEE Transactions on Applied Superconductivity*, vol. 29, p. 8002404, 2019.
- [11] W.-J. Oh, I. Park, J.-H. Lee, H. Lee, S.-H. Moon, K. Shinde, K. Chung, and S.-I. Yoo, "The Post-Annealing Effect on the Pinning Properties of  $\text{GdBa}_2\text{Cu}_3\text{O}_{7-\delta}$  Coated Conductors via RCE-DR," *IEEE Transactions on Applied Superconductivity*, vol. 28, no. 4, 2018.
- [12] N. Haberkorn, J. Kim, S. Suárez, J.-H. Lee, and S. Moon, "Influence of random point defects introduced by proton irradiation on the flux creep rates and magnetic field dependence of the critical current density  $J_c$  of co-evaporated  $\text{GdBa}_2\text{Cu}_3\text{O}_{7-\delta}$  coated conductors," *Superconductor Science and Technology*, vol. 28, no. 12, p. 125007, 2015.
- [13] E. D. Specht, A. Goyal, J. Li, P. M. Martin, X. Li, and M. Rupich, "Stacking faults in  $\text{YBa}_2\text{Cu}_3\text{O}_{7-x}$ : Measurement using x-ray diffraction and effects on critical current," *Applied physics letters*, vol. 89, no. 16, p. 162510, 2006.
- [14] A. Puichaud, S. Wimbush, and R. Knibbe, "Enhanced low-temperature

- critical current by reduction of stacking faults in REBCO coated conductors," *Superconductor Science and Technology*, vol. 30, no. 7, p. 074005, 2017.
- [15] L. Civale, B. Maiorov, A. Serquis, S. Foltyn, Q. Jia, P. Arendt, H. Wang, J. Willis, J. Coulter, and T. Holesinger, "Influence of crystalline texture on vortex pinning near the ab-plane in  $\text{YBa}_2\text{Cu}_3\text{O}_7$  thin films and coated conductors," *Physica C: Superconductivity*, vol. 412, pp. 976-982, 2004.
- [16] J.-W. Lee, S.-M. Choi, W.-J. Oh, J.-H. Lee, S.-H. Moon, and S.-I. Yoo, "Enhanced Pinning Properties of  $\text{GdBa}_2\text{Cu}_3\text{O}_{7-\delta}$  Coated Conductors via a Post-Annealing Process," *IEEE Transactions on Applied Superconductivity*, vol. 26, no. 3, pp. 1-6, 2016.
- [17] E. D. Specht, A. Goyal, J. Li, P. M. Martin, X. Li, and M. Rupich, "Stacking faults in  $\text{YBa}_2\text{Cu}_3\text{O}_{7-x}$ : Measurement using x-ray diffraction and effects on critical current," *Applied physics letters*, vol. 89, no. 16, p. 162510, 2006.
- [18] R. Goswami, T. Haugan, P. Barnes, G. Spanos, and R. Holtz, "Effects of nanoscale defects on critical current density of  $(\text{Y}_{1-x}\text{Eu}_x)\text{Ba}_2\text{Cu}_3\text{O}_{7-\delta}$  thin films," *Physica C: Superconductivity*, vol. 470, no. 5-6, pp. 318-322, 2010.
- [19] H. Yamasaki, K. Ohki, I. Yamaguchi, M. Sohma, W. Kondo, H. Matsui, T. Manabe, and T. Kumagai, "Strong flux pinning due to dislocations associated with stacking faults in  $\text{YBa}_2\text{Cu}_3\text{O}_{7-\delta}$  thin films prepared by fluorine-free metal organic deposition," *Superconductor Science and Technology*, vol. 23, no. 10, p. 105004, 2010.
- [20] K. Takahashi, Y. Yamada, M. Konishi, T. Watanabe, A. Ibi, T. Muroga, S. Miyata, Y. Shiohara, T. Kato, and T. Hirayama, "Magnetic field dependence of  $J_c$  for Gd-123 coated conductor on PLD-CeO<sub>2</sub> capped IBAD-GZO substrate tapes," *Superconductor Science and Technology*, vol. 18, no. 8, p. 1118, 2005.
- [21] Y. Yamada, K. Takahashi, H. Kobayashi, M. Konishi, T. Watanabe, A.

- Ibi, T. Muroga, S. Miyata, T. Kato, and T. Hirayama, "Epitaxial nanostructure and defects effective for pinning in Y(RE)Ba<sub>2</sub>Cu<sub>3</sub>O<sub>7-x</sub> coated conductors," *Applied Physics Letters*, vol. 87, no. 13, p. 132502, 2005.
- [22] J. Wang, J. Kwon, J. Yoon, H. Wang, T. Haugan, F. Baca, N. Pierce, and P. Barnes, "Flux pinning in YBa<sub>2</sub>Cu<sub>3</sub>O<sub>7-δ</sub> thin film samples linked to stacking fault density," *Applied Physics Letters*, vol. 92, no. 8, p. 082507, 2008.
- [23] J. Gazquez, M. Coll, N. Roma, F. Sandiumenge, T. Puig, and X. Obradors, "Structural defects in trifluoroacetate derived YBa<sub>2</sub>Cu<sub>3</sub>O<sub>7</sub> thin films," *Superconductor Science and Technology*, vol. 25, no. 6, p. 065009, 2012.
- [24] R. Guzman, J. Gazquez, V. Rouco, A. Palau, C. Magen, M. Varela, J. Arbiol, X. Obradors, and T. Puig, "Strain-driven broken twin boundary coherence in YBa<sub>2</sub>Cu<sub>3</sub>O<sub>7-δ</sub> nanocomposite thin films," *Applied Physics Letters*, vol. 102, no. 8, p. 081906, 2013.
- [25] S.-M. Choi, J.-W. Lee, G.-H. Shin, J.-H. Lee, G.-W. Hong, S.-H. Moon, and S.-I. Yoo, "Characteristics of high J<sub>c</sub> GdBCO coated conductors fabricated by the RCE-DR process," *IEEE Transactions on Applied Superconductivity*, vol. 23, no. 3, pp. 8001004-8001004, 2012.
- [26] S.-M. Choi, J.-W. Lee, J.-H. Lee, S.-H. Moon, and S.-I. Yoo, "The Effect of Growth Temperature on GdBa<sub>2</sub>Cu<sub>3</sub>O<sub>7-δ</sub> Coated Conductors Fabricated by the RCE-DR Process," *IEEE Transactions on Applied Superconductivity*, vol. 25, no. 3, pp. 1-5, 2014.
- [27] E. Talantsev, S. Wimbush, N. Strickland, J. Xia, P. D'Souza, J. Storey, J. Tallon, B. Ingham, R. Knibbe, and N. Long, "Oxygen deficiency, stacking faults and calcium substitution in MOD YBCO coated conductors," *IEEE Transactions on Applied Superconductivity*, vol. 23, no. 3, pp. 7200205-7200205, 2012.
- [28] E. Gyorgy, R. Van Dover, K. Jackson, L. Schneemeyer, and J.

- Waszczak, "Anisotropic critical currents in  $\text{Ba}_2\text{YCu}_3\text{O}_7$  analyzed using an extended Bean model," *Applied physics letters*, vol. 55, no. 3, pp. 283-285, 1989.
- [29] K. Zhang, B. Dabrowski, C. Segre, D. Hinks, I. K. Schuller, J. Jorgensen, and M. Slaski, "Solubility and superconductivity in  $\text{RE}(\text{Ba}_{2-x}\text{RE}_x)\text{Cu}_3\text{O}_{7+\delta}$  systems (RE= Nd, Sm, Eu, Gd, Dy)," *Journal of Physics C: Solid State Physics*, vol. 20, no. 34, p. L935, 1987.
- [30] M. Murakami, N. Sakai, T. Higuchi, and S. Yoo, "Melt-processed light rare earth element-Ba-Cu-O," *Superconductor Science and Technology*, vol. 9, no. 12, p. 1015, 1996.
- [31] W. Zhang, Y. Huang, X. Li, T. Kodenkandath, M. Rupich, U. Schoop, D. Verebelyi, C. Thieme, E. Siegal, and T. Holesinger, "Control of flux pinning in MOD YBCO coated conductor," *IEEE Transactions on Applied Superconductivity*, vol. 17, no. 2, pp. 3347-3350, 2007.
- [32] K. Develos-Bagarinao and H. Yamasaki, "Microstructural defects associated with enhanced magnetic flux pinning in YBCO/DyBCO/YBCO multilayered thin films," *Superconductor Science and Technology*, vol. 24, no. 6, p. 065017, 2011.
- [33] H. Zhang, N. Gauquelin, C. McMahon, D. Hawthorn, G. Botton, and J. Wei, "Synthesis of high-oxidation Y-Ba-Cu-O phases in superoxygenated thin films," *Physical Review Materials*, vol. 2, no. 3, p. 033803, 2018.
- [34] P. McIntyre and M. Cima, "Microstructural inhomogeneities in chemically derived  $\text{Ba}_2\text{YCu}_3\text{O}_{7-x}$  thin films: Implications for flux pinning," *Journal of materials research*, vol. 9, no. 11, pp. 2778-2788, 1994.
- [35] L. Fu, N. Browning, W. Ramadan, S. Ogale, D. Kundaliya, and T. Venkatesan, "Interface and defect structures in  $\text{YBa}_2\text{Cu}_3\text{O}_{7-\delta}$  and Nb:  $\text{SrTiO}_3$  heterojunction," *Journal of Physics D: Applied Physics*, vol. 40, no. 1, p. 187, 2006.

- [36] H. Zhang, N. Gauquelin, G. Botton, and J. Wei, "Attenuation of superconductivity in manganite/cuprate heterostructures by epitaxially-induced CuO intergrowths," *Applied Physics Letters*, vol. 103, no. 5, p. 052606, 2013.
- [37] Y. Jia, U. Welp, G. Crabtree, W. Kwok, A. Malozemoff, M. Rupich, S. Fleshler, and J. Clem, "Microstructure dependence of the c-axis critical current density in second-generation YBCO tapes," *Journal of Applied Physics*, vol. 110, no. 8, p. 083923, 2011.
- [38] E. Talantsev, N. Strickland, S. Wimbush, J. Storey, J. Tallon, and N. Long, "Hole doping dependence of critical current density in  $\text{YBa}_2\text{Cu}_3\text{O}_{7-\delta}$  conductors," *Applied Physics Letters*, vol. 104, no. 24, p. 242601, 2014.
- [39] D. E. Morris, A. G. Markelz, B. Fayn, and J. H. Nickel, "Conversion of 124 into 123+ CuO and 124, 123 and 247 phase regions in the Y-Ba-Cu-O system," *Physica C: Superconductivity*, vol. 168, no. 1-2, pp. 153-160, 1990.
- [40] Z. Chen, F. Kametani, S. Kim, D. Larbalestier, H. Jang, K. J. Choi, and C. Eom, "Influence of growth temperature on the vortex pinning properties of pulsed laser deposited  $\text{YBa}_2\text{Cu}_3\text{O}_{7-x}$  thin films," *Journal of Applied Physics*, vol. 103, no. 4, p. 043913, 2008.

Table 4.1.  $T_{c,zero}$ ,  $\Delta T_c$ , Average linear SF density, FWHM values of (003) reflections, and magnetic  $J_c$  values for samples

Sample	$T_{c,zero}$ (K)	$\Delta T_c$	Average linear SF density ( $10^6/\text{cm}$ )	FWHM of (003) reflection (degree)	Magnetic $J_c$ @ 77 K, 0 T (MA/cm <sup>2</sup> )
Pristine	94.2	0.6	0.37 ( $\pm 0.03$ )	0.247(2)	3.11
5 min	93.9	0.6	-	0.203(2)	2.27
15 min	93.8	0.9	0.19 ( $\pm 0.04$ )	0.180(2)	2.38
30 min	93.4	1.2	-	0.180(2)	2.02
60 min	93.1	1.2	-	0.178(1)	-

Table 4.2.  $T_{c,zero}$ ,  $\Delta T_c$ , Average linear SF density, and the FWHM values of (003) reflections for samples

Sample ID	Annealing conditions in 300 mTorr	$T_{c,zero}$ (K)	$\Delta T_c$ (K)	Average linear SF density ( $10^6/\text{cm}$ )	FWHM values of (003) reflection (degree)
Sample A	As-prepared (Pristine)	94.2	0.6	0.37 ( $\pm$ 0.03)	0.247(2)
Sample B	750 °C, 5 min	93.8	0.6	0.29 ( $\pm$ 0.08)	0.204(5)
Sample C	500 °C, 1 h	94.2	0.7	0.49 ( $\pm$ 0.07)	0.346(3)

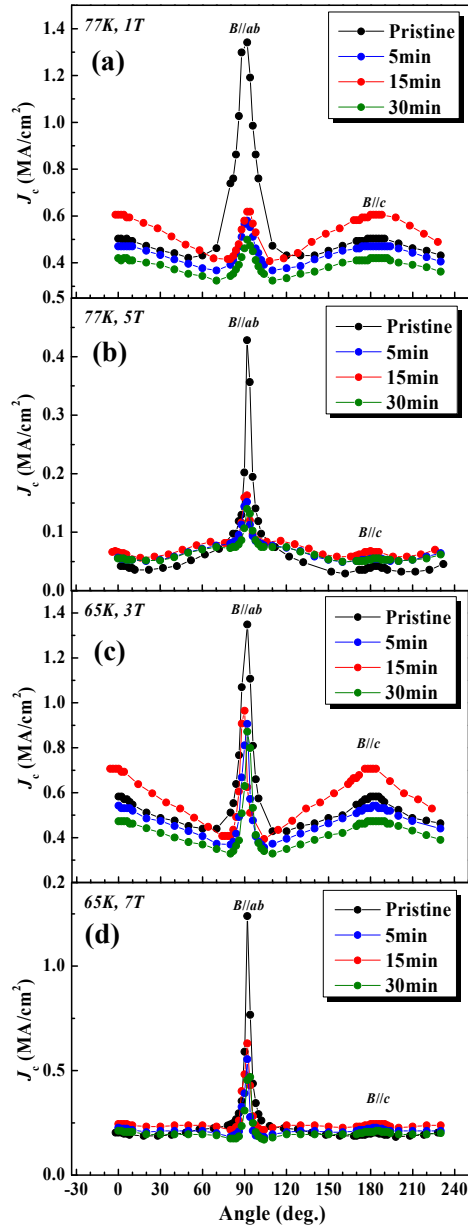


Fig 4.1. Angular dependence of  $J_c$  values ( $B$ ,  $\theta$ ,  $T$ ) (a) at 77 K in 1 T, (b) at 77 K in 3 T, (c) at 65 K in 3 T, and (d) at 65 K in 7 T for pristine and GdBCO CCs annealed at 750°C in the  $PO_2$  of 300 mTorr for 5, 15 and 30 min.

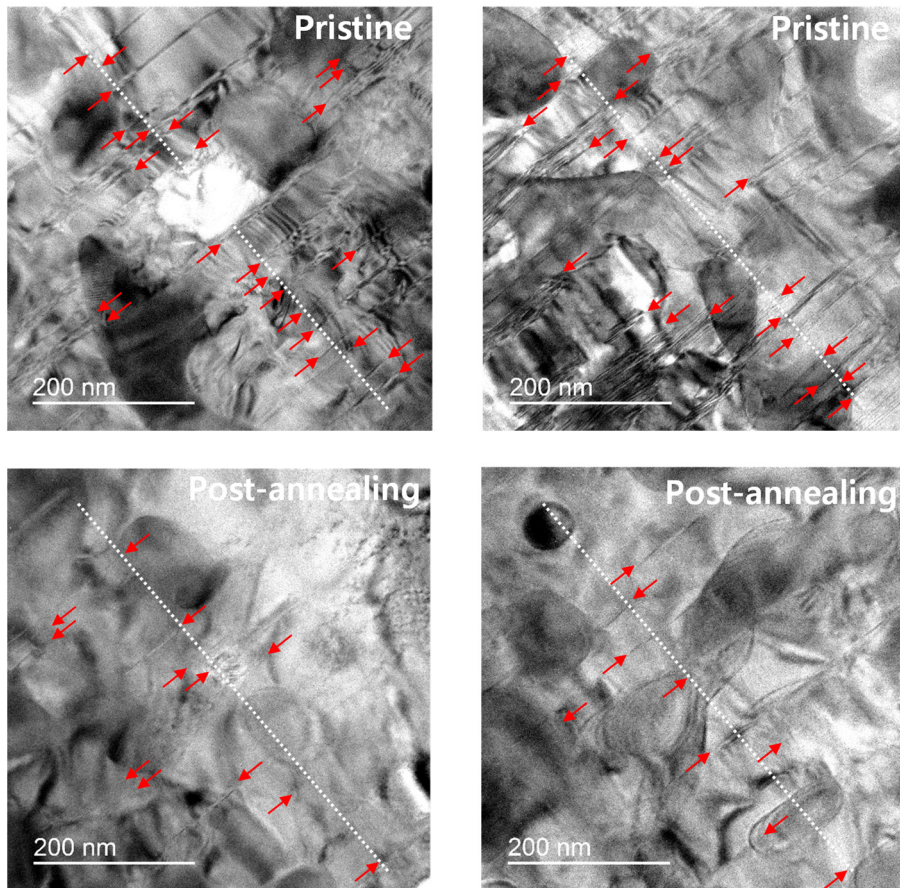


Fig. 4.2. Cross-sectional TEM images of pristine and post-annealed GdBCO CCs for 15 min. (Red arrows indicate the SFs)

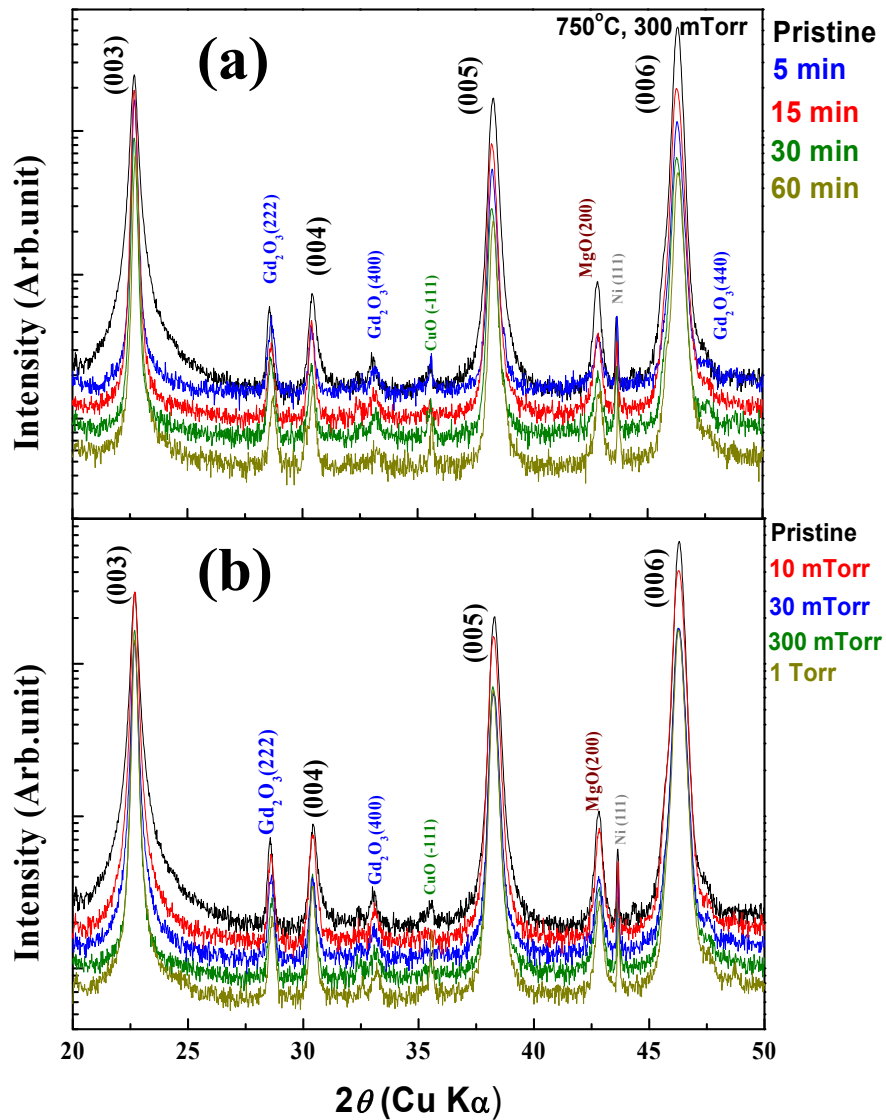


Fig. 4.3. XRD patterns of pristine and GdBCO CCs post-annealed (a) at 750°C in the  $PO_2$  of 300 mTorr for 5, 15, 30 and 60 min and (b) at 750°C in the  $PO_2$  of 10, 30, 300 and 1000 mTorr for 15 min.

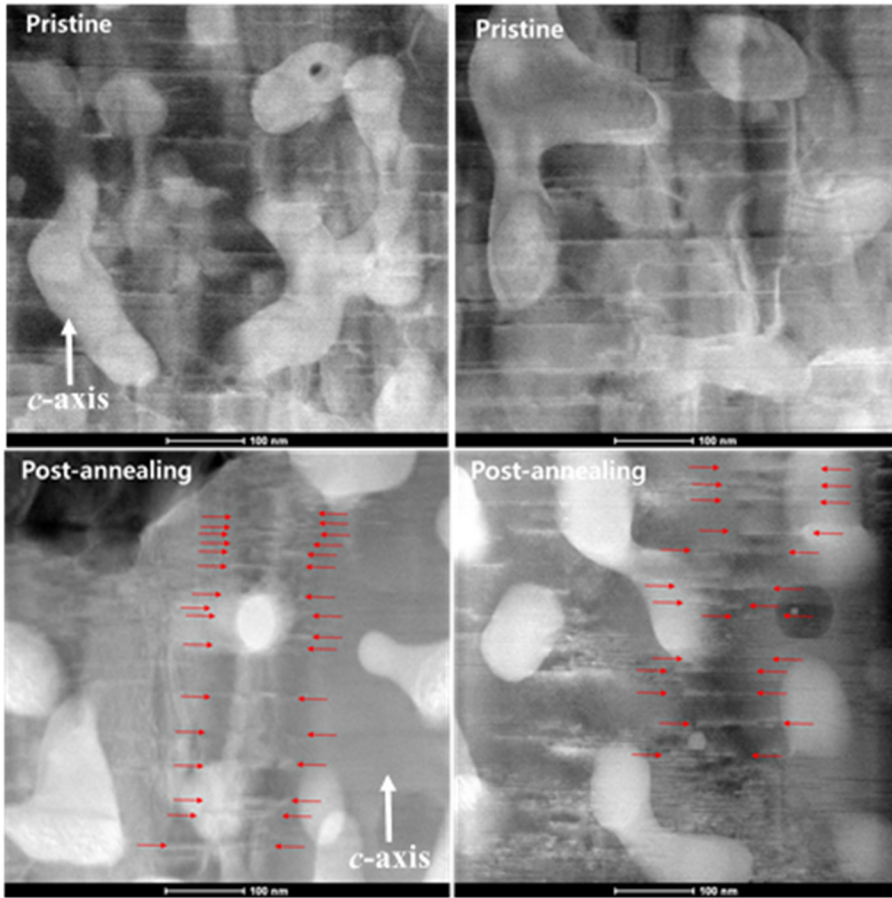


Fig. 4.4. STEM images of the pristine and post-annealed GdBCO CCs for 15 min. HAADF-STEM images show that the SFs were piled up along the *c*-axis of the GdBCO CCs (red arrows).

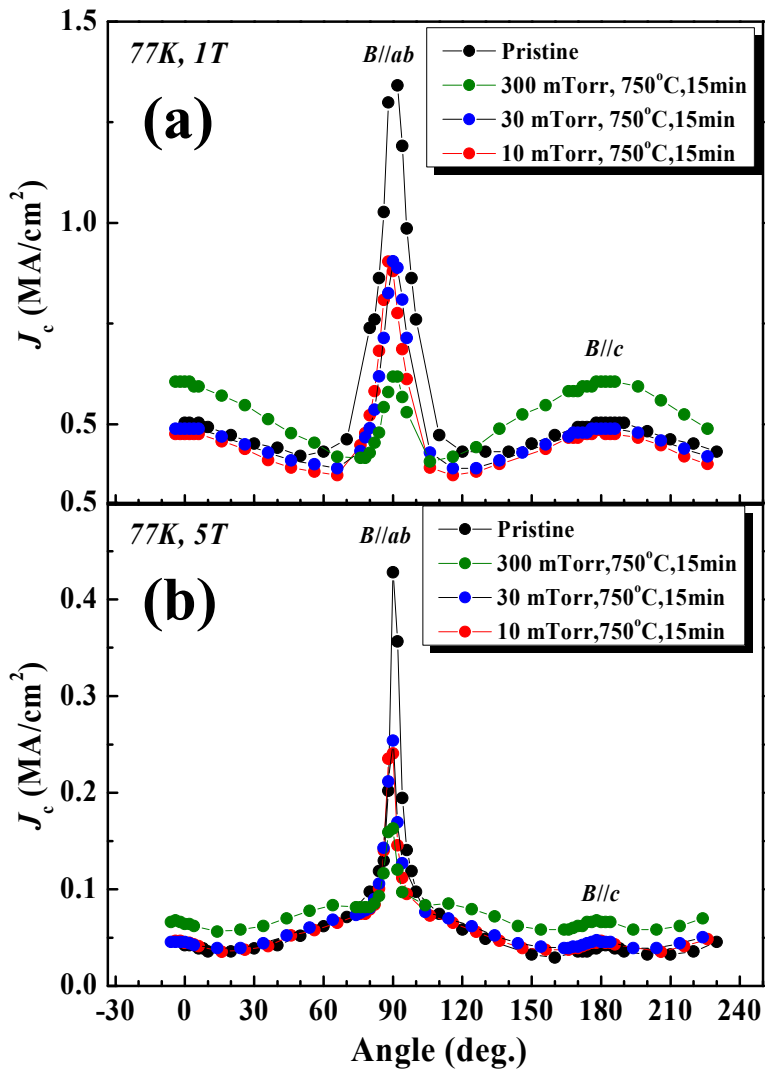


Fig. 4.5. Angular dependence of  $J_c$  value ( $B$ ,  $\theta$ ,  $T$ ) at 77 K in (a) 1 T, and (b) 5 T compared with 10, 30, and 300 mTorr.

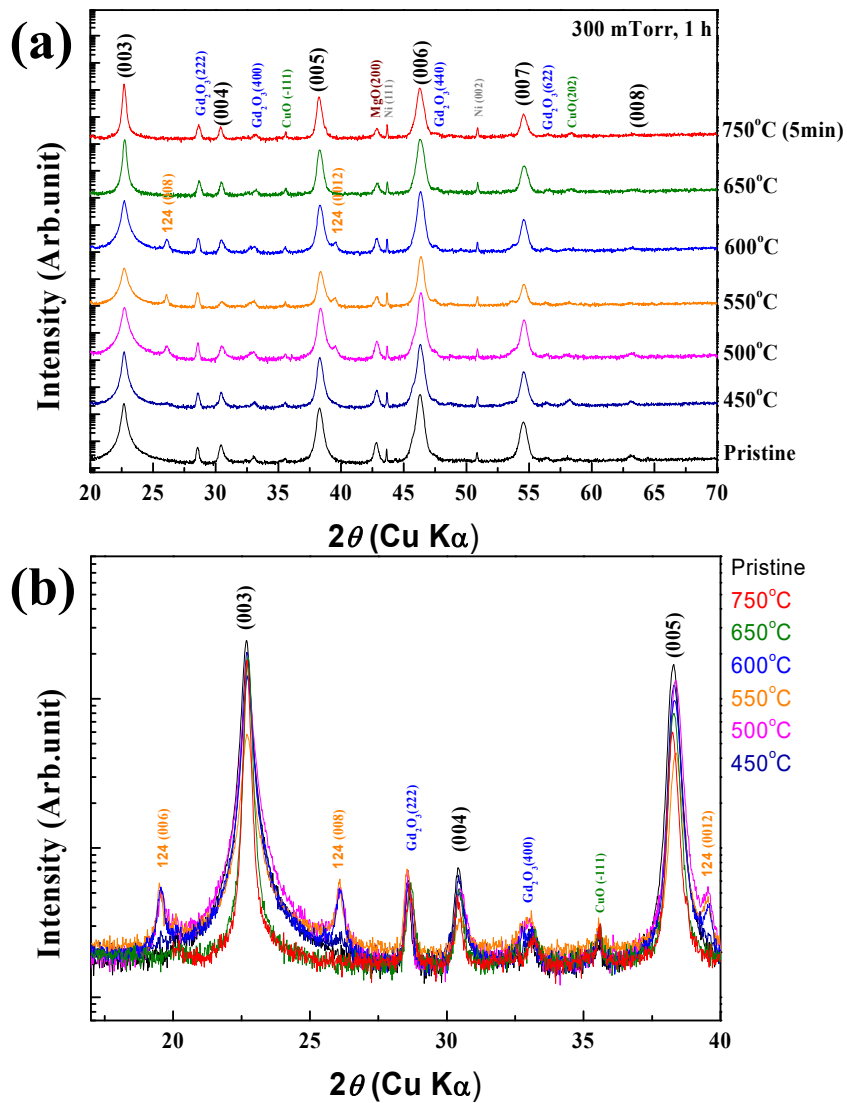


Fig. 4.6. Theta-2theta ( $\theta$ - $2\theta$ ) scans of samples. As-grown pristine GdBCO CCs samples were post-annealed at 450, 500, 550, 600, 650, and 750°C in the  $PO_2$  of 300 mTorr from 20° to 70° (a) and from 17° to 40° (b).

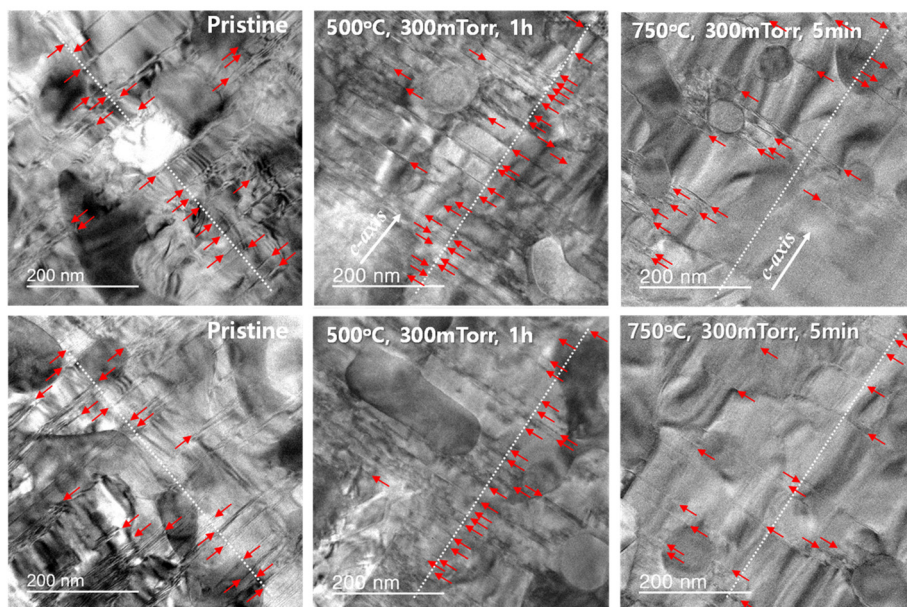


Fig. 4.7. Cross-sectional TEM micrographs of pristine sample and GdBCO CCs annealed at 500°C (1 h) and 750°C (5 min) in the  $PO_2$  of 300 mTorr. The SFs are indicated by red arrows.

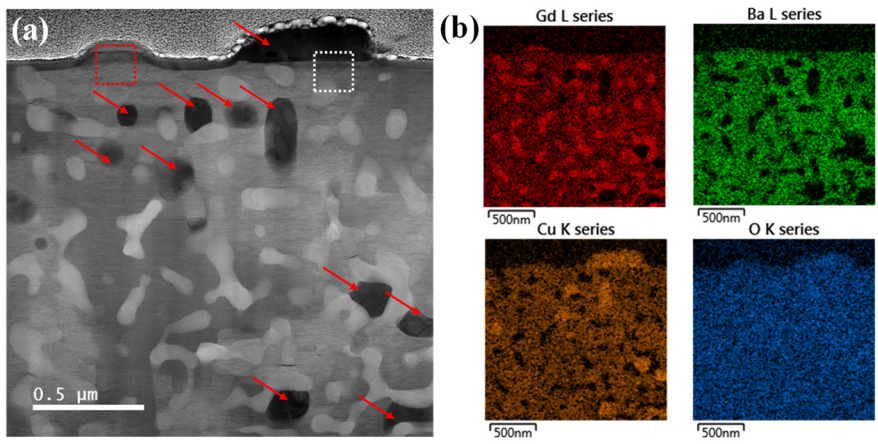


Fig. 4.8. Cross-sectional STEM micrographs of pristine sample and GdBCO CCs annealed at 500°C in the  $PO_2$  of 300 mTorr for 1 h (a) and EDS elemental mapping (b). The CuO phases are indicated by red arrows.

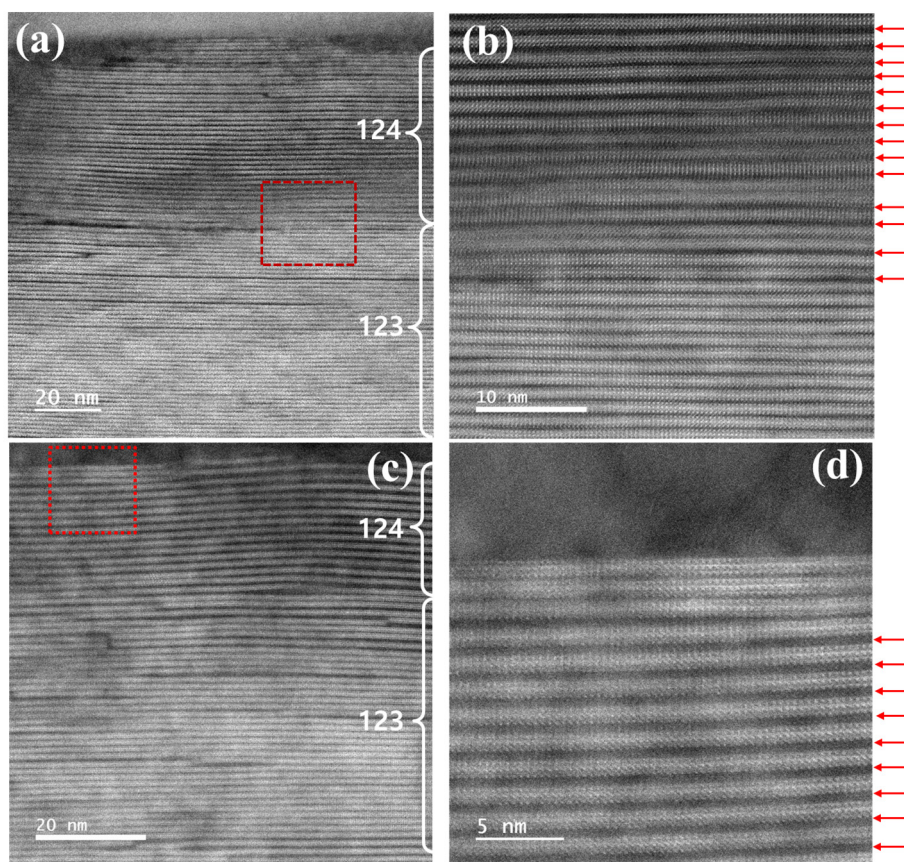


Fig. 4.9. Magnified HAADF images are indicated by red rectangular (a) and white rectangular (c) in Fig. 3 for GdBCO CCs annealed at 500°C in the  $PO_2$  of 300 mTorr for 1 h. High resolution HAADF images are noted by red rectangular (b) and (d).

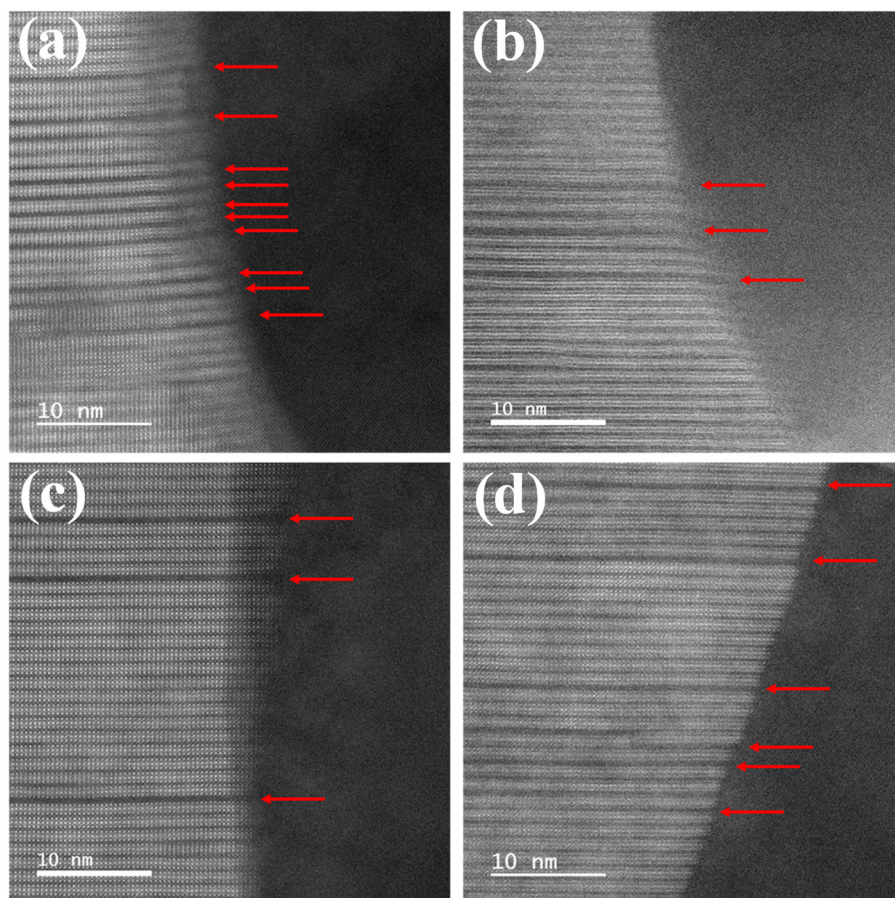


Fig. 4.10. High resolution HAADF images showing the distribution of SFs near the CuO phase in the GdBCO matrix for GdBCO CCs annealed at 500°C in the  $PO_2$  of 300 mTorr for 1 h. The red arrows indicate the double CuO planes.

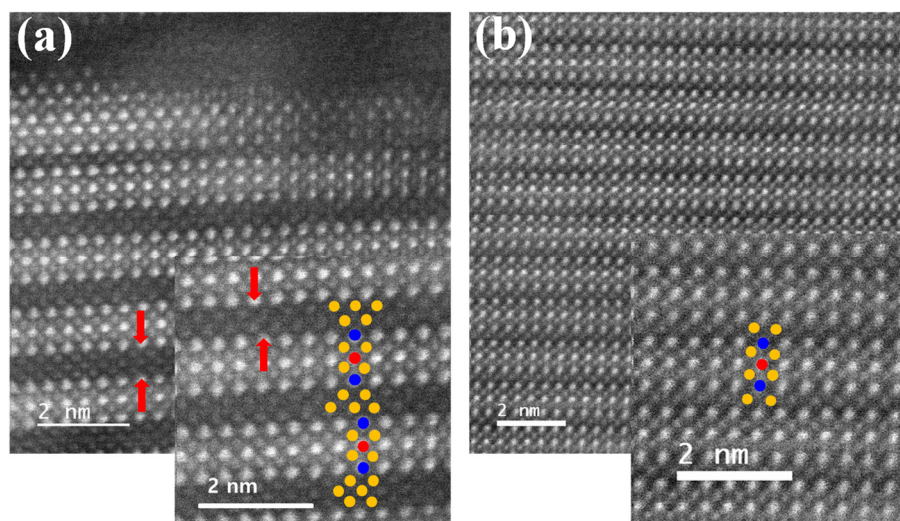


Fig. 4.11. Atomic scale resolution HAADF images showing the double CuO planes (a) and single CuO planes (b).

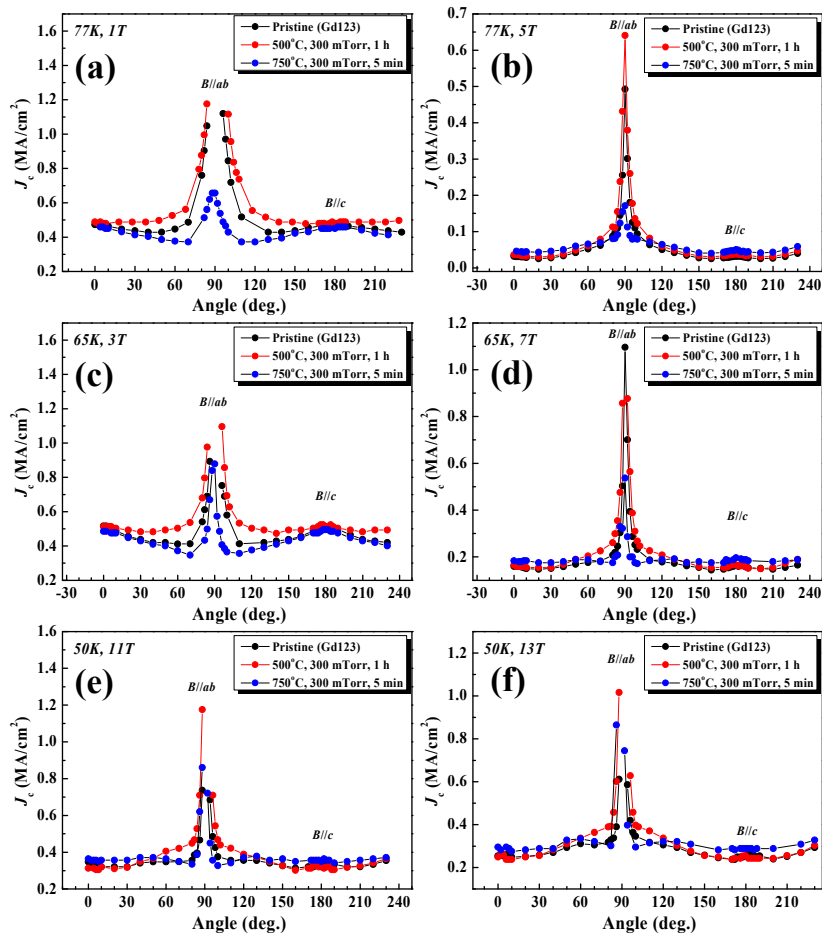


Fig. 4.12. The field angle dependency  $J_c$  of both the pristine sample and post-annealed GdBCO CCs (a) at 77 K in 1 T, (b) at 77 K in 5 T, (c) at 65 K in 3 T, (d) at 65 K in 7 T, (e) at 50 K in 11 T, and (f) at 50 K in 13 T.

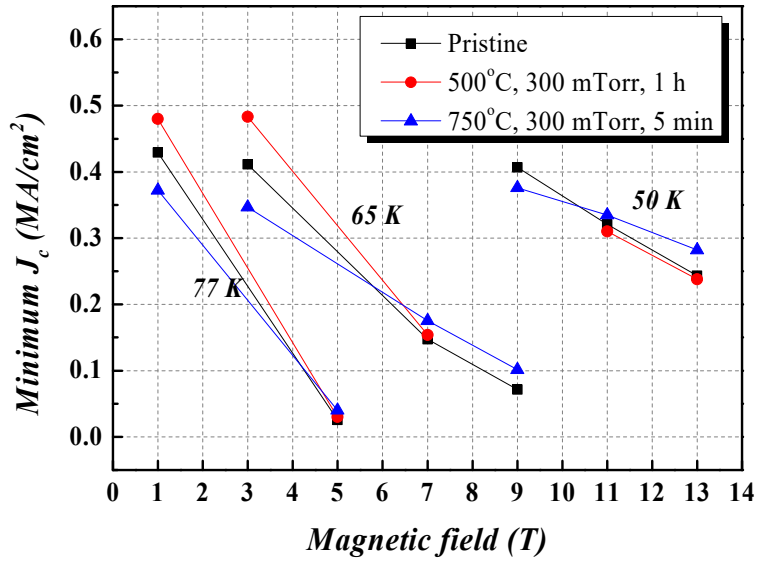


Fig. 4.13. The  $J_{c,min}$  values of pristine sample and post-annealed GdBCO CCs versus the applied fields at 77, 65, and 50 K.

## Chapter 5. Conclusion

In this thesis, we characterized the pinning properties and microstructures of REBCO films fabricated by the PLD and RCE-DR process. In order to investigate the effect of  $\text{RE}_2\text{O}_3$  nanoparticles on the pinning properties of REBCO films, the REBCO films with  $\text{RE}_2\text{O}_3$  nanoparticles were grown on the  $\text{CeO}_2$ -buffered MgO (100) single crystal substrate by PLD. With increasing the  $\text{RE}_2\text{O}_3$  doping contents, the in-plane texture and out-of-plane texture of the  $\text{RE}_2\text{O}_3$ -doped REBCO films were degraded due to the strain effect induced by the lattice mismatch between the superconducting matrix and dopants. The  $\text{RE}_2\text{O}_3$ -doped REBCO films showed the improved pinning properties below 40 K. However, the  $\text{RE}_2\text{O}_3$ -doped REBCO films exhibited the degradation of pinning properties above 65 K due to the severe degradation in the  $T_{c,zero}$  values. To identify the origin of the significant  $T_{c,zero}$  drop for the  $\text{RE}_2\text{O}_3$ -doped REBCO films, we employed the GPA and TEM-EDS analysis. From the results of the GPA analysis, we could observe that the compressive and tensile strain were extended near the  $\text{Eu}_2\text{O}_3$  nanoparticles, leading to the  $T_{c,zero}$  drop. Moreover, we observed that the Eu/Ba ratio was increased with increasing the  $\text{Eu}_2\text{O}_3$  doping contents by TEM-EDS analysis, indicating that the  $\text{Eu}_2\text{O}_3$  nanoparticles caused the substitution of Eu for Ba site, leading to the  $T_{c,zero}$  drop. Even though the  $\text{RE}_2\text{O}_3$  nanoparticles were effective for improving pinning properties at relatively low temperature, the  $\text{RE}_2\text{O}_3$ -doped REBCO films exhibited the degradation of pinning properties at high temperature due to a residual strain effect and the formation of solid solution.

Next, we identified the origin of  $J_c$  peak along the  $c$ -axis direction for the GdBCO films fabricated by PLD. We fabricated the GdBCO films having the  $J_c$  peak for  $B//c$  by modifying the position of a laser focal point. From the angular dependence of  $J_c$ , the GdBCO films fabricated by the narrow spot size showed the  $J_c$  peak for  $B//c$  at 77 K in 1 T. However, the  $J_c$  peak for  $B//c$  disappeared with increasing the magnetic fields at 77 K. However, at 65 K, the small  $J_c$  peaks for  $B//c$  were observable in all samples in 3 and 5 T. In order to investigate the origin for the  $J_c$  peak along the  $c$ -axis direction, we performed SEM and STEM analysis. The GdBCO films with  $J_c$  peak for  $B//c$  showed a lot of outgrowths on the top surface. The outgrowth was identified as the CuO and Gd123 phases by the STEM-EDS mapping analysis. Also, various defects such as threading dislocation, twin boundaries, and SFs were observable in all samples. The significant difference of microstructures was the density and length of SFs. The GdBCO films having the  $J_c$  peak for  $B//c$  exhibited the high density of the short SF. Since the edge dislocation at the boundary of short SFs can act as pinning centers, the GdBCO film with high density of short SFs shows  $J_c$  peak for  $B//c$  at 77 K in 1 T.

Finally, we investigated the effect of post-annealing process on the pinning properties of GdBCO CCs by RCE-DR. On the basis of the GdBCO phase diagram, we annealed the GdBCO CCs at various temperatures ranging from 450 to 750 °C in the low  $PO_2$  region (300 mTorr). With the annealing temperature of 750°C in the  $PO_2$  of 300 mTorr, the  $T_{c,zero}$  values of GdBCO CCs were degraded from 94.2 K to 93.1 K with increasing an annealing time. Also, the peak broadening of (003) reflection for the GdBCO CCs annealed at 750°C was smaller than that for the pristine sample, indicating the SF density was

reduced. From the cross-sectional TEM micrographs, we observed the reduced SF density for the GdBCO CCs annealed at 750°C in the  $PO_2$  of 300 mTorr for 15 min. Among the post-annealed samples, the GdBCO CCs annealed for 15 min show enhanced in-field  $J_c$  values for  $B//c$  due to the SFs piled up along the  $c$ -axis direction. Also, we extended the annealing temperature down to 450°C. Interestingly, the Gd124 phases were observable in the GdBCO matrix below 600°C. In the cross-sectional HAADF-STEM micrographs, the Gd124 phases existed predominantly near the top surface of GdBCO CCs due to the CuO phase segregated at the top surface of GdBCO CCs. Compared with pristine sample, the  $J_{c,min}$  values of GdBCO CCs annealed at 750°C in the  $PO_2$  of 300 mTorr for 5 min were improved with increasing the applied fields due to the reduction of SF density. On the other hands, the  $J_{c,min}$  values of GdBCO CCs annealed at 500°C in the  $PO_2$  of 300 mTorr for 1 h were slightly improved at high temperature in low magnetic fields. Consequently, the reduction of SF in the REBCO matrix is effective for improving the  $J_{c,min}$  values at relatively low temperature in high magnetic fields while the  $J_{c,min}$  values can be enhanced by both increment in the SF density and the formation of Gd124 phases in the REBCO matrix at relatively high temperature in low magnetic fields.

# Publications

## Papers (SCI journals)

1. Won-Jae Oh, Jae-Eun Kim, Insung Park, and Sang-Im Yoo, “Improved pinning properties of  $\text{EuBa}_2\text{Cu}_3\text{O}_{7-\delta}$  films with  $\text{Eu}_2\text{O}_3$  nanoparticles prepared by pulsed laser deposition”, to be submitted.
2. Won-Jae Oh, Insung Park, Kookchae Chung, and Sang-Im Yoo, “Origin of  $J_c$  peak along the c-axis direction for GdBCO films by the PLD process”, to be submitted.
3. Won-Jae Oh, Insung Park, Kookchae Chung, Jae-Hun Lee, Seung-Hyun Moon, and Sang-Im Yoo, “Effect of post-annealing on the pinning properties of  $\text{GdBa}_2\text{Cu}_3\text{O}_{7-\delta}$  coated conductors by the RCE-DR process”, submitted
4. Won-Jae Oh, Insung Park, Kookchae Chung, Jae-Hun Lee, Hunju Lee, Seung-Hyun Moon, and Sang-Im Yoo, “Enhanced Pinning Properties of Sm-Doped GdBCO CCs by the RCE-DR Process”, *IEEE Transactions on Applied Superconductivity*, 29 (2019) 8002404
5. Won-Jae Oh, Insung Park, Jae-Hun Lee, Hunju Lee, Seung-Hyun Moon, Kiran Shinde, Kookchae Chung, and Sang-Im Yoo, “The Post-Annealing Effect on the Pinning Properties of  $\text{GdBa}_2\text{Cu}_3\text{O}_{7-\delta}$  Coated Conductors via RCE-DR”, *IEEE Transactions on Applied Superconductivity*, 28 (2018) 6602305
6. Won-Jae Oh, Jae-Eun Kim, and Sang-Im Yoo, “Enhanced Pinning

Properties of  $\text{GdBa}_2\text{Cu}_3\text{O}_{7-\delta}$  Films With the  $\text{Gd}_2\text{O}_3$  Nanoparticles”, *IEEE Transactions on Applied Superconductivity*, 27 (2017) 8000605

### Contributed papers (SCI journals)

7. Insung Park, Doo-Ho Lee, Won-Jae Oh, Jae-Hun Lee, Seung-Hyun Moon, and Sang-Im Yoo, “Stability Phase Diagram of  $\text{YBa}_2\text{Cu}_3\text{O}_{7-\delta}$  for the Composition of Y:Ba:Cu = 1:1:2.5 in Low Oxygen Pressures”, *IEEE Transactions on Applied Superconductivity*, 29 (2019) 7200105
8. Insung Park, Won-Jae Oh, Jae-Hun Lee, Seung-Hyun Moon, and Sang-Im Yoo, “Stability Phase Diagram of  $\text{GdBa}_2\text{Cu}_3\text{O}_{7-\delta}$  for the Nominal Composition of Gd:Ba:Cu = 1:1:2.5 in Low Oxygen Pressures”, *IEEE Transactions on Applied Superconductivity*, 28 (2018) 7200105
9. Sungho Lee, Woo il Yang, Ho Sang Jung, Won-Jae Oh, Jiyeong Jang, Jae-Hun Lee, Kihyeok Kang, Seung-Hyun Moon, Sang-Im Yoo, and Sang Young Lee, “The Effects of Gd-Free Impurity Phase on the Aging Behavior for the Microwave Surface Resistance of Ag-coated  $\text{GdBa}_2\text{Cu}_3\text{O}_{7-\delta}$  at Cryogenic Temperatures”, *Electronic Materials Letters*, 14 (2018) 646-654
10. Kyung-Pil Ko, Soon-Mi Choi, Won-Jae Oh, Insung Park, and Sang-Im Yoo, “Epitaxial Growth of  $\text{CeO}_2$  Buffer Layers on IBAD-Textured MgO Templates by Pulsed Laser Deposition”, *IEEE Transactions on Applied Superconductivity*, 27 (2017) 6601105
11. Jung-Woo Lee, Soon-Mi Choi, Won-Jae Oh, Jae-Hun Lee, Seung-Hyun Moon, and Sang-Im Yoo, “Enhanced Pinning Properties of  $\text{GdBa}_2\text{Cu}_3\text{O}_{7-\delta}$

Coated Conductors via a Post-Annealing Process”, *IEEE Transactions on Applied Superconductivity*, 26 (2016) 8001906

### **Papers (Domestic journals)**

12. Won-Jae Oh, Insung Park, and Sang-Im Yoo, “The superconductivity and pinning properties of  $Y_2O_3$ -doped  $GdBa_2Cu_3O_{7-\delta}$  films prepared by pulsed laser deposition”, *Progress in Superconductivity and Cryogenics*, 20 (2018) 41-45

### **Contributed papers (Domestic journals)**

13. Insung Park, Won-Jae Oh, Jae-Hun Lee, Seung-Hyun Moon, and Sang-Im Yoo, “Refinement of  $Gd_2O_3$  inclusions in the  $GdBa_2Cu_3O_{7-\delta}$  films fabricated by the RCE-DR process”, *Progress in Superconductivity and Cryogenics*, 20 (2018) 46-49

## 초 록

반응성 동시증발 증착법 (reactive co-evaporation by deposition & reaction: RCE-DR) 은 높은 생산성과 77 K, self-field 에서 높은 임계 전류 밀도 ( $J_c$ ) 의 장점을 가진다. 그러나 RCE-DR 법으로 제조된  $GdBa_2Cu_3O_{7-\delta}$  (GdBCO) 선재 (CCs) 의 경우 펄스레이저 증착법 (pulsed laser deposition: PLD), 유기금속 증착법 (metal-organic deposition: MOD) 및 유기금속화학 증착법(metal-organic chemical vapor deposition: MOCVD) 과 같은 공정을 이용하는 타제조사의 선재 보다 자속 고정 특성 (flux pinning property) 이 약한 단점이 있다. RCE-DR 법으로 제조된  $REBa_2Cu_3O_{7-\delta}$  (REBCO, RE: light rare earth) 박막의 자속 고정 특성을 향상시키기 위하여 본 연구에서 2가지 다른 방법으로 접근하였다. 첫째, REBCO 막 내부에 포집되어 있는  $RE_2O_3$  의 입자 크기가 PLD 및 MOD 공정으로 제조된 자속 고정점 (artificial pinning centers: APCs) 의 크기로 줄여 들었을 때 자속 고정 특성이 어떻게 변화하는지를 확인하는 것이다. 다음으로, 낮은 산소 분압 하에서 RCE-DR 법으로 제조된 GdBCO 선재를 후열처리하여 적층결함 (stacking faults: SFs) 을 제어하는 것이다.

RCE-DR 법으로 제조된 GdBCO 막 내부 기지상에 포집되어 있는  $Gd_2O_3$  입자의 평균 크기는 flux line 을 효과적으로 고정하기에 너무 크기 때문에, 자장 하  $J_c$  값을 향상시키기 위해서는  $Gd_2O_3$  입자의 크기를 줄여야만 한다. 따라서 본 연구에서 PLD 법으로  $CeO_2$  버퍼층을 가지는 MgO 단결정 기판 위에  $RE_2O_3$  나노입자를 가지는 REBCO (RE= Eu and Gd) 막을 제조하였다. 그리고 제조된 시료의

자속 고정 특성을 분석하여,  $\text{RE}_2\text{O}_3$  입자의 크기를 줄이는 것이 얼마나 자속 고정 특성에 향상을 주는지 확인하고자 하였다. 또한 PLD 법으로 제조된 GdBCO 막에서  $c$  축 방향의 자기장이 가해졌을 때 생기는  $J_c$  피크 원인을 규명하고자 하였다. 다른 한편으로는 RCE-DR 법으로 제조된 GdBCO 선재를 낮은 산소 분압 하에서 다양한 온도의 조건에서 후열처리하여 자속 고정 특성을 향상시키고자 하였다. 후열처리 조건은 GdBCO 상안정도를 기반으로 신중하게 선택하였다. 주요 결과는 다음과 같다.

첫째,  $\text{RE}_2\text{O}_3$  를 첨가한 REBCO (RE=Eu, Gd) 초전도막의 자속 고정 특성을 최적화하는 실험을 진행하였다. 0, 2, 5, 7, 그리고 10 mol%  $\text{Gd}_2\text{O}_3$  입자가 첨가된 GdBCO 막과 0, 2, 4, 5, 6, 그리고 8 mol%  $\text{Eu}_2\text{O}_3$  입자가 첨가된 EuBCO 막을 PLD 법을 이용하여  $\text{CeO}_2$  버퍼층을 가지는 MgO 단결정 기판위에 성장시켰다. 모든 시료중에, 각각 5 mol%  $\text{Gd}_2\text{O}_3$ 가 첨가된 GdBCO 박막과 4 mol% 의  $\text{Eu}_2\text{O}_3$  가 첨가된 EuBCO 박막이 다른 시료와 비교하였을 때, 20 K 그리고 40 K 에서 가장 높은  $J_c$  ( $B//c$ ) 값과 자속고정힘 (pinning force density:  $F_p$ ) 을 보였다. 따라서 40 K 이하에서 각각 5 mol%  $\text{Gd}_2\text{O}_3$  와 4 mol% 의  $\text{Eu}_2\text{O}_3$  가 최적의 첨가량으로 규명하였다. 하지만 65 K 이상의 온도에서는  $\text{RE}_2\text{O}_3$  가 첨가된 시료가 첨가하지 않은 시료보다 저하된 피닝특성을 보였다. 투과전자현미경 (Transmission Electron Microscopy: TEM) 분석을 통해 기지상 내부에 임의로 분포되어 있는  $\text{RE}_2\text{O}_3$  나노 입자가 18 nm 의 평균 크기를 가지는 것을 확인 하였다. RCE-DR 법으로 제조된 GdBCO 선재와 달리, 이러한 특이한 특성을 보이는 이유는  $\text{RE}_2\text{O}_3$ 를 첨가에 따른 급격한 임계온도 (Transition temperature:  $T_{c,zero}$ ) 의 저하하였기 때문이다. 그리고 이러한 급격한

$T_{c,zero}$  의 저하는 첨가된  $RE_2O_3$  나노 입자 근처의 기지상에서 solid solution 의 형성과 strain effect 가 존재하기 때문이다.

둘째, PLD 법으로 제조된 GdBCO film 의  $c$  축 방향에서의  $J_c$  peak 의 원인을 규명하였다. PLD 공정 변수 중에서 focal point 의 위치를 조절하여 77 K 1 T 에서  $B//c$  방향의  $J_c$  peak 가 있는 시료 (시료 A) 와 없는 시료 (시료 B) 를 성공적으로 제조 하였다. 시료 A는 표면에 outgrowth 가 많이 관찰 되었으며, 시료 B는 비교적 깨끗한 표면을 보였다.  $J_c$  의 각도의존성 결과를 통해 77 K 1 T 에서 시료 A 는  $J_c$  peak ( $B//c$ ) 를 나타내는 반면  $J_c$  peak ( $B//ab$ ) 가 매우 작아지는 것을 관찰하였다. 하지만, 77 K 에서 자기장의 세기가 커질수록 시료 A 의  $J_c$  peak ( $B//c$ ) 가 사라지는 것을 확인하였다. 반면에, 시료 B의 경우 77 K 1 T 에서  $J_c$  peak ( $B//c$ ) 가 관찰되지 않았다. 주사투과전자현미경 (Scanning Transmission Electron Microscopy: STEM) 분석을 통해 모든 시료에서 threading dislocation 과 twin boundary (TB) 를 확인 하였다. 시료 A와 시료 B의 가장 큰 미세구조 차이점은 SFs 의 밀도와 길이였다. 시료 A의 경우, 시료 B 보다 기지상 내부에 SFs의 밀도가 높고 길이가 짧은 것을 관찰 하였다. 따라서 SFs의 경계에 존재하는 edge dislocation 이 효과적인 자속 고정점으로 작용하는 것으로 사료되며, 이러한 결함들이  $c$  축 방향의  $J_c$  peak 를 나타내는 주요 원인으로 규명하였다.

마지막으로, 후열처리 공정이 RCE-DR 법으로 제조된 GdBCO 선재의 피닝특성에 미치는 영향을 규명하였다. 750°C, 300 mTorr 에서 15 분 후열처리를 한 시료가 가장 향상된  $J_c$  ( $B//c$ ) 값을 보였으며, 이는 SFs 가  $c$  축 방향으로 정렬되어 있기 때문이다. 후열처리를 한 시료는 77 K 1 T 그리고 65 K 3 T 에서는 열처리를 하지 않은

시료보다 낮은 최소임계전류밀도 ( $J_{c,min}$ ) 값을 보였지만, 77 K 5 T 그리고 65 K 7 T 에서는 향상된  $J_{c,min}$  값을 보였다. 그리고  $J_c (B//ab)$  값은 SFs 와 굉장히 밀접한 관계가 있는 것을 확인하였다. TEM 미세구조 분석을 통해 후열처리를 한 시료의 경우, 기지상 내부 SFs 의 길이가 짧아지고 밀도가 낮아진 것을 확인 하였고, 이는  $J_{c,min}$  값을 향상시키고  $J_c (B//ab)$  값을 저하시킨 요인으로 사료된다. 또한 열처리 온도를 상대적인 저온의 영역으로 확대하였다. 앞서 고온에서 열처리를 하였을 때와 달리, 상대적인 저온인 450 ~ 600°C 에서 열처리를 하였을 때는 기지상 내부에  $GdBa_2Cu_4O_8$  (Gd124) 상이 생성되며 SFs 의 밀도가 높아지는 것을 확인 할 수 있었다. 500°C 에서 열처리한 시료에 대해 High-angle annular dark-field (HAADF)-STEM 분석을 하여 Gd124 상이 주로 표면과 기지상 내부의 CuO 상 주위에서 생성되는 것을 확인하였다. 50-77 K 의 온도영역에서, 750°C 에서 열처리를 한 시료는 SFs 의 밀도가 낮아졌기 때문에 상대적인 고자기장에서  $J_{c,min}$  이 향상되었고, 500°C 에서 열처리를 한 시료는 Gd124 가 생성되고 SFs 의 밀도가 높아졌기 때문에 저자기장에서  $J_{c,min}$  과  $J_c (B//ab)$  값이 향상되었다.

**주요어:**  $REBa_2Cu_3O_{7-\delta}$  (REBCO) films,  $Eu_2O_3$ 가 첨가된  $EuBa_2Cu_3O_{7-\delta}$  (EuBCO) 박막,  $Gd_2O_3$ 가 첨가된  $GdBa_2Cu_3O_{7-\delta}$  (GdBCO) 박막, 펄스레이저 증착법 (PLD), 반응성 동시증발 증착법 (RCE-DR), 후열처리 공정, 자속 고정점, 임계전류밀도 ( $J_c$ ), 자속 고정 힘 밀도 ( $F_p$ )

**학 번:** 2014-21430